UNIVERSITÀ DEGLI STUDI DI CATANIA

DIPARTIMENTO DI SCIENZE BIOLOGICHE, GEOLOGICHE E AMBIENTALI

DOTTORATO DI RICERCA IN SCIENZE GEOLOGICHE, BIOLOGICHE ED AMBIENTALI

XXXI CICLO

UNRAVELLING VOLCANIC TREMOR SOURCE AT MOUNT ETNA FROM QUANTITATIVE MULTIPARAMETRIC ANALYSIS AND MOMENT TENSOR INVERSION

Giancarlo Spedalieri

Coordinatore:
Prof.ssa Agata Di Stefano

Tutor:

Prof. Stefano Gresta

Co-Tutor:

Prof. Andrea Cannata
Dott. Giuseppe Di Grazia
Dott. Luciano Zuccarello

NOVEMBRE 2018

Giancarlo SPEDALIERI

STUDIO DELLA SORGENTE DEL TREMORE VULCANICO AL MT. ETNA MEDIANTE ANALISI QUANTITATIVA MULTIPARAMETRICA ED INVERSIONE DEL TENSORE MOMENTO.

Abstract: L'interpretazione dei segnali sismici osservati in contesti vulcanici e la descrizione quantitativa dei meccanismi alla sorgente costituiscono gli obiettivi principali della moderna sismologia vulcanica.

Dalla fine degli anni '70, alcuni autori hanno dedicato la loro attività a comprendere le dinamiche ed i meccanismi alla sorgente in grado di generare sismicità a lungo periodo (sismicità LP). La sismicità LP include segnali sismici come il tremore vulcanico e gli eventi a bassa frequenza (eventi LP), caratterizzati da simile contenuto spettrale (0.2 – 5.0 Hz), imputabili alla dinamica dei fluidi magmatici e idrotermali. Il tremore è il segnale sismico più distintivo registrato in contesti vulcanici attivi, può durare minuti, ore, persino mesi o anni ed è possibile osservarlo sia durante fasi quiescenti che duranti fasi eruttive.

L'obiettivo principale di questa tesi è stato lo studio della sorgente del tremore vulcanico al vulcano Etna (Italia). A tale scopo, è stato analizzato il tremore vulcanico registrato durante l'intensa attività eruttiva sommitale verificatasi tra il 2011 ed il 2012. Negli anni in questione, i prodotti emessi a seguito di 25 eventi di fontane di lava hanno determinato la formazione di un nuovo cratere, il Nuovo Cratere di Sud Est (NSEC), a partire da un pit crater formatosi alla fine del 2009. Questo cratere si è andato a sommare a quelli già esistenti, ovvero il Cratere di Nord Est (NEC), il cratere Voragine (VOR), il cratere Bocca Nuova (BN) ed il Cratere di Sud Est (SEC, cratere alla cui base si è impostato il pit-crater precedentemente citato).

Grazie ai dati messi a disposizione dall'Istituto Nazionale di Geofisica e Vulcanologia – Sezioni di Catania (Osservatorio Etneo) e Palermo, la tesi in oggetto si è focalizzata su due differenti aspetti: i) lo studio multiparametrico basato sul

confronto quantitativo tra il tremore vulcanico e dati geochimici come il flusso di CO_2 al suolo e di SO_2 ai crateri sommitali; ii) l'inversione del tensore momento del tremore vulcanico registrato durante una delle fontane di lava del 2011.

Il confronto multiparametrico tra dati sismici e geochimici è stato effettuato al fine di individuare e stimare quantitativamente eventuali variazioni di trend analoghe tra le serie temporali poste a confronto, sia sincrone che caratterizzate da ritardi durante gli anni tra il 2011 ed il 2012. A tale scopo, sono state implementate quattro diverse tecniche d'analisi cioè la Cross-Correlazione (CC), la Cross-Correlazione Randomizzata (RCC), la Wavelet Coherence e Cross Power Spectrum (WC e CWS) e la regressione lineare (R^2). I risultati ottenuti con l'analisi RCC hanno messo in evidenza come variazioni nell'andamento del flusso di CO_2 al suolo siano analoghi a quelli evidenziati circa 35 giorni dopo nella serie temporale del tremore. Inoltre, variazioni nell'andamento della serie temporale del tremore vulcanico tendono a precedere di qualche giorno analoghe variazioni nel flusso di SO_2 ai crateri sommitali. Compatibilmente alle velocità di risalita stimate per i magmi etnei e considerando i risultati di analoghi confronti quantitativi effettuati precedentemente per altre fasi eruttive allo stesso vulcano, i risultati ottenuti hanno permesso di ipotizzare dinamiche di pressurizzazione e depressurizzazione del sistema di alimentazione superficiale durante le diverse fasi eruttive osservate nel periodo considerato.

Il secondo studio illustrato in questa tesi, invece, rappresenta una novità assoluta per il vulcano Etna: infatti, per la prima volta è stata affrontata un'analisi di inversione del tensore momento applicata al tremore vulcanico al fine di individuarne i parametri alla sorgente. Nello specifico, questa analisi è stata applicata al segnale sismico acquisito durante l'episodio di fontana di lava del 5 Agosto 2011, uno degli episodi più vigorosi tra i 25 che hanno caratterizzato il periodo 2011-2012.

L'analisi di inversione del tensore momento applicata al tremore vulcanico è stata effettuata in quattro step differenti. In primo luogo, al fine di limitare effetti di distorsione dovuti alla topografia, ad eterogeneità e a strutture superficiali,

l'analisi di inversione è stata effettuata nella banda di frequenze 0.2 – 0.5 Hz, ovvero considerando soltanto il contenuto a basse frequenze del tremore vulcanico; dato che tale banda di frequenza è in parte coincidente con quella del microseism, è stato verificato che tale segnale di origine marina/oceanica fosse trascurabile durante l'episodio di fontana di lava in questione. Il secondo step, invece, è stato incentrato sulla necessità di considerare una sorgente puntiforme per l'analisi di inversione; a tale scopo, la localizzazione della sorgente è stata effettuata in due fasi: in primo luogo, (i) un volume delle probabili sorgenti del tremore è stato individuato mediante il metodo di localizzazione basato sul decadimento delle ampiezze, mentre (ii) la migliore soluzione puntuale all'interno di questo volume è stata effettuata mediante l'analisi della distribuzione spaziale dei misfit ottenuti con l'inversione del tensore momento. Con il terzo step, attraverso un'analisi di inversione "*unconstrained*" si è proceduto ad individuare il tipo di meccanismo sorgente per la fase parossistica dell'episodio di fontana di lava considerato. Infine, con l'ultimo step è stata eseguita un'analisi di inversione "*constrained*" al fine di confermare il meccanismo alla sorgente. L'analisi di inversione del tensore momento ha permesso di definire un meccanismo alla sorgente caratterizzato prevalentemente da una componente isotropica. I risultati ottenuti hanno permesso di evidenziare un meccanismo sorgente generato da un crack sub-orizzontale prossimo all'area del cratere sommitale, interpretabile come una valvola attraverso la quale il magma ricco in gas arriva in superficie durante l'episodio di fontana di lava.

I risultati ottenuti dal confronto tra serie temporali geofisiche e geochimiche e dall'analisi di inversione del tensore momento del tremore vulcanico non solo hanno permesso di ottenere informazioni sulle dinamiche che hanno caratterizzato il sistema di alimentazione superficiale del vulcano Etna durante l'attività del 2011-2012, ma hanno anche fornito importanti spunti di riflessione da approfondire con eventuali studi futuri.

TABLE OF CONTENTS

LIST OF FIGURES

LIST OF TABLES

SINTESI IN ITALIANO

STUDIO DELLA SORGENTE DEL TREMORE VULCANICO AL MT. ETNA MEDIANTE ANALISI QUANTITATIVA MULTIPARAMETRI-CA ED INVERSIONE DEL TENSORE MOMENTO.

CAPITOLO 1

Il primo capitolo di questa tesi espone gli argomenti relativi alle conoscenze di base necessarie al fine di condurre il duplice studio del tremore vulcanico presentato con questo elaborato. Nello specifico, si compone di tre parti: la prima parte introduce brevemente la sismicità vulcanica, la seconda parte, invece, descrive il vulcano Etna, mentre la terza parte è dedicata ad una descrizione dei metodi di base per lo studio del tremore vulcanico registrato al vulcano Etna.

L'introduzione alla sismicità vulcanica oggetto della prima parte descrive le diverse tipologie di segnali sismici che è possibile osservare nei pressi di un vulcano attivo; sulla base degli studi più recenti, è stata effettuata una descrizione dei segnali sismo-vulcanici, tra cui il tremore vulcanico.

La descrizione del vulcano Etna, oggetto della seconda parte è stata effettuata prendendo in esame i più recenti studi al fine di mostrarne le principali caratteristiche geologiche, strutturali e geodinamiche; particolare attenzione, inoltre, è stata dedicata sia alla descrizione delle caratteristiche e delle modalità di acquisizione dei dati relativi al tremore vulcanico, sia alla descrizione della recente attività, specie per quanto riguarda l'attività eruttiva osservata tra il 2011 ed il 2012.

Infine, la terza parte è stata dedicata alla descrizione delle metodologie d'analisi per la caratterizzazione del tremore vulcanico come ampiezza, contenuto spettrale e localizzazione della sorgente.

CAPITOLO 2

Il secondo capitolo di questa tesi è dedicato al primo dei due studi sul tremore vulcanico effettuati nell'ambito delle attività del Dottorato di Ricerca, ovvero lo studio multiparametrico dell'attività al vulcano Etna tra il 2011 ed il 2012. A tale scopo, dopo una breve descrizione della letteratura concernente diversi casi

studio analoghi sia al vulcano Etna che in altri contesti vulcanici, ci si è focalizzati sui diversi step in cui è stato articolato il confronto tra la serie temporale del tremore vulcanico ed altre serie temporali acquisite durante lo stesso intervallo temporale. In primo luogo, sono state descritte le quattro tecniche d'analisi differenti scelte per il confronto quantitativo, ovvero la Cross-Correlazione (CC), la Cross-Correlazione Randomizzata (RCC), la Wavelet Coherence e Cross Power Spectrum (WC e CWS) e la regressione lineare (R^2). Successivamente, è stata effettuata una selezione dei dati geofisici (sismici e geodetici) e geochimici (flussi di gas vulcanici e rapporti tra flussi di gas emessi ai diversi crateri sommitali) messi a disposizione dall'Istituto Nazionale di Geofisica e Vulcanologia per il confronto quantitativo delle serie temporali. Successivamente, a causa di periodi in cui l'acquisizione dei dati di alcuni parametri non è stata possibile durante il periodo considerato, le analisi effettuate con i dati a disposizione hanno restituito dei risultati significativi soltanto nel caso dei confronti tra la serie temporale del tremore vulcanico e le serie geochimiche del flusso di gas vulcanici come CO_2 al suolo e flusso di SO_2 al plume. Nello specifico, mediante analisi RCC è stato possibile evidenziare come, rispetto alla serie temporale del tremore, analoghe variazioni di trend siano riscontrabili circa 35 giorni prima nel flusso di CO_2 al suolo e circa 50 giorni dopo nel flusso di SO_2 ai crateri sommitali. Ciò ha permesso di ipotizzare sia dinamiche caratterizzate da pressurizzazione durante le fasi non eruttive e depressurizzazione durante le fasi eruttive del sistema di alimentazione dell'Etna tra la seconda metà del 2010 e la prima metà del 2012, sia di stimare le modalità ed i tempi di risalita dei fluidi vulcanici durante il periodo in questione.

CAPITOLO 3

Il terzo capitolo di questa tesi espone il secondo dei due studi effettuati, ovvero l'Inversione del Tensore Momento (MTI) del tremore vulcanico registrato all'Etna durante la fontana di lava del 5 agosto 2011. Lo studio in questione costituisce una

novità assoluta per il vulcano Etna: infatti, si tratta del primo caso in cui un'analisi di inversione delle forme d'onda complete viene applicata al fine di individuare il meccanismo sorgente (tensore momento) del tremore registrato al vulcano in questione; allo stato attuale, l'analisi MTI applicata al tremore vulcanico registrato al vulcano Arenal (Costa Rica) rappresenta l'unico precedente descritto in letteratura.

La prima parte di questo capitolo descrive brevemente la letteratura concernente lo stato dell'arte in materia di caratterizzazione delle dinamiche e dei meccanismi alla sorgente in grado di generare la sismicità a lungo periodo (LP). Oltre ad illustrare i diversi modelli proposti da diversi autori per spiegare l'origine della sismicità LP alla sorgente, in questa prima parte è stata affrontata anche la trattazione matematica della procedura di inversione adottata con questo studio, nonché la descrizione sia dei limiti di questa metodologia sia della libreria delle "*Green's functions*" per la rappresentazione matematica della propagazione delle onde sismiche nella porzione superficiale dell'edificio vulcanico etneo.

La seconda parte di questo capitolo, invece, è incentrata sulla descrizione dell'analisi MTI effettuata, con particolare attenzione al principale limite di questa metodologia, cioè la limitata definizione del modello di velocità delle onde sismiche nel mezzo; avendo focalizzato l'analisi MTI sulla componente a bassa frequenza del tremore vulcanico (0.2 – 0.5 Hz), particolare attenzione è stata dedicata sia alla localizzazione della sorgente del tremore mediante il metodo di decadimento delle ampiezze, sia alla possibile influenza dovuta al microseism. Alla fine di questa parte, inoltre, sono stati presentati i risultati ottenuti. L'analisi MTI effettuata ha permesso di ottenere un crack sub-orizzontale con una prevalente componente isotropa come meccanismo sorgente del tremore vulcanico considerato, interpretabile come una valvola attraverso cui il magma ricco di gas viene emesso nell'atmosfera durante l'attività di fontana di lava.

CAPITOLO 4

Il capitolo 4, ultimo capitolo di questa tesi, oltre a riassumere i principali risultati ottenuti mediante il duplice studio effettuato, espone una serie di considerazioni e suggerimenti per eventuali lavori futuri concernenti studi analoghi.

ACKNOWLEDGEMENTS

The PhD training course at University of Catania gave me a great opportunity and I am very grateful to many people who have contributed to my research activity during the last three years.

First of all, I am deeply grateful to my supervisor Professor Stefano Gresta. I'm honored to have had the opportunity to be introduced into the field of volcano seismology from him. His supervision and his advice in the PhD training course were fundamental.

I would like to thank my tutors, Professor Andrea Cannata, Dr. Giuseppe Di Grazia and Dr. Luciano Zuccarello, their contributions were essential in the development of my PhD studies. They supported me with great scientific enthusiasm and their wide scientific knowledge. I especially thank Professor Andrea Cannata, with his professionalism, his attitude in research and his infinite patience supported me constantly during all phases of doctoral research and writing of this thesis.

I am very grateful to Catania and Palermo Sections of INGV that gave me the chance to work on volcanic monitoring data. I am indebted to all technicians and researchers who have worked on the seismic and geochemical data used for the studies of this thesis.

I am grateful to Drs. Francesca Bianco of the INGV of Naples and Gilberto Saccorotti of the INGV of Florence for the reviews. Their comments were important to improve the originality of this thesis and gave me the opportunity for further investigations and discussion.

I thank the colleague Salvo Moschella for helped me with the significant wave height data used with this thesis.

I would like to thank my PhD coordinator Prof. Agata Di Stefano, for the constant support to the training and all the aspects associated at PhD training program.

An invaluable thanks goes to my family, in particular to my parents who gave me motivation and support to overcome all the difficulties in these last years.

Finally, an invaluable thanks also goes to Maricla for her love, her support, her patience, for helping me to improve every day from every point of view, to believe in me and in my abilities.

ABSTRACT

UNRAVELLING VOLCANIC TREMOR SOURCE AT MOUNT ETNA FROM QUANTITATIVE MULTIPARAMETRIC ANALYSIS AND MOMENT TENSOR INVERSION

Developments of multiparametric monitoring networks, real time analysis techniques and the acquisition of high-resolution data, have allowed to improve the knowledge of the structures and dynamics that characterize the active volcanoes. To understand the dynamics of an active volcano, it is possible to proceed with two different types of studies: i) multiparametric studies based on the joint analysis of different data (such as geophysical, geochemical, petrological data); ii) detailed studies concerning specific data. In order to understand source volcanic tremor at Mt. Etna volcano, volcanic tremor recorded during the vigorous summit of 2011-2012 was analyzed. In particular, this thesis shows the results obtained from the investigation of the volcanic tremor source through a duplex study: i) a multiparametric study based on the quantitative comparison between different time series such as volcanic tremor amplitudes and geochemical data such as soil CO_2 flux and the SO_2 flux at summit craters; ii) a moment tensor inversion analysis of volcanic tremor recorded during a lava fountain episode of the considered period. For these studies, data acquired from the multiparametric monitoring network managed by *Istituto Nazionale di Geofisica e Vulcanologia* were used.The quantitative comparison between seismic and geochemical data was performed in order to identify and quantitatively estimate similar trends variations between the compared time series, both synchronous and characterized by time lags. To this end, four different analysis techniques have been implemented, such as Cross-Correlation, Randomized Cross-Correlation, wavelet analysis and linear regression. The obtained results allowed to infer pressurization and depressurization dynamics of the plumbing system during the different eruptive phases observed during the considered period. The moment tensor inversion analysis of the volcanic tremor recorded at Mt. Etna represents a novelty. Specifically, this analysis was applied to volcanic tremor recorded during the lava fountain episode that occurred on 5 August 2011, one of the most vigorous of the 25 episodes that characterized the 2011-2012 period. The results allowed to highlight a source mechanism generated by a sub-horizontal crack near the summit crater area, which can be interpreted as a valve through which gas-rich magma is ejected during the lava fountain activities.

Keywords: seismology, Mt. Etna volcano, volcanic tremor, lava fountains, multiparametric, moment tensor inversion.

INTRODUCTION

Volcanology is a multidisciplinary science that deals with the study of volcanoes based on the principles of different aspects of Earth Sciences, such as geology, geophysics and geochemistry. For this reason, the monitoring and surveillance of active volcanoes require the study of various types of geological, geochemical, and geophysical data. Each type of data (such as measurements of seismic signals, gas fluxes, ground deformation, temperature, gravity, etc) provides information about physical processes which may be related to movement of molten rock or other eruption precursory phenomena (McNutt et al., 2000).

In the last two decades, improvements in computerized acquisition, real time analysis systems, and more precise and higher quality data, have allowed to improve the knowledge about the structures and dynamics that characterize active volcanoes.

Generally, starting from the acquired monitoring data at a volcano, to understand the active dynamics it is possible to proceed through two different types of studies: i) multidisciplinary study based on the joint analysis of different data (such as geophysical, geochemical, petrological data), or ii) detailed studies concerning a specific type of acquired data.

Mount Etna volcano (Italy) is one of the most active and monitored volcanoes in the world, characterized by the continuous acquisition of different geophysical and geochemical data. The rapid evolution of the eruptive dynamics that characterizes this volcano and the multiparametric monitoring network, managed by the “Istituto Nazionale di Geofisica e Vulcanologia (INGV)”, allow us to consider Mt. Etna as a natural laboratory.

In the following chapters of this thesis the results, obtained with by the study of the activity that occurred at Mt. Etna during the 2011-12 period, will be presented. These years were characterized by an intense activity showing 25 paroxysmal episodes at the New South-East Crater (NSEC), each one reaching lava fountains at the climax of the activity.

The initial phases of the study concerned the investigation of seismic signals recorded during the considered period, focusing the attention on the features of volcanic tremor (frequency content, amplitude, source location). The following

work, on the other hand, was articulated in two different types of analyses: i) quantitative comparison of geophysical and geochemical time series recorded during 2011-2012 period, in order to highlight any relationship between different parameters and improve the knowledge on volcano dynamics; ii) moment tensor inversion of volcanic tremor recorded during the 5 August 2011 lava fountaining in order to localize the source of the seismic signals and describe its mechanism and geometry.

The idea of the first study arises from the conclusions obtained by Cannata et al. (2015) which examined the Mount Etna activity during 2013. With a comparative multiparametric study, relating temporal series of parameters such as volcanic tremor, infrasonic signals at summit craters, soil CO_2 flux and ground deformation, the authors highlighted pressurization and depressurization phases of the shallow plumbing system during the alternation between quiescence and eruptive phases, respectively. Considering the similarities of the volcano activity between 2011-2012 and 2013 (Behncke et al., 2014; De Beni et al., 2015), for the first period, a quantitative comparison between the RMS amplitude of the volcanic tremor and geochemical time series, as soil CO_2 flux and flow of SO_2 from the summit craters was performed.

The second study described in this thesis concerns the moment tensor inversion analysis of the volcanic tremor recorded at Mount Etna during the lava fountaining of 5 August 2011. At Mount Etna, inversion analyses of waveforms of seismic signals were made; for example, De Barros et al. (2009, 2011) performed a moment tensor inversion analysis of long period events recorded between 18 June 2008 and 3 July 2008. Through this analysis, the authors have obtained information regarding source geometry (De Barros et al., 2009) and mechanisms, (De Barros et al., 2011). As for the volcanic tremor recorded to other volcanoes, moment tensor inversion was carried out only in one case: at Arenal volcano (Costa Rica) by Davi et al. (2012). At Mt. Etna volcano, this type of study has never been performed before and the one presented in this study is the first attempt to do so.

In Chapter 1 of this thesis, the fundamentals regarding volcano seismicity, geological features and recent activity of Mount Etna, as well as the principal analyses routinely performed on Etna volcanic tremor, have been briefly described. In Chapter 2 and Chapter 3, instead, the main steps of the quantitative multiparametric comparison and the moment tensor inversion studies, were described. Specifically, each of the two chapters was divided into sections concerning general introduction, methods of analysis, description of the results, discussion and conclusions.

Finally, Chapter 4 summarizes the main results obtained with the studies carried out in this thesis, providing some perspectives for possible future studies.

CHAPTER 1 - BACKGROUND AND STATE OF ART

1.1 VOLCANO SEISMICITY

At active volcanoes, it is common to observe seismicity characterized by different signals with well-defined features. Volcanic seismology studies these signals; in particular, the main objective of this discipline is to understand the nature and dynamics of seismic sources associated with the injection and transport of magma and related to hydrothermal fluids (Chouet, 2003).

An aspect of volcano seismology concerns the classification of volcano-seismic signals. Already since the 70s, several authors with pioneering works have proposed classifications (e.g. Shimozuru, 1972; Minakami, 1974); the current classification refers to more recent works such as those of McNutt (2000, 2005) and Chouet (1996) and Wassermann (2012). According the latter, volcano seismicity can be distinguished into transient and continuous signals, even if some of these continuous signals simply reflect the superposition of discrete signals. On the basis of this subdivision, the main features of the volcano-seismic signals will be discussed below.

1.1.1 Transient volcano-seismic signals

- *Volcanic-Tectonic events (deep and shallow).*

Also called High-Frequency event (HF), *deep (below about 2 km) Volcanic-Tectonic events (VT-A)* manifest themselves by the clear onsets of P- and S-wave arrivals and their high frequency content (between 5 and 15 Hz; **Fig. 1.1**).

Volcanic-Tectonic events have been attributed to regional tectonic forces, gravitational loading, pore pressure effects and hydrofracturing, thermal and volumetric forces associated with magma intrusion, withdrawal, cooling, or some combinations of any or all of these (McNutt, 2005). They differ from their tectonic counterparts only in the patterns of occurrence, which at volcanoes are typically in swarms rather than mainshock-aftershock sequences (McNutt, 1996).

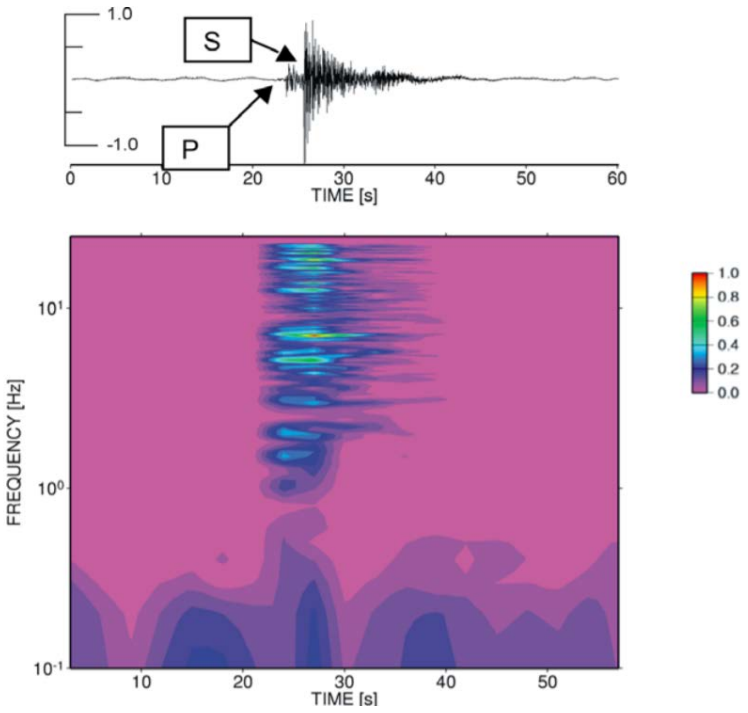

Figure 1.0.1. VT-A type event recorded at Mt. Merapi, Indonesia. The impulsive P- and S-wave arrivals are clearly visible in this signal, as well as their high-frequency content and short signal duration. The given color coding, representing normalized amplitude spectral density, is valid for all following figures. Also, the amplitudes of the corresponding amplitude-time representation are in arbitrary units and when given are normalized to the amplitude shown in this figure (from Wassermann, 2012).

Implementation of a suite of techniques used to improve locations represents one of the main progress in studying VT-A events. These techniques allowed defining many faults that were not discernable in standard locations (e.g. Prejean et al., 2002; McNutt, 2005). Moreover, high-resolution tomography, developed to image subsurface volcanic structures at scales of a few hundred meters (e.g. Dawson et al., 1999; Patanè et al., 2006,) was another recent method mostly based on VT-A events. This type of events is also very useful at volcanoes to determine stress orientations via study of focal mechanisms and stress tensor inversion.

Shallow (above about 1-2 km) Volcanic-Tectonic events (VT-B), instead, show much more emergent P-wave onsets and sometimes it is even impossible to detect any clear S-wave arrival (**Fig. 1.2**). The spectral bands are shifted to lower frequencies (1-5 Hz). Both observations are thought to be caused by a shallow hypocenter

location and therefore a larger amount of scattering during wave propagation, especially affecting higher frequencies. **Fig. 1.3** shows schematically models for VT-A and VT-B events.

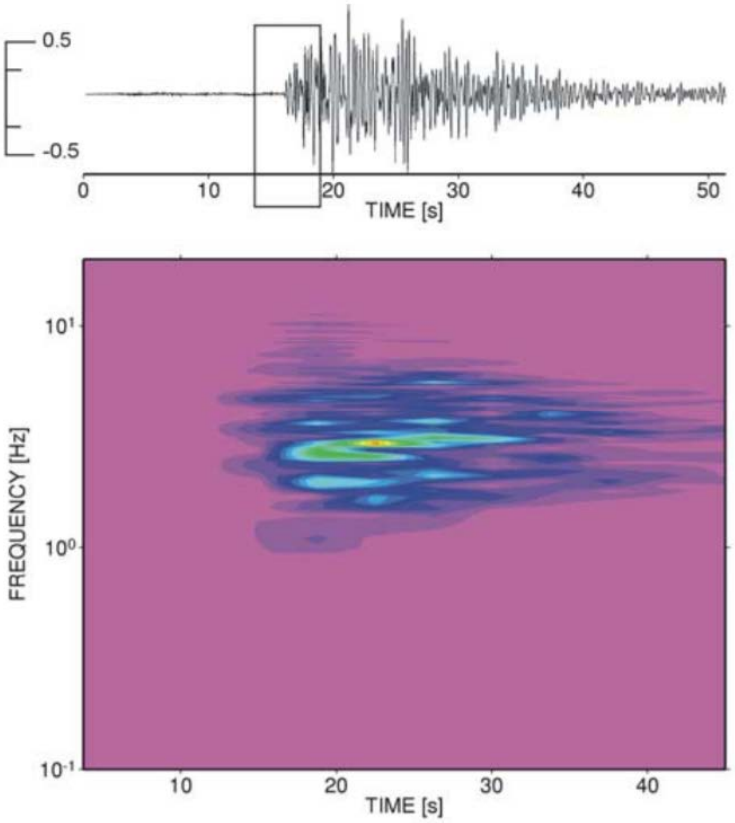

Figure 1.2. Typical example of a VT-B type event recorded during a high activity phase at Mt. Merapi. Note that the overall frequency content is mainly between 1 – 10 Hz with a dominant frequency at roughly 3 Hz (from Wassermann, 2012).

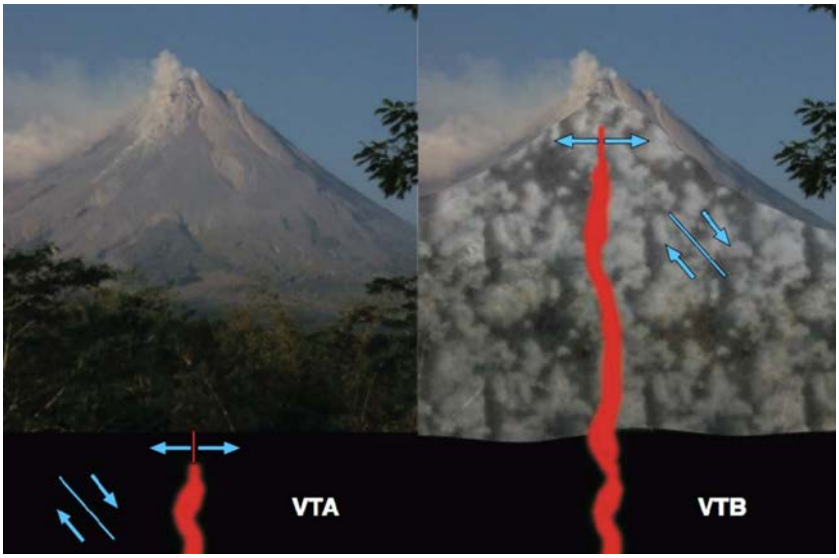

Figure 1.3. Two different models describing the occurrence of VT –A/B in active volcanoes. While some VT events are simply caused by reactivation of existing faults by the increasing stress due to magma ascent, the other possible mechanism is directly linked to the emplacement of the magma in the feeder system and the associated tensile faulting. In this picture, the difference between VT-A and VT-B is simply their location with respect to a high scattering region (from Wassermann, 2012).

- *Low Frequency (LF) events.*

Also called Long Period (LP) events (**Fig. 1.4**), they are generally characterized by emergent P-waves, lack of S-waves and dominant frequencies of 0.5-5 Hz (Chouet, 1996). They may be caused by internal volcanic activities associated with fluid movement, heat and gas supply from magma, and interaction between magma and underground water. Despite the ambiguity regarding the source, many authors have studied these events, focusing on particular features such as spectral content, rates, or relation to eruptions (McNutt, 2005).

Moreover, the use of broadband stations during the last decade also allowed the observation of very long period (VLP) events (with spectral content of 2-100 seconds; Neuberg et al., 1994; Ohminato et al., 1998) at many volcanoes around the world, such as Aso (Legrand et al., 2000), Merapi (Hidayat et al., 2002), Stromboli (Neuberg et al., 1994; Chouet et al., 2003), Popocatépetl (Chouet et al., 2005), Kilauea (Ohminato et al., 1998), Etna (Cannata et al., 2009).

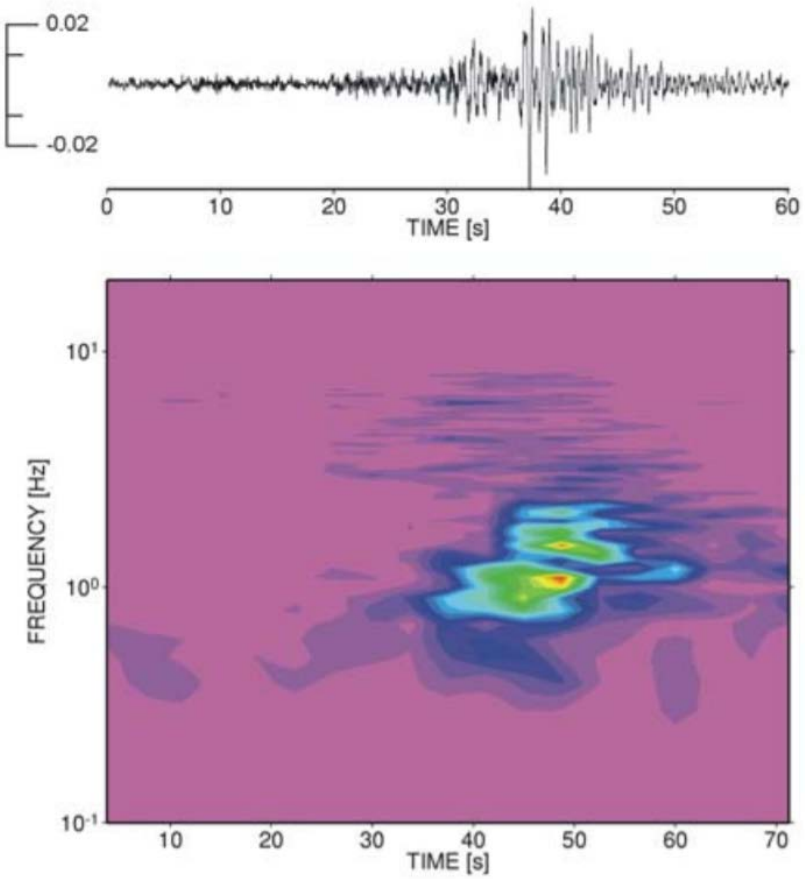

Figure 1.4. Example of a LF-wave group recorded at Mt. Merapi. Clearly the dominant frequency is around 1 Hz (from Wassermann, 2012).

They are assumed to be linked to the mass movements and to represent inertial forces resulting from perturbations in the flow of magma and gases through conduits (Uhira and Takeo, 1994; Kaneshima et al., 1996; Chouet, 1996). Some authors use the term Ultra Long Period event (ULP) to refer events with period longer than 100 s (e.g. Ohminato et al., 1998).

Among low frequency events we also find the tornillos, long-period volcano-seismic events (Chouet. 1996) whose shape bears a resemblance to the profile of a screw (**Fig. 1.5**).

The tornillo signals are characterized by (1) a long duration compared to the amplitude, (2) a long quasi-linear, slowly decaying coda and (3) a low frequency and monochromatic or quasi-monochromatic waveform sometimes showing a weak high-frequency onset superimposed on the low frequency (Torres et al., 1996). At Galeras volcano (Colombia), Narváez et al. (1997) have detected that five

out of six eruptions, that occurred between July 1992 and June 1993, were preceded by episodes of tornillo signals.

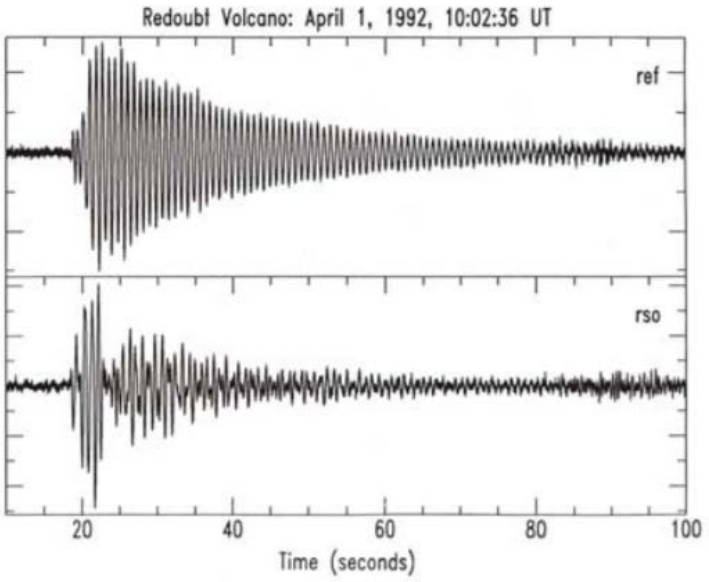

Figure 1.5. Example of a LF event recorded at two different sites located at Redoubt volcano, Alaska. The spindle shaped signal is also known as Tornillo. (from Wassermann, 2012).

- *Hybrid events, Multi-Phases events*

The volcano-seismic signals that share signal and frequency characteristics of both LF and VT-(A, B) events are usually labeled as *Hybrid events* (**Fig. 1.6**).

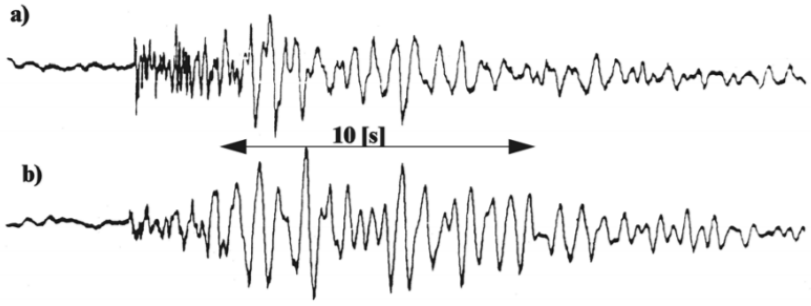

Figure 1.6. **a**) shows a Hybrid event and **b**) a VT-B event for comparison. The higher frequencies at the beginning of the Hybrid event are an obvious feature, while the later part shows the similarity with the VT-B event (from Wassermann, 2012).

This type of signals may reflect a possible mixture of source mechanisms from both event types and/or additionally reflect possible path effects (Harrington and Brodsky, 2007). For example, a VT microearthquake may trigger a nearby LP event. Lahr et al. (1994) and Miller et al. (1998) detected swarms of Hybrid events during the high activity phase of Redoubt (Alaska) and Soufriere Hills volcano (Montserrat, West Indies), respectively. Miller et al. (1998) concluded that such events reflect very shallow activity associated with a growing dome.

Multi-Phase events (MP also Many-Phases event; Shimozuru, 1972) are somewhat higher in their frequency content (3 to 8 Hz) than Hybrid events but are related to energetic dome growth at a very shallow level (**Fig. 1.7**). The name reflects their complicated waveforms which seems to consist of multiple phases following to each other.

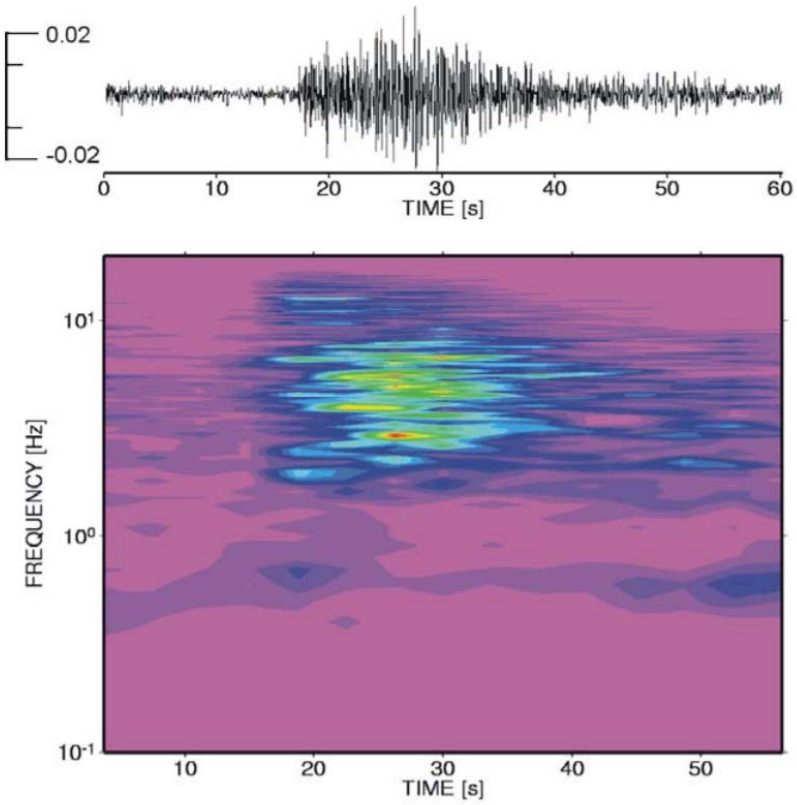

Figure 1.7. MP-event recorded at Mt. Merapi during strong dome formation. The frequency content is restricted between 3 - 10 Hz and resembles that of a VT-B type event at this volcano. (from Wassermann, 2012).

- *Explosion-quakes*

The *explosion-quakes* (**Fig. 1.8**) accompany explosive eruption and many ot them are characterized by air-shock phase in the seismograms. They have been extensively studied in recent years also by using infrasonic microphones or infrasonic pressure sensors: in fact, the infrasonic signal, defined as acoustic waves at frequency lower than the audible component of the sound (<20 Hz), for short distances travels in an almost homogenous atmosphere with no structures which can scatter, attenuate or reflect acoustic waves.

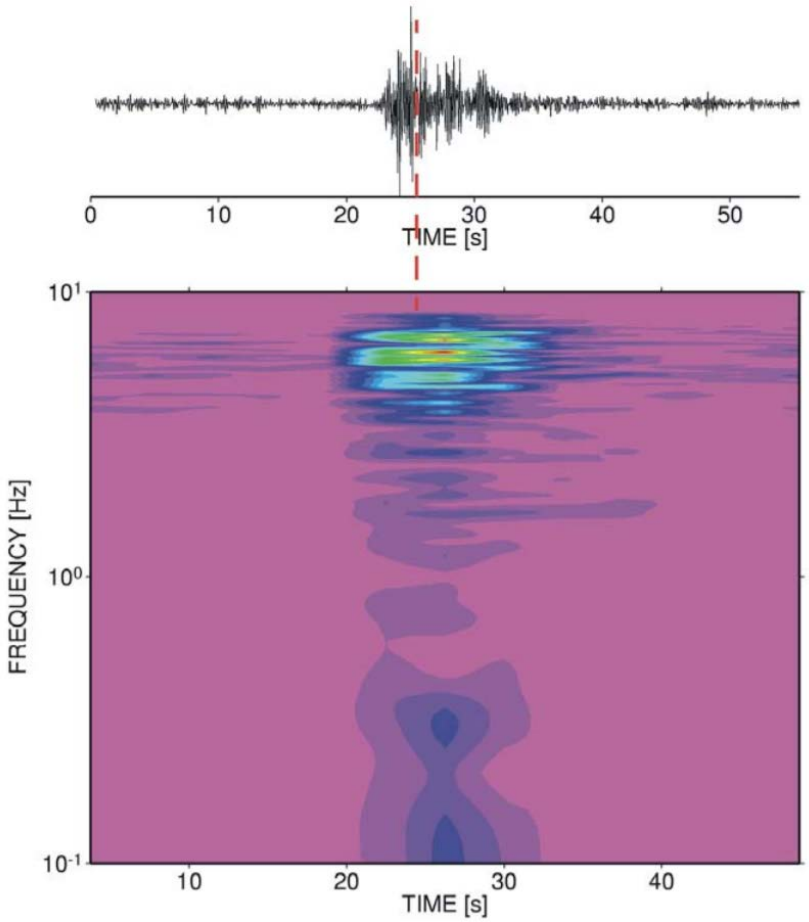

Figure 1.8. An explosion signal recorded at Stromboli volcano, Italy. The seismic station was located just 400 m from the active vent. The dashed line gives a rough estimate of the onset of a sonic wave also visible as high (red) amplitudes in the time-frequency plot around 5 Hz (from Wessermann, 2012).

Then, unlike the seismic signal whose wavefield is strongly affected by topography (Neuberg and Pointer, 2000) and path effects (Gordeev, 1993), the infrasonic signal maintains almost unchanged its features during the propagation, allowing to obtain information concerning source dynamics. Methods for determining the relative acoustic and seismic contributions during explosive eruptions were developed and showed time variations probably related to changing conduit features and conditions (Johnson and Aster, 2005; Andronico et al., 2013).

1.1.2. Continuous volcanic-seismic signals

- *Volcanic tremor.*

It remains the most distinctive seismic signal recorded at volcanoes and shares the same frequency band with the LP events (0.2 – 5.0 Hz). The main difference between LP events and volcanic tremor consists in the duration: similar to that of earthquakes for the LP events; minutes to longer than months for volcanic tremor. On the base of it, many authors have concluded that tremor is a series of low-frequency events occurring at intervals of few seconds (Chouet, 1992). In fact, the models developed to explain the tremor source, generally involving complex interactions of magmatic fluids with the surrounding rocks (e.g. Kubotera, 1974; Steinberg and Steinberg, 1975; Aki et al., 1977; Chouet, 1981), are similar to the models of LP events. Harmonic tremor and spasmodic tremor are two special cases of more general volcanic tremor. The former is a low-frequency, often monotonic sinusoid with smoothly varying amplitude, while the latter is a higher-frequency, pulsating, irregular signal (McNutt, 1996).

1.2 MOUNT ETNA VOLCANO

Situated in Eastern Sicily (Italy), Mount Etna (**Fig. 1.9**) is a polygenetic basaltic volcano among the most active volcanoes in the world, as well as the tallest in Europe with its elevation of 3350 a.s.l. (Branca et al., 2004).

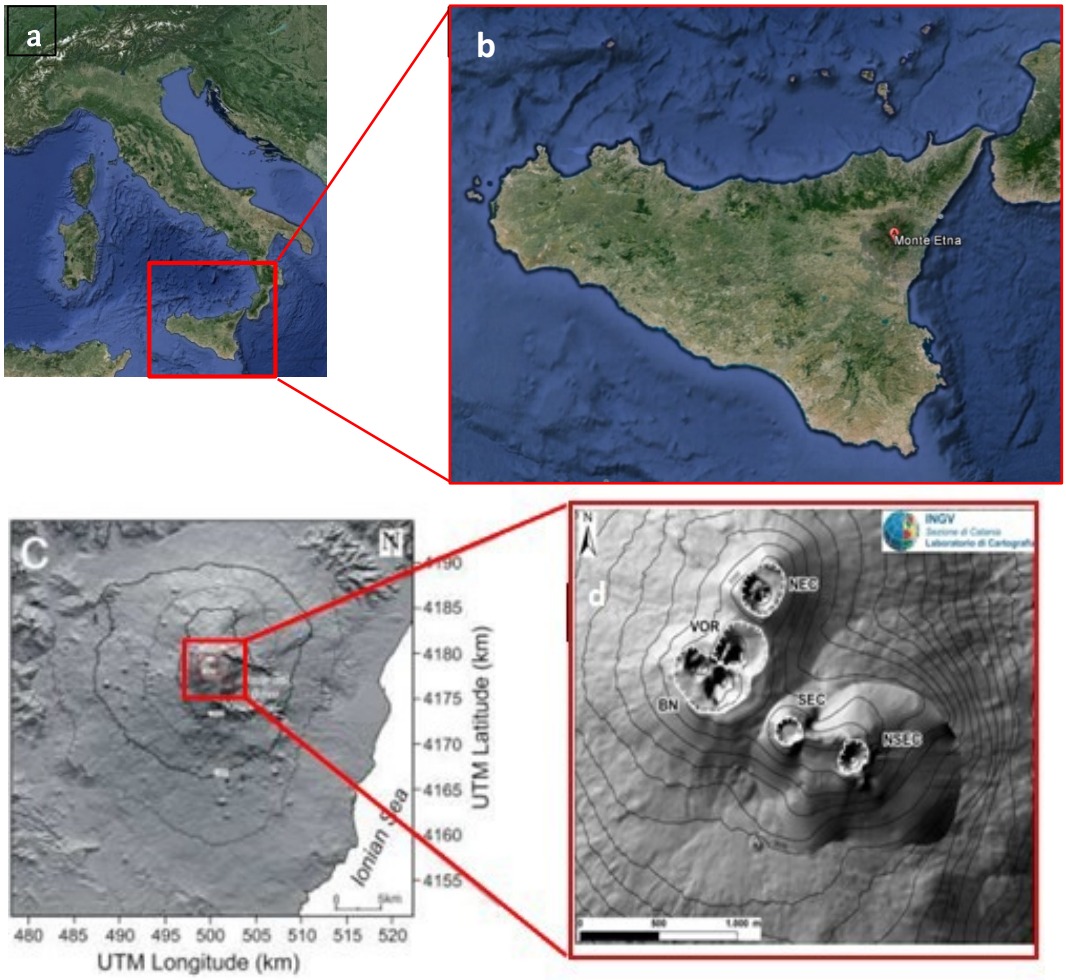

Figure 1.9. (**a, b**) Geographical position of Mt. Etna volcano. (**c**) Digital Elevation Model (DEM) of Mt. Etna volcano. (**d**) DEM with summit area in detail.

It is characterized by roughly elliptical base (38 × 47 km), occupies a total area of 1250 km^2 and the summit area of the volcano is currently characterized by five main active craters: Voragine (VOR), Bocca Nuova (BN), North- East Crater (NEC) and New South-East Crater (NSEC). Moreover, about 350 craters and minor vents are located in the flanks of volcano, each of which erupted only once.

1.2.1 Geological framework

The first studies on Mt. Etna were performed in the nineteenth century and successively published by Gemmellaro (1858), Lyell (1859) and Waltershausen (1880). In particular, they compiled the first geological maps of Mt. Etna and performed the first stratigraphic studies that allowed them to recognize the polygenetic origin of the volcano. Waltershausen (1880) published the first geological map of the entire volcano (Branca et al., 2004).

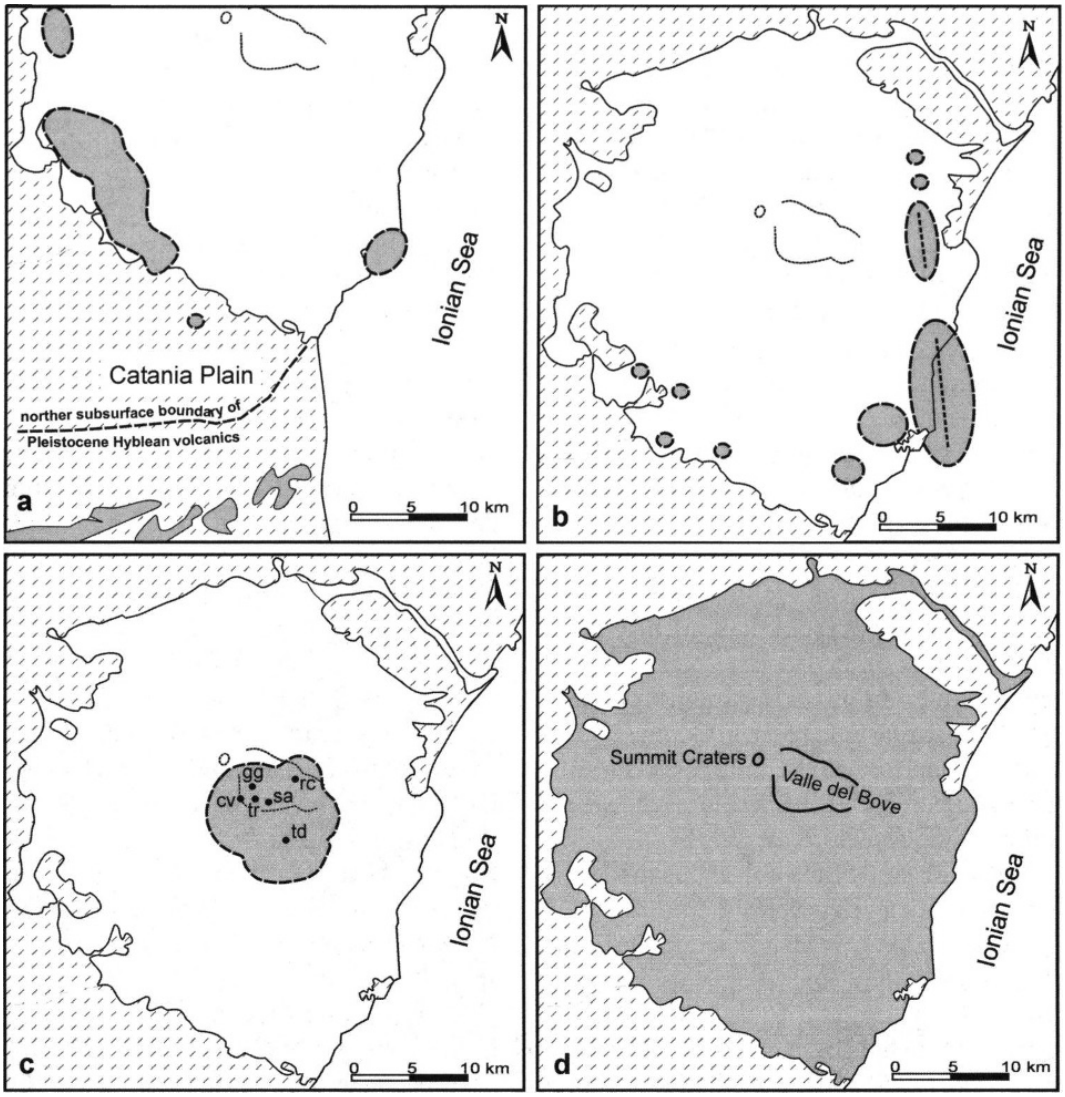

Figure 1.10. Schematic representation of Etna volcano evolutionary phases: **a**) Basal Tholeiitic phase; **b**) Timpe phase; **c**) Valle del Bove Centers phase, circle indicate the location of the volcanoes: td=Tarderia, rc=Rocche, tr=Trifoglietto, gg=Giannicola; sa=Salifizio, cv=Cuvigghiuni; **d**) Stratovolcano phase (from Branca et al., 2004).

The geological history of Mount Etna is quite recent and began about 500,000 years ago, in the middle of Pleistocene (Branca et al., 2008). The geological evolution of volcano is subdivided in four main phases (**Fig. 1.10**): (1) the Basal Tholeiitic phase, (2) the Timpe phase, (3) the Valle del Bove centers phase and (4) the stratovolcano phase (Branca et al., 2011a, 2004, 2008).

The earliest volcanic products erupted in Mt. Etna area were grouped in the (1) Basal Tholeiitic phase (**Fig. 1.10a**). The first subaerial products were erupted about 330 ka ago (Branca et al., 2011b) along the coast of the Ionian Sea immediately to the north of Catania, leading to the Aci Castello formation characterized by pillow lava and hyaloclastic breccia (Corsaro and Cristofolini, 2000, **Fig. 1.10a**). Overall, the products of the Basal Tholeiitic phase are tholeiitic basalts (Branca et al., 2008).

The (2) Timpe phase (**Fig. 1.10b**) occurred between about 220 ka and 129 ka ago (De Beni et al., 2011) and consisted mainly of repetitive effusive eruptions through N-S oriented fissures along the Timpe fault system (Branca et al., 2011b). The products of this phase are related to the first primitive composite volcano interpreted as a lava shield elongated 22 km on an NNW-SSE basis in correspondence of the actual Acireale scarps on the east flank of the volcano (Branca et al., 2008, 2011b). During this eruptive period, sporadic eruptive activity affected also the lower southwestern and southeastern sectors of the Etna edifice. The products of this phase are mainly constituted by alkali-basaltic lavas (Branca et al., 2008; Corsaro and Pompilio, 2004).

The (3) Valle del Bove phase (**Fig. 1.10c**) occurred about 110 ka ago and the volcanism shifted from the Ionian coast to the area now occupied by the Valle del Bove. During this period the volcanic activity of Mt. Etna underwent a profound change: from the sporadic fissure eruption of the first two phases it shifted to a central-type polygenetic volcano (De Beni et al., 2011). During a period comprised from 110 ka and 65 ka ago (De Beni et al., 2011) about seven main volcanic centers took place. The principal activity occurred from Trifoglietto volcano (~107 – 99 ka ago) on the southern flank of Valle del Bove. It was mainly characterized by effusive lava flows and explosive activity during the final phases which ended with a Plinian eruption which generated a thick sequence of pumice and flow deposits

(Branca et al., 2011a). The Trifoglietto edifice reached a maximal elevation of about 2600 m (Branca et al., 2011b).

After the construction of volcanoes of the Valle del Bove the volcanism shifted NNW giving raise to the last (4) Stratovolcano phase (**Fig. 1.10d**). The composition of the erupted lava changed from alkali-basalt to trachytes (Corsaro and Pompilio, 2004) and was marked by the construction of Ellittico volcano, the main eruptive center recognized in Etna region. Ellittico volcano reached a maximal elevation of about 3600 m and was characterized by both explosive and effusive activity, most from the summit vents and subordinated flank fractures (Branca et al., 2011b).

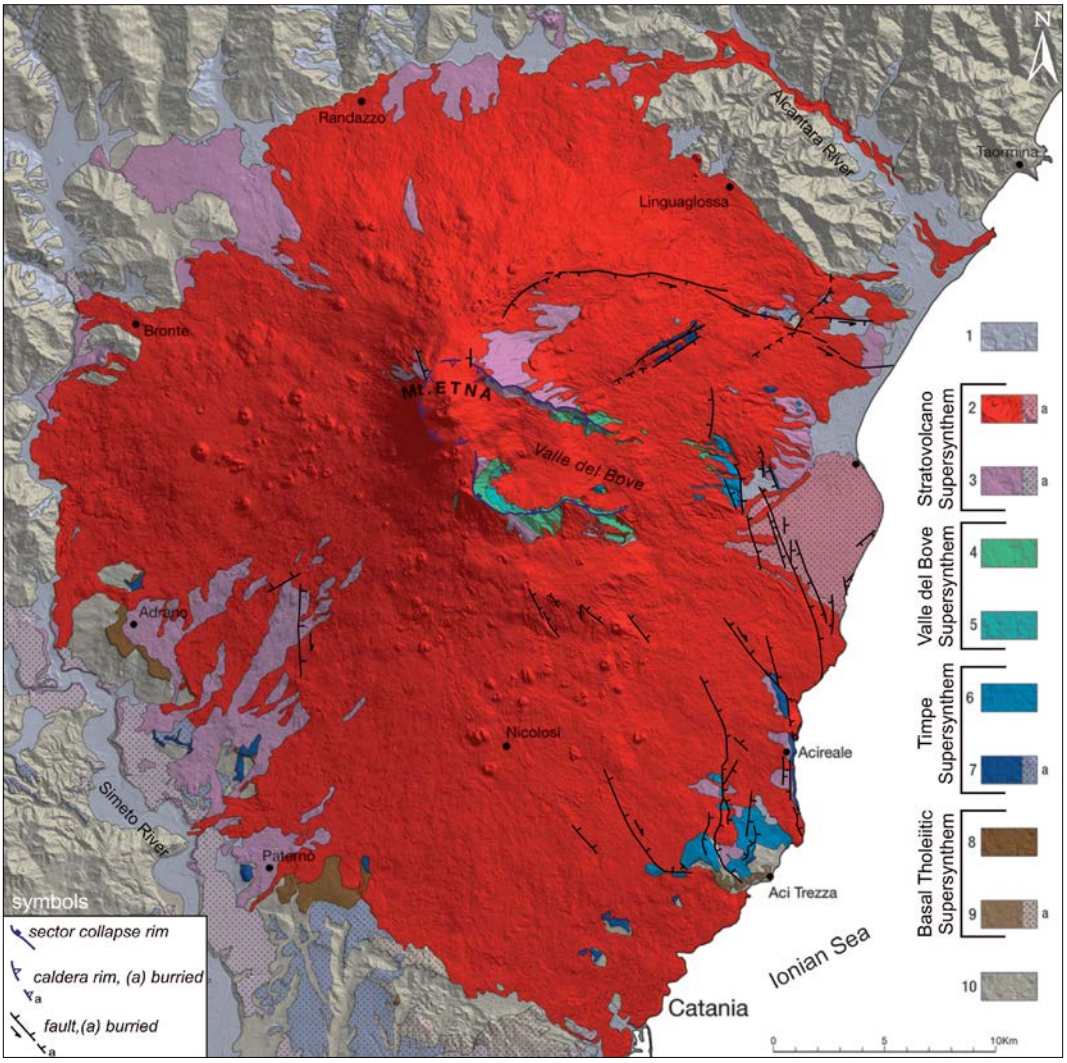

Figure 1.11. Scheme of the outcropping deposits of the four phases of volcanism on Mt. Etna volcano. (from Branca et al., 2011b).

Ellittico volcano began his growth about 57 ka ago and slowly expanded his flanks until it reached, almost 20 ka ago, its maximal areal expansion having a maximum diameter of about 45 km that corresponds to the actual boarders of Mt. Etna volcano (**Fig. 1.11**). The final stage of Ellittico volcano was characterized by four Plinian eruptions, occurring about 15.5 – 15 ka ago, which ended the Elittico phase and produced a collapse of the summit area which formed the Ellittico caldera (Branca et al., 2011b). Since 15 ka ago the volcanic activity shifted to the actual active vents at the summit of Mt. Etna, namely the Mongibello volcano was born. Effusive summit eruptions gradually filled the Ellittico caldera and many flank fissures generated lava flows which reached the Ionian coast.

About 10 ka ago a collapse involved the eastern flank of the Etna edifice and formed the huge collapse depression of the Valle del Bove (Calvari et al., 1994). In 122 BC the largest explosion of Mongibello occurred, this was a Plinian eruption (Coltelli et al., 1998) that produced widespread pyroclastic scoria fall deposits and huge damage to the ancient Roman town of Catania (Branca et al., 2011b). In 1669 the largest flank eruption of modern times occurred at low altitude in correspondence of Monti Rossi.

The lava flow reached and destroyed part of the town of Catania and many villages on the Etna steps. Since the 17th century the eruptive activity has been characterized by both periods of explosive activity (Strombolian to lava fountains) and the occurrence of sporadic flank activity which appear to have no systematic relationship with the central activity (Branca and Carlo, 2005).

1.2.2 Geodynamic framework

By a structural point of view, Mount Etna is located in a complex area characterized by different domains (**Fig. 1.12**).

Specifically, the volcano is located on the structural domain of the Catania-Gela foredeep chain and delimited by three geostructural units: the Appennine-Maghrebian Chain northward and westward; the Iblean foreland southward, belonging to the Pelagian block, the northernmost part of the African plate; the Ionian basin eastward, opened probably during the middle-late Mesozoic and aborted at some time during the Tertiary (Catalano et al., 2001).

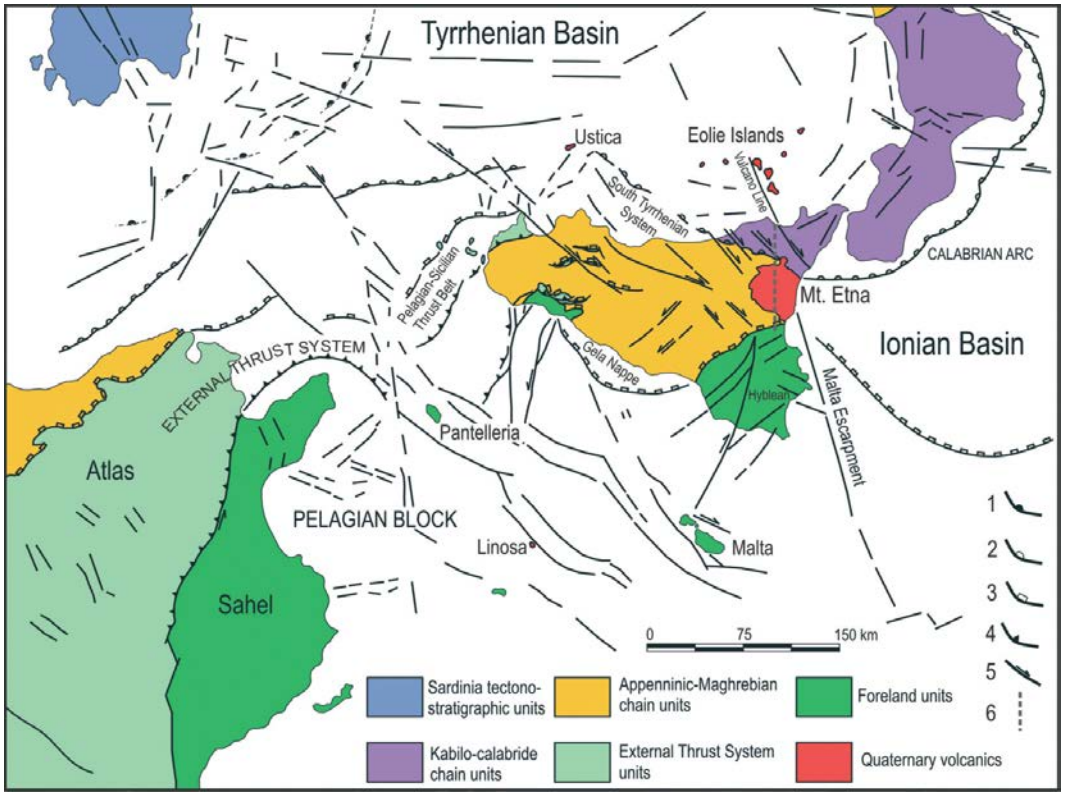

Figure 1.12. Structural setting of central Mediterranean Sea (from Lentini et al., 2006) and location of Mt Etna.

So, Mount Etna is located on the edge of two crustal domains, whose boundary lies a little further south than the volcano and corresponds to the Malta escarpment (Bousquet and Lanzafame, 2004, and reference therein). The faults of this topographic lineament have been named "Aeolian Maltese fault system".

This system extends (**Fig. 1.13**) from the Malta escarpment, along the south-eastern coast of Sicily, to the eastern base of Etna (Timpe faults), proceeding

across north-eastern Sicily before reaching the Tyrrhenian Sea, where the faults control the volcanism of the Vulcano-Lipari-Salina alignment.

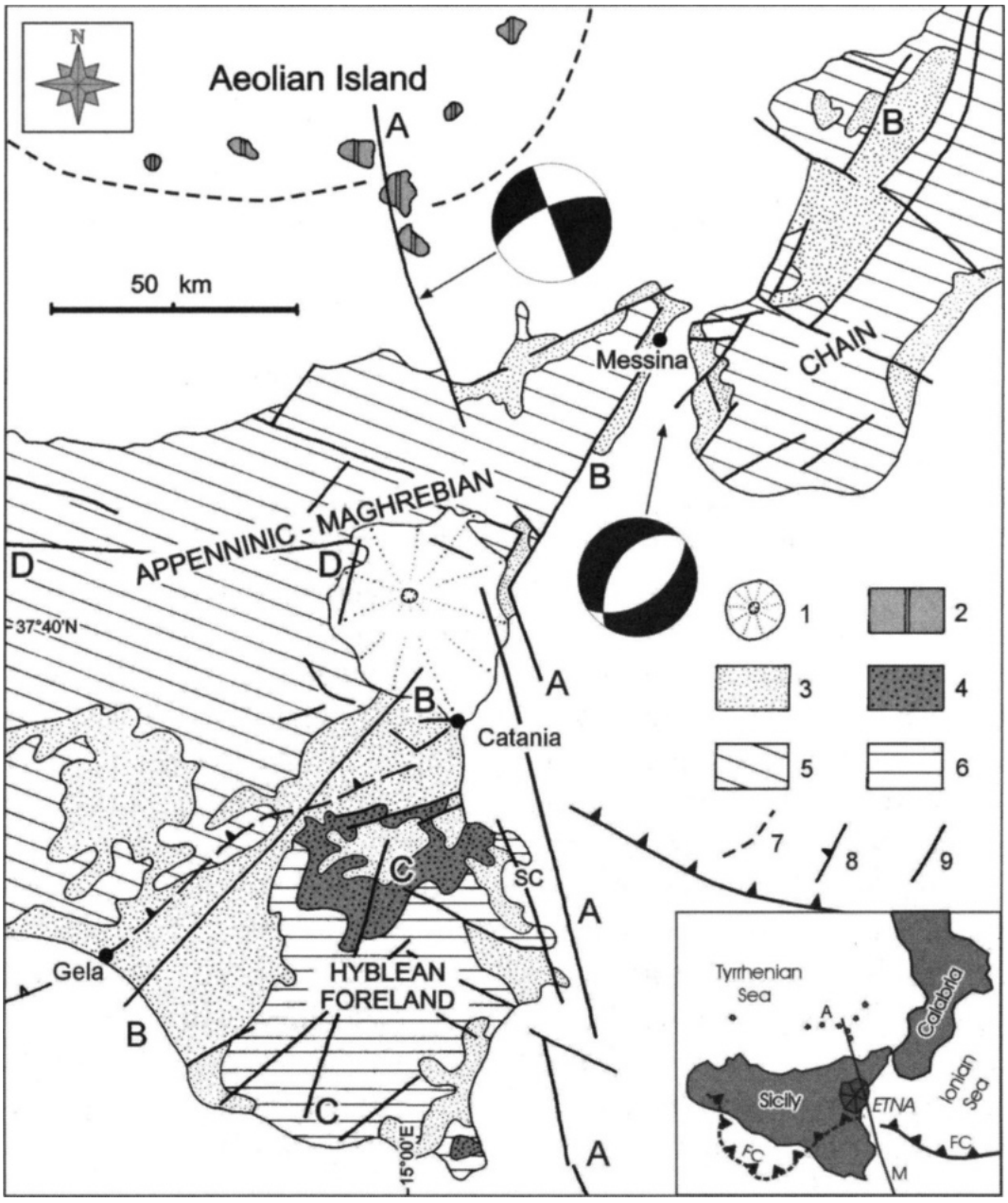

Figure 1.13. Structural sketch map of eastern Sicily and southern Calabria (from Bousquet and Lanzafame, 2004)

The Aeolian-Maltese fault system divides the Calabrian-Sicilian arc into two different sectors (Bousquet and Lanzafame, 2004): (1) to the east, the calcalkaline volcanism of the Aeolian islands (on the margin of the Tyrrhenian back-arc basin)

is active and the Ionian basin is subducted under Calabria; (2) to the west, the convergence due to subduction is blocked and the region is in a collisional regime. Mt. Etna, moreover, lies in the intersection zone of the major fault systems of eastern Sicily (Scicli and Comiso-Messina faults), and is bounded to the north by the eastern extension of the Monte Kumeta-Alcantara faults and to the east by the Aeolian-Maltese faults. The Etnean substratum is thus highly fractured: it is cut by steeper faults and, at the level of the nappes, has numerous gentle overthrusting planes.

The structural features about Mt. Etna are quite complex. To explain its origin different models have been proposed. The first models to explain the origin of the volcano were performed during the 70s; several authors (e.g. Ritmann, 1973; Cristofolini et al., 1979) proposed a model in which the intersection of three main fault systems, trending ENE, NNW and WNW, created a weakness zone of uprising magma.

In the late 90s, Gvirtzmann and Nur (1999) proposed that Mt. Etna has formed as a consequence of rollback (**Fig. 1.14**) of the Ionian slab underneath the Calabrian arc.

Substantially, the rollback mechanism could be explained as the Ionian slab slowly moving away (southeast) from the subduction zone due to the weight of the subducting plate.

This leads to the opening of a gap between the Ionian lithosphere and the African plate, gap which is filled by viscous material coming from the asthenosphere (Gvirtzman and Nur, 1999).

In the last two decades, several authors have proposed models in which the magmatism has been related to the instability of the eastern flank of the volcano. In particular, deformation measurements carried out by GPS, SAR and so on, suggest that the eastern flank of the volcano is sliding toward the sea.

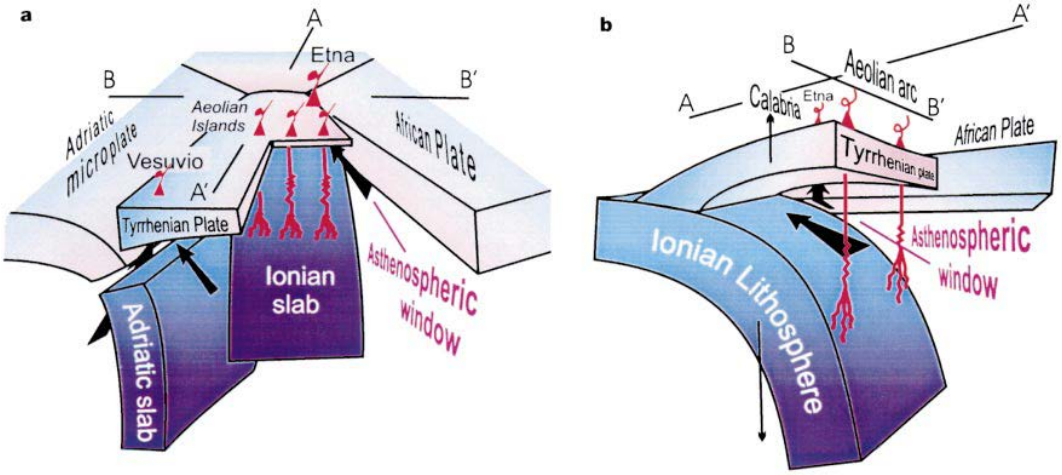

Figure 1.14. Three-dimensional sketch of the South Tyrrhenian subduction zone. Red lines represent magma rising from the top of the slab to the arc. Black arrows represent local patterns of mantle flow driven by slab motion. Notice that Etna is located outside the Aeolian arc and above a sideways mantle flow coming from under the African plate. **a**. A view toward the southeast from a point above the Tyrrhenian Sea. **b**. A view south and upward from a point under the Tyrrhenian plate (from Gvirtzman and Nur, 1999).

1.2.3 Structural framework

According to some authors, the structural framework of Mount Etna results from the complex interaction between regional tectonic, flank instability and basement geometry (e.g. Azzaro et al., 2013; Borgia et al., 1992; Bousquet and Lanzafame, 2004; McGuire and Pullen, 1989; Norini and Acocella, 2011; Rasà et al., 1996; Rust et al., 2005).

The main structural lineaments of the unstable flanks of Mt. Etna are the following fault systems (**Fig. 1.15**, Azzaro et al., 2013): Pernicana, Ragalna, Tremestieri-Trecastagni, Timpe and Ripe della Naca-Piedimonte-Calatabiano.

In particular, recent data obtained from different geophysical techniques have highlighted that the unstable flank of Etna is dismembered into different blocks, characterized by homogeneous kinematics (**Fig. 1.16**, Bonforte et al., 2011).

Seismic data in agreement with the high deformation rate recorded on the eastern/south-eastern flank of the volcano and geodetical data have highlighted

the current high dynamism of the eastern sector of the volcano (Bonaccorso et al., 2006; Bonforte et al., 2011; Azzaro et al., 2013).

The Pernicana fault system (PF) is identified as the northern boundary of this unstable sector (Alparone et al., 2013 and references therein) while the southern part is represented by the south-rift (Rasà et al., 1996) and the Tremestieri-Trecastagni faults systems (**Fig. 1.15**).

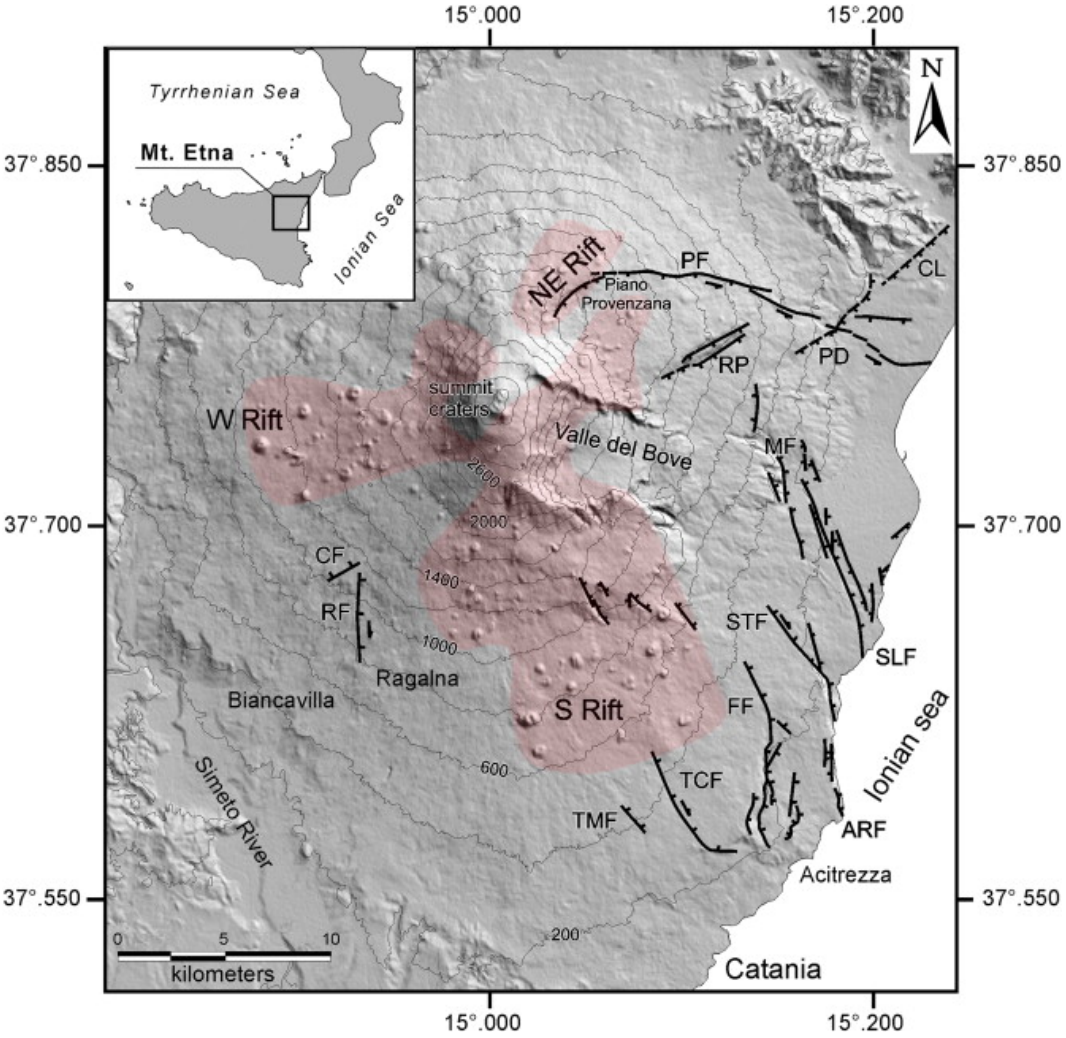

Figure 1.15. Tectonic sketch map of Mt. Etna defined by structures with morphological expression. Fault abbreviations: PF, Pernicana; RF, Ragalna; CF, Calcerana; TMF, Tremestieri; TCF, Trecastagni; FF, Fiandaca; ARF, Acireale; STF, S. Tecla; MF, Moscarello; SLF, S. Leonardello; RF, Ragalna; RP, Ripe della Naca; PD, Piedimonte; CL, Calatabiano. The arrows indicate the strike-slip component, the contour of the rift zones is in red (from Azzaro et al., 2013).

These structures join with a displacement plane located roughly at a depth of 2-4 km b.s.l. which also corresponds to the maximum depth of the earthquakes recorded along the Pernicana fault (Alparone et al., 2013). The sliding of the eastern flank of the volcano towards the sea is thought to favor the extension and the depressurization of the central part of the volcano thus facilitating magma ascent at shallower levels (Bonaccorso and Patanè, 2001). The relation between the unstable condition of sliding flank and the magmatic system was also confirmed by Privitera et al. (2012) through the computation of Coulomb stress changes retrieved from numerical simulations of volcanic-tectonic events.

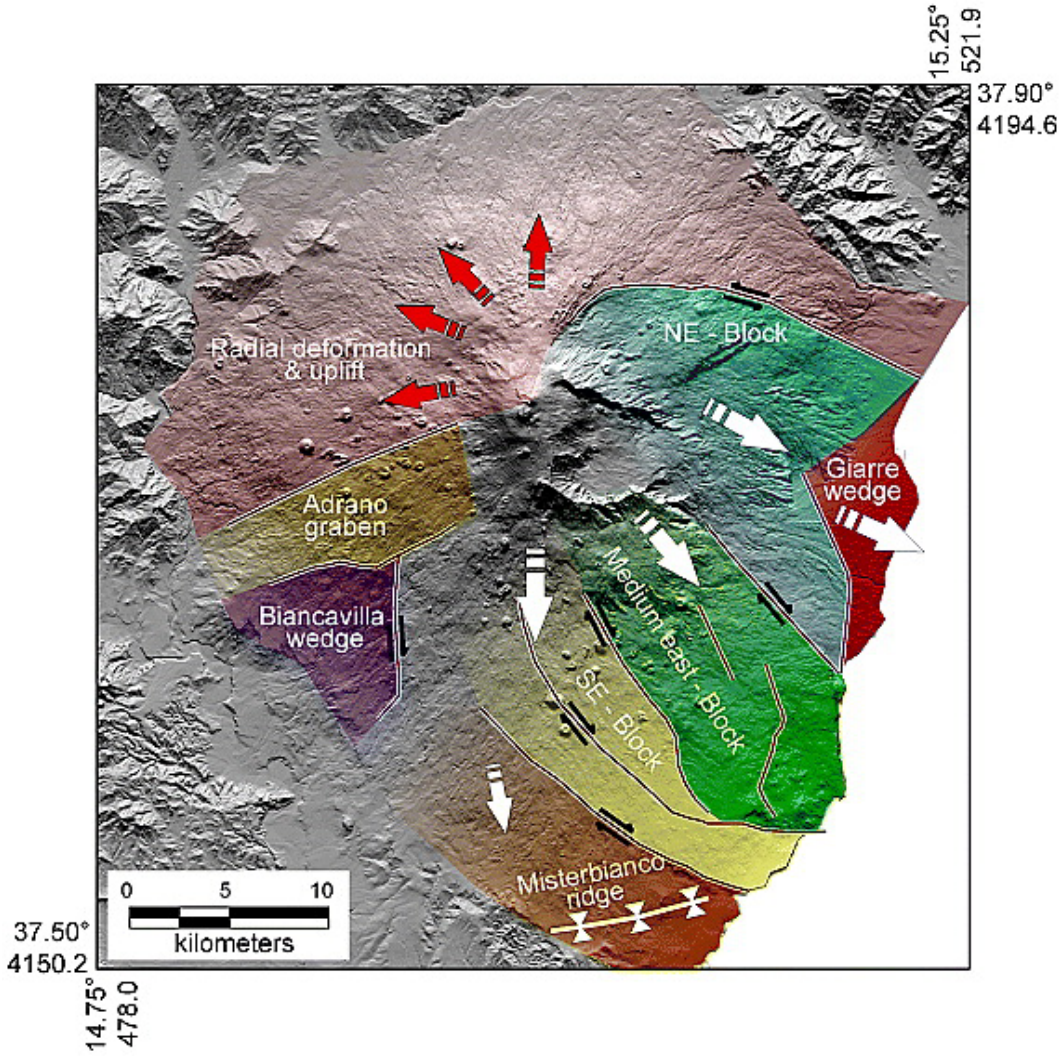

Figure 1.16. Main kinematic domains of Mount Etna volcano (from Bonforte et al., 2011).

1.2.4 Volcanic tremor at Mt. Etna

Mount Etna volcano is characterized by a wide spectrum of volcano-seismic signals such as VT-A, VT-B, LP events, VLP events, explosion-quakes and volcanic tremor. Here, we focus on volcanic tremor, that is the main topic of this thesis. Volcanic tremor is a typical seismic signal that is generally observed at many different volcanoes in the world. Due to its close relationships with magmatic and hydrothermal activity within the volcano's feeding system (e.g., Kostantinou and Schlindwein, 2002), volcanic tremor is frequently used to study volcanic activity. Several models have been proposed to explain the source mechanism of volcanic tremor, though all authors concord in attributing its origin to the complex interplay among the magmatic-hydrothermal fluids and their hosting rocks.

As observed in many other basaltic volcanoes with persistent activity such as Stromboli (e.g. Langer and Falsaperla, 1996), Mt. Etna volcanic tremor is characterized by continuity in time. Therefore, variations in time of the signals (for example, in amplitude) can be used to detect short/long-term variations in the magma ascent. Example of such variations are the episodes of lava fountains.

At Mt. Etna, the first instrumental observations of volcanic tremor were performed by Schick and Riuscetti (1973). Successively, numerous different studies followed, leading to often contrasting conclusions about its source mechanism, that highlight the complexity of the problem.

Sometimes is possible to observe that typical volcanic tremor is accompanied or substituted by a "banded tremor", as occurred during March-May 1987 (Gresta et al., 1996) and in August-October 2008 (Cannata et al., 2010b). These authors found that this "banded tremor" was characterized by different spectral content wavefield and location of the source compared to the "ordinary tremor", suggesting different sources for the two kinds of tremor. Moreover, they hypothesized that hydrothermal fluids are responsible for the banded tremor generation, while magma only plays a passive role, specifically as a heat source. Focusing on the "ordinary volcanic tremor", it has always been observed in concomitance with degassing, explosive and/or effusive activity from either the

summit or flank craters (e.g. Del Pezzo et al., 1993; Falsaperla et al., 1994; Alparone et al., 2003; Privitera et al., 2003), often showing variations in amplitude, spectral content, wavefield features and source location, concurrently with changes in volcanic activity (Alparone et al., 2007; Di Grazia et al., 2006, 2009; Patanè et al., 2008; Cannata et al., 2009a,b).

During paroxysmal events, such as vigorous and sustained lava fountains, tremor amplitude is correlated well with the height and duration of this kind of activity (Alparone et al., 2003; Privitera et al., 2003; Carbone et al., 2006; Patanè et al., 2013). A contribution from deeper sources has also been inferred on the basis of the spatial distribution of seismic amplitudes and polarization attributes (Alparone et al., 2003; Privitera et al., 2003; Di Grazia et al., 2006, 2009).

At Mt. Etna, monitoring of volcanic tremor, as well as all the volcanic-seismic signals, is carried out by Istituto Nazionale di Geofisica e Vulcanologia – Osservatorio Etneo (INGV – OE). Below, the main characteristics of the seismic network (Sec. 1.2.4.1) will be described.

1.2.4.1 Seismic Monitoring network

At Mt. Etna, the permanent seismic network, run by the INGV-OE, comprises 33 broadband and 12 short-period stations. The analyses of seismo-volcanic signals are performed on the recordings of 19 of these stations, each equipped with a broadband (40 s cutoff period), three-component Trillium seismometer (Nanometrics™) and acquired in real time at sampling rate of 100 Hz (**Fig. 1.17**). It is worth noting that two of these stations (EBEL and ETFI) were destroyed during the paroxysmal episodes of 28 February and 11 November 2013, respectively (Cannata et al, 2015).

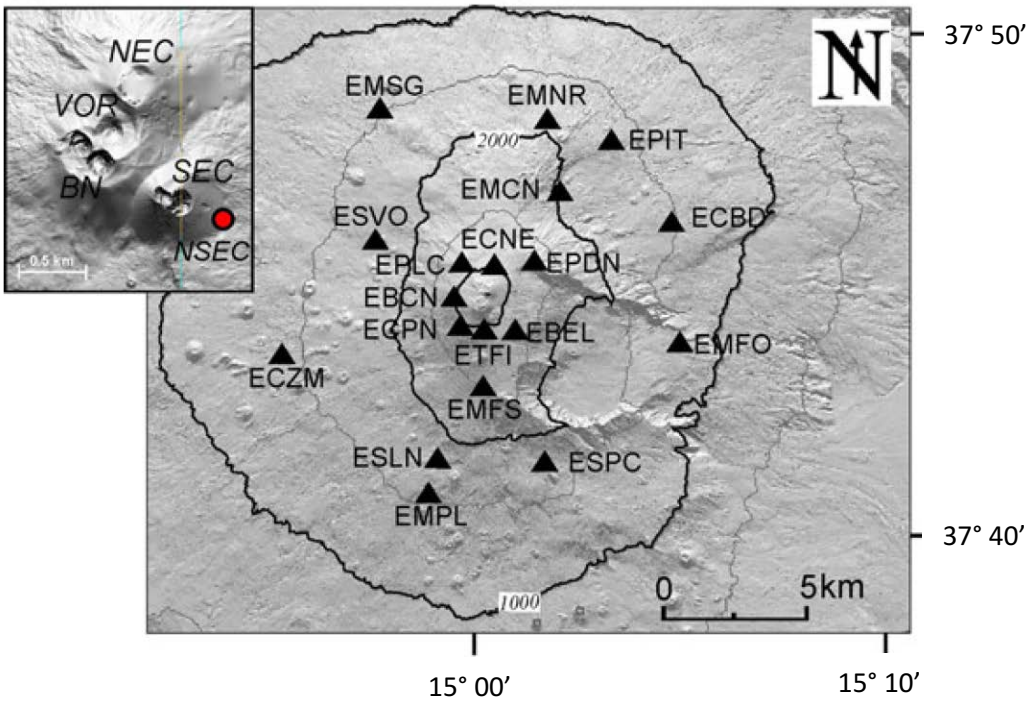

Figure 1.17. Digital Elevation Model of Mt. Etna with the location of the broadband seismic stations. The digital elevation model in the upper left corner shows the distribution of the five summit craters (VOR Voragine, BN Bocca Nuova, SEC Southeast Crater, NEC Northeast Crater and the New SEC (NSEC), indicated by the red dot. The black concentric lines in (a, b) are altitude contour lines from 1 to 3 km a.s.l. with spacing of 1 km (from Cannata et al., 2013).

1.2.5 Volcanic framework during 2011-2012 activity

From January 2011 to the end of April 2012 Mt. Etna was characterized by intense volcanic activity at the summit craters area. This period was preceded by a relatively quiet period from July 2009 to the end of 2010, when there was a modest explosive activity at a pit crater on the east flank of the South-East Crater (SEC), at Bocca Nuova (BN) and at North-East Crater (NEC) (e.g., Andronico et al., 2013; Patanè et al., 2013).

Subsequently, since the first days of January 2011 it was possible to observe an intensification of volcanic activity, which began with Strombolian activity at the pit crater near the SEC, culminating in a paroxysmal episode at the same crater on 12 January. This was the first of a series of 25 paroxysmal episodes that occurred between January 2011 and April 2012; these events produced a total volume

(bulk) of volcanic products of ~50x10^6 m^3. A portion of these products (~19x10^6 m^3) built a new summit crater cone called New South-East Crater (NSEC; Behncke et al., 2014). The 25 paroxysmal episodes did not take place with a constant rate over the period, but it was possible to identify three different periods of alternating phases of relative quiet, each with a different number of paroxysmal episodes and frequency of occurrence. Specifically, it was possible to identify the following phases (***Tab. 1.1***):

- ***Phase 1***: from January to May 2011 --> 4 episodes of lava fountaining;
- ***Phase 2***: from July to November 2011 --> 14 episodes of lava fountaining;
- ***Phase 3***: from January to April 2012 --> 7 episodes of lava fountaining

The paroxysmal episodes between 2011 and 2012 were characterized by a similar dynamics (e.g., Behncke et al., 2014**;** Viccaro et al., 2014) with a succession of different stages of activity: (i) reactivation of crater with minor explosive activity; (ii) Strombolian activity often accompanied by emission of lava flows; (iii) lava fountaining; (iv) progressive decrease in the intensity of the lava fountaining gradually replaced by a weak Strombolian activity and subsequent resting phase until the successive paroxysmal episode. Despite common evolutionary stages among the examined paroxysmal events, significant differences were found in the initial stages: in fact, some events, such as the 12 January episode, showed a stage (ii) with prolonged Strombolian activity (up to a few days), while other events were marked by a stage (ii) from 1h to 8h prior to evolve into lava fountaining (Behncke et al., 2014).During the same time interval, the crater BN in the months from June to July 2011 showed explosive activity with ash emissions which culminated in intra-crater Strombolian activity. The same type of activity occurred at BN craters during 2012 in the periods between June-August and October-November (Viccaro et al., 2014). Finally, the degassing activity was persistent throughout the period considered at the craters BN, NEC and NSEC (e.g., Behncke et al., 2014**;** Viccaro et al., 2014). **Fig. 1.18** summarizes the volcanic activity recorded at the summit craters of Mt. Etna during 2011-2012.

Date	Episode	Reactivation	Start Strombolian	Start lava emission	Start fountaining	End fountaining	End episode	Full episode duration (h_min)	Lava fountain duration (h_min)	
12/1/11	01	2/1/11 16:00	11/1/11 8:00	12/1/11 20:10	12/1/11 21:50	12/1/11 23:50	13/1/11 2:00	42_00	2_00	
18/2/11	02	18/2/11 1:00	18/2/11 1:45	18/2/11 12:00	18/2/11 3:30	18/2/11 12:30	18/2/11 13:17	12_20	9_00	
10/4/11	03	29/3/11 8:00	8/4/11 6:00	9/4/11 17:55	10/4/11 8:05	10/4/11 13:30	10/4/11 14:03	56_00	5_25	PHASE I
12/5/11	04	8/5/11 6:00	11/5/11 17:00	11/5/11 20:30	12/5/11 3:20	12/5/11 5:00	12/5/11 5:55	96_00	1_40	
9/7/11	05	4/7/11 7:00	7/7/11 20:00	9/7/11 12:05	9/7/11 13:45	9/7/11 14:45	9/7/11 15:30	128_30	1_00	
19/7/11	06	16/7/11 8:00	18/7/11 17:00	19/7/11 0:00	19/7/11 0:05	19/7/11 2:30	19/7/11 3:00	67_00	1_25	
25/7/11	07	24/7/11 16:00	24/7/11 18:00	25/7/11 1:30	25/7/11 3:00	25/7/11 5:00	25/7/11 5:30	13_30	2_00	
30/7/11	08	28/7/11 20:00	30/7/11 7:50	30/7/11 17:30	30/7/11 19:35	30/7/11 21:30	30/7/11 22:00	50_00	2_00	
5/8/11	09	5/8/11 16:00	5/8/11 17:00	5/8/11 20:15	5/8/11 21:00	5/8/11 23:00	6/8/11 0:15	8_15	2_00	
12/8/11	10	11/8/11 3:30	12/8/11 5:30	12/8/11 7:50	12/8/11 8:30	12/8/11 10:00	12/8/11 11:00	31_30	1_30	
20/8/11	11	19/8/11 3:36	20/8/11 2:00	20/8/11 2:55	20/8/11 7:00	20/8/11 7:30	20/8/11 7:50	28_15	0_30	
29/8/11	12	28/8/11 0:52	28/8/11 18:00	29/8/11 3:15	29/8/11 4:05	29/8/11 4:40	29/8/11 5:15	28_30	0_35	PHASE II
8/9/11	13	6/9/11 12:00	8/9/11 5:30	8/9/11 6:50	8/9/11 6:30	8/9/11 8:30	8/9/11 8:45	45_15	2_00	
19/9/11	14	16/9/11 10:27	19/9/11 2:00	19/9/11 6:30	19/9/11 12:20	19/9/11 13:00	19/9/11 13:10	74_30	0_40	
28/9/11	15	28/9/11 8:00	28/9/11 17:30	28/9/11 19:15	28/9/11 19:31	28/9/11 19:55	28/9/11 20:10	12_10	0_24	
8/10/11	16	8/10/11 11:00	8/10/11 11:24	8/10/11 13:30	8/10/11 14:30	8/10/11 14:50	8/10/11 17:45	6_45	0_20	
23/10/11	17	23/10/11 17:13	23/10/11 17:40	23/10/11 18:07	23/10/11 18:30	23/10/11 20:30	23/10/11 21:15	4_00	2_00	
15/11/11	18	15/11/11 6:00	15/11/11 8:00	15/11/11 6:00	15/11/11 11:00	15/11/11 12:29	15/11/11 13:00	7_00	1_29	
5/1/12	19	4/1/12 8:00	4/1/12 16:00	5/1/12 2:45	5/1/12 5:00	5/1/12 6:50	5/1/12 8:30	24_30	1_50	
9/2/12	20	27/1/12 11:24	27/1/12 21:40	8/2/12 19:00	9/2/12 0:00	9/2/12 5:30	9/2/12 9:00	309_30	5_30	
4/3/12	21	16/2/12 0:00	16/2/12 20:00	4/3/12 6:00	4/3/12 7:30	4/3/12 9:32	4/3/12 9:32	417_30	2_02	
18/3/12	22	16/3/12 0:00	17/3/12 20:00	18/3/12 5:55	18/3/12 8:00	18/3/12 9:45	18/3/12 10:10	58_10	1_45	
1/4/12	23	26/3/12 0:00	30/3/12 18:30	1/4/12 1:00	1/4/12 2:00	1/4/12 3:30	1/4/12 4:30	154_10	1_30	PHASE III
12/4/12	24	10/4/12 17:50	11/4/12 19:00	12/4/12 12:25	12/4/12 14:30	12/4/12 15:15	12/4/12 16:00	46_10	0_45	
24/4/12	25	21/4/12 10:00	23/4/12 17:00	23/4/12 0:00	24/4/12 1:30	24/4/12 2:20	24/4/12 2:40	64_20	0_50	

Table 1.1. Timing of the various eruptive activities recognized for each episode and duration both of the lava fountaining phases and the full episodes. (Behncke et al., 2014 - mod.)

35

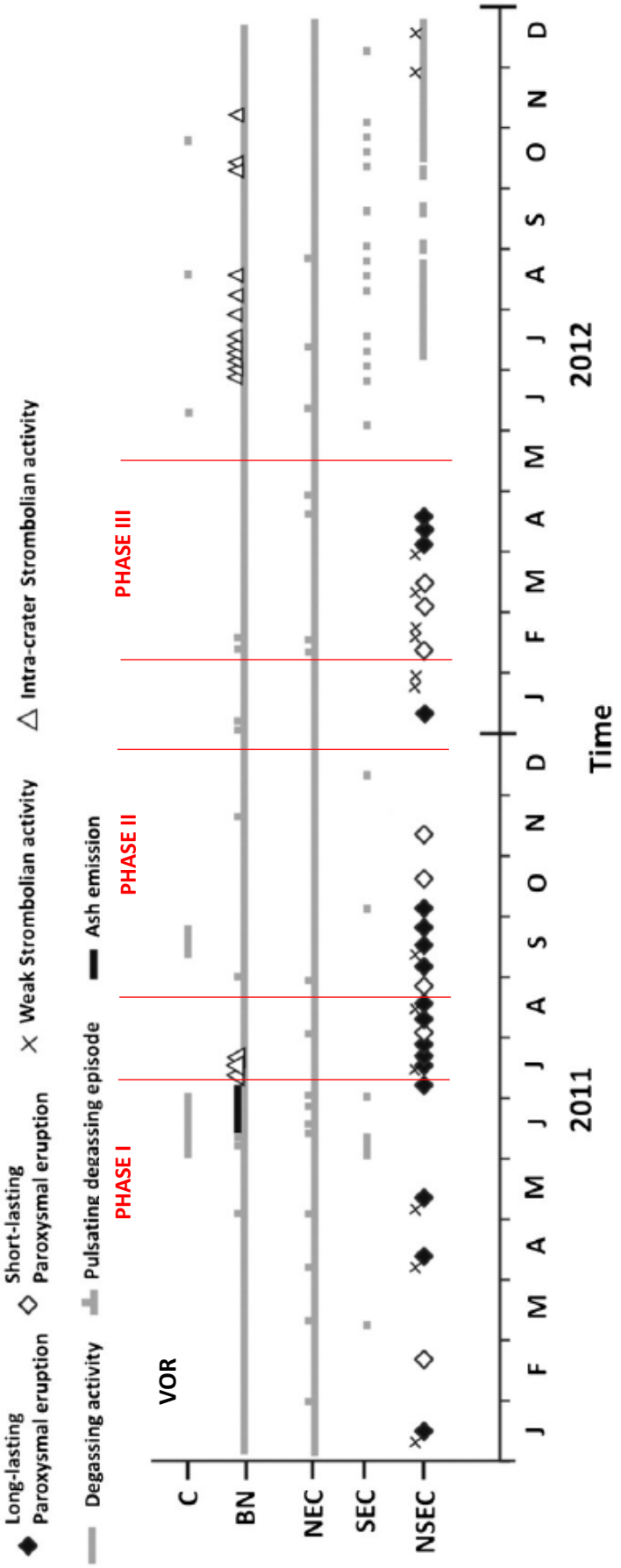

Figure 1.18. Plot summarizing the eruptive activity during 2011-2012 at Voragine (VOR), Bocca Nuova (BN), North East Crater (NEC), South East Crater (SEC) and New South East Crater (NSEC). (Viccaro et al., 2014 - mod.)

1.3 METHODS OF ANALYSIS ROUTINELY PERFORMED TO MONITOR VOLCANIC TREMOR AT MT. ETNA

As seen previously, the persistent activity at Mt. Etna generates a continuous seismic signal, mainly composed of volcanic tremor. In order to identify variations in the volcanic state activity, variations of the main characteristics of volcanic tremor (for example, amplitude, spectral content and source location) are routinely detected, to provide important information for monitoring purposes important information for monitoring purposes.

Below, the main methods of analysis for the study of volcanic tremor will be illustrated.

- *Spectral analysis*

1. *Fourier Transform*

As aforementioned, to successfully investigate the nature of the volcanic tremor, it is necessary to analyze its frequency content. Frequency representation is commonly computed by Fourier transform that breaks a signal down into constituent sinusoids of different frequencies allowing the retrieval of information on power content at any frequency. The equation to perform Fourier transform analysis is the following one (e.g. Papoulis, 1987):

$$X(\omega) = \int_{-\infty}^{+\infty} x(t) e^{-i\omega t} dt \qquad (1.1)$$

where t and ω are time and angular frequency, respectively, $x(t)$ and $X(\omega)$ are the signal in time and frequency domains, respectively, i is equal to $\sqrt{-1}$. One of the most efficient and popular algorithms to implement the Fourier transform is the Fast Fourier Transform (FFT), developed by Cooley and Tukey (1965).

When looking at a Fourier transform of a signal, it is impossible to tell when a particular event took place. If the signal properties do not change much over time (stationary signal) this drawback is not very important.

2. Short Time Fourier Transform

Most interesting signals in geophysics contain numerous non-stationary or transitory characteristics: drift, trends, abrupt changes, and onsets and ends of events. These characteristics are often the most important part of the signal, and Fourier analysis is not suited to detecting them. Time localization can be obtained by windowing the data at different times with sliding window functions w(t). The Fourier transform of this procedure is called Short-Time Fourier transform (STFT) or spectrogram. It is defined as (Lesage et al., 2002):

$$STFT_f^{(g)} = \int_{t'} [x(t') \cdot w^*(t - t')] \exp(-2i\pi\omega t')\, dt' \qquad (1.2)$$

where $w*$ is the complex conjugate of w. The STFT at a given time t is the Fourier transform of the signal $x(t')$ multiplied by a shifted analysis window $w*(t - t')$ centered on t. The STFT can be seen as a local spectrum of the signal $x(t')$ around the analysis time t.

Therefore, the STFT represents a sort of compromise between the time- and frequency-based views of a signal. It provides some information about both when and at what frequencies a signal event occurs. However, we can only obtain this information with limited precision, and that precision is determined by the size of the window. It is clear that a good time resolution of the STFT requires a narrow window in time. In contrast, a good frequency resolution of the STFT requires a narrow filter in the frequency domain (and then a large window in time). Unfortunately, Heisenberg's uncertainty principle prohibits the existence of a window with arbitrarily small duration and small bandwidth. It is well known that

once a window function $w(t)$ is chosen, both time and frequency resolutions are fixed. This means that for any given t and ω, the frequency resolution in time is fixed, and the entire phase space is uniformly described by cells of fixed sizes. Thus, the STFT is inadequate for the study of signals with different size features because it is not possible to design an optimal window for analyzing the process.

3. Wavelet Transform

For spectral analysis, in order to overcome the limitations of Fourier Transform and STFT analysis it is possible to make use of Wavelet analysis. In particular, it overcomes the limitations of the STFT and can give a more accurate time-frequency description of signals containing low and high-frequency components.
Wavelet analysis allows the use of long-time intervals where we want more precise low-frequency information, and shorter regions where we want high-frequency information.
This is achieved by using analyzing functions called wavelets, which are characterized by two parameters, the translation parameter as in the STFT, and the dilatation parameter, which controls the time duration of the wavelet. When these parameters take continuous values, the operation is called continuous wavelet transform (CWT) (Lesage et al., 2002). The CWT is defined in the time frequency domain as (Bartosch and Seidl, 1999):

$$CWT_{a,t'} = \frac{1}{\sqrt{a}} \int_{-\infty}^{+\infty} x(t)\, \Psi\left(\frac{t - t'}{a}\right) \tag{1.3}$$

where a is the scale, t' is the translation, Ψ is the analyzing wavelet. There are different types of analyzing wavelet such as Daubechies, Haar, Coiflets, Symlets, Morlet Mexican Hat, Gaussian. The choice of the analyzing wavelet is neither unique nor arbitrary. It must be a zero-mean function with unit energy and compact support (i.e., with sufficiently fast decay) to obtain localization in time. Among the many available wavelets, the Morlet wavelet has been widely used in

geophysics. It is a complex wavelet, which is able to extract information on both the amplitude and phase.

In the **Eq. 1.3** the frequency parameter is not mentioned. A way to turn the scale a into frequency ω it is to compute the centre frequency F_c of the wavelet and to use the following relationship (Abry, 1997):

$$F_a = \frac{F_c}{\Delta t \cdot a} \tag{1.4}$$

where Δt is the sampling rate, F_a is the frequency (also called "pseudo-frequency") corresponding to the scale a. The main difference between STFT and CWT is the distinct behaviour of the time-shift/frequency-shift operators. Whereas the effective duration and bandwidth of the STFT are independent of the analysis frequency ω, the effective duration of the CWT is inversely proportional to ω, and the bandwidth is proportional to ω (Kumar and Foufoula-Georgiou, 1997).

Both of these techniques have the same time-frequency resolution limitations (time resolution and frequency resolution cannot be made arbitrarily good simultaneously).

However, while the STFT resolution does not depend on the analysis frequency, the CWT has better time resolution and poorer frequency resolution at high frequency and better frequency resolution and poorer time resolution at low frequency (Lesage et al., 2002). The CWT technique was applied on seismic and infrasonic signals in several papers, such as Wasserman (1997), Bartosch and Seidl (1999), Lesage et al. (2002) and Lesage (2008).

- *Amplitude analysis*

The investigation of the time variation of the seismic amplitude is performed by the Root Mean Square (RMS) amplitude analysis. The RMS amplitude value of a

set of samples of a waveform is the square root of the arithmetic mean (average) of the squares of the original values. Since the amplitude of signals is usually observed in separate frequency bands, signals must be band-pass-filtered before calculating the RMS. Therefore, considering a signal x_i, and ($i = 0, 1, \dots, N-1$ is a segment of the signal encompassing N points) filtered in a specified frequency band, the RMS amplitude is calculated as (e.g. Battaglia and Aki, 2003):

$$RMS = \sqrt{\frac{1}{N}\sum_{i=0}^{N} x_i^2\,(t)} \tag{1.5}$$

Alternatively, the RMS amplitude can be computed in the frequency domain, using Parseval's theorem. In this case, applying the discrete Fourier transform to the signal x_i, the RMS amplitude of the unfiltered signal is (e.g. Battaglia and Aki, 2003):

$$RMS = \sqrt{\frac{1}{N}\sum_{k=0}^{N} [X_k]^2} \tag{1.6}$$

where X_k, with $k = 0, 1, \dots, N-1$, represents the frequency spectrum of the time-domain signal x_i.

Considering a specific frequency band, it is possible to calculate the RMS as the sum over the chosen part of the spectrum. For continuous signals, the RMS amplitude value is much more stable than the peak-to-peak amplitude which may be strongly influenced either by a single peak in the signal or by a technical glitch. One of the best ways to monitor and detect any variations in the volcanic tremor signal can be considered the spectrogram. As time elapses, this type of representation allows to display all the variables indicative of the change in the properties of the volcanic tremor, such as amplitude and frequency content.

- *Source Location (amplitude decay method)*

In the case of the Mt. Etna volcano, for the localization of volcanic tremor the recourse to the method based on the decay of the seismic amplitudes, proposed by Di Grazia et al. (2006) and Patanè et al. (2008) is consolidated. Assuming that seismic waves propagation occurs in a homogeneous medium, this methodology is based on 3D grid search approach centered under the summit craters (e.g. Gottschammer and Surono, 2000; Battaglia et al., 2005; Di Grazia et al., 2006). The decay of the seismic amplitude A_0 is related to the distance r by equation

$$A(f,r) = A_0(f) r^{-b} e^{-\alpha r}, \quad con\ \alpha = \frac{\pi f}{Qc} \tag{1.7}$$

where f is the characteristic frequency of the seismo-volcanic signal, c is the seismic velocity of propagation in the considered homogeneous medium, b is the value of the exponent that assumes values of 0.5 for surface waves and of 1.0 for body waves, α is the absorption coefficient as a function of frequency and Q is the quality factor. The equation (1.7) can be linearized taking into account the logarithm of both members (Di Grazia et al., 2006; Cannata et al., 2010) in order to obtain the following relation:

$$\ln A_i + \alpha r_i = lnA_0 - blnr_i \tag{1.8}$$

where A_i is the signal amplitude in terms of the RMS evaluated at the i-th station, r is the distance between the source and the i-th station and A_0 is the amplitude of the signal at the source; in particular, the RMS values are calculated in a specific frequency band in order to isolate the contribution of a single source; moreover, in equation (1.8) lnA_0 and b can be considered the intercept and the slope of the linearised equation, respectively.

Seismo-volcanic signals are usually the result of the superposition of different terms such as the volcanic tremor (continuous signal) and any transients of signal

such as tectonic and VT earthquakes, LP events, VLP events, etc. In order to consider the volcanic tremor and possibly remove the contribution of any transients, Di Grazia et al. (2006) suggest that, firstly, the signal is filtered in the frequency band characteristic for the considered volcano. Subsequently, for the calculation of the amplitude in terms of RMS (resulting from the 3 components of the seismic signal) the signal will be divided into fixed time windows (for example of 10 seconds). From the set of RMS values obtained for a larger window (for example of 5 or 15 minutes) the representative RMS amplitude value will be determined, taking into consideration the 25th percentile instead of, for example, the average; specifically, the percentile x_p of a given data set is defined such that the percentage $p\%$ of values is lower than x_p, while $(1-p)\%$ of the values are higher than x_p.

CHAPTER 2 – MULTIPARAMETRIC APPROACH FOR QUANTITATIVE COMPARISON OF VOLCANOLOGICAL TIME SERIES

2.1 INTRODUCTION

Modern volcanic monitoring techniques are based on the simultaneous study of different geophysical, geochemical and volcanological parameters, some of which are able to provide immediate results while others require more time due to a more complex analysis work (McNutt, 2000). The systematic control of the different data is usually carried out both during the phases in which eruptive events take place with the aim of studying their evolution, and during the phases in which the eruptive events do not occur and this in order to identify precursors which, however, may suggest a medium to short term eruption.

Therefore, the availability of different data for the study of the different phases of volcano activity and the ever-increasing computing power allowed the development of study with multiparametric approach for a reliable interpretation of the eruptive dynamics and structures that characterize a volcano.

During the last twenty years, several studies have been carried out in order to quantify the relationship between different parameters of the activity of a volcano. For example, McNutt (1994) was one of the first authors that have been quantitatively studying different volcanological monitoring data; specifically, the author applied linear regression analysis between tremor data with distinct volcanological data such as Volcanic Explosivity Index (VEI) and Ash Cloud Height for different volcanoes. Bani and Lardy (2007), instead, carried out a correlation analysis between seismic events and SO_2 emission rates in order to understand the eruptive dynamics during the activity at Yasur volcano (Vanuatu) from April 2004 to November 2005. Similar studies have been conducted in other volcanoes: for example, Palma et al., (2008) have taken into consideration correlation between volcanic tremor amplitude and SO_2 emission rate to study the activity at Villarica volcano (Chile), that occurred during November 2004 to January 2005, while Nadeau et al., (2011) carried out a correlation analysis between volcanic tremor and SO_2 emission rates in order to understand the eruption dynamics during the activity at Fuego volcano (Guatemala) in January 2009 and provided new insight into the system's shallow conduit processes. Martini et al. (2009) used

cross-correlation and randomized cross-correlation analysis to study the relationship between volcanic tremor and rainfall rates at Fogo volcano (Azores) during 2003-2004 activity. In addition, Ichihara et al. (2012) computed the cross-correlation function of vertical ground motion generated by infrasound, and the infrasound itself and apply this method to study activity at Asama volcano (Japan) during 2 February 2009 and at Shinmoe-dake volcano (Japan) during January 2011. Multiparametric quantitative analyses were also performed at Mt. Etna volcano. For example, Leonardi et al. (2000) carried out a cross-correlation analysis between volcanic tremor and the emission of SO_2 flux at craters for the study of the volcanic activity observed during the period 1987-1995. By cross-correlation, wavelet coherence and wavelet cross spectrum analysis, Cannata et al. (2010) have shown significant trends from the comparison between the emission rates of the soil CO_2 flux and the volcanic tremor acquired during the November 2002 - January 2006. Finally, Zuccarello et al. (2013) have shown significant trends from the comparison between the emission rates of the SO_2 flux and seismic data time series, such as volcanic tremor amplitude and cumulative volume changes, calculated by VLP counts acquired during the activity between December 2005 to January 2006. Finally, considering the eruptive activity at Mt. Etna between 2007 and 2008, Salerno et al. (2018) have shown the coupling between magmatic degassing and volcanic tremor by non-parametric Spearman's Rank correlation analysis. For extended periods, they have highlighted that the volcanic tremor and SO_2 flux signals on Mt. Etna are strongly correlated, while they attribute periods of low correlation between tremor and SO_2 flux to a different degassing regime, dominated by flux of gas from depth.

In the following paragraphs of this chapter, a quantitative multiparametric study of the activity at Mt. Etna volcano during the 2011-2012 period will be illustrated, in order to investigate the volcano dynamics. For this study, four different techniques of investigation were used: Cross Correlation (CC); Randomized Cross Correlation (RCC); Wavelet Coherence and Cross Wavelet Spectrum (WC and CWS); Linear regression and coefficient of determination (LR).

2.2 METHODS OF ANALYSIS FOR TIME SERIES QUANTITATIVE COMPARISON

In order to investigate possible relationship between the amplitude of volcanic tremor and other volcanological parameters, four different methods of analysis were chosen:

- Cross Correlation (CC);
- Randomized Cross Correlation (RCC);
- Wavelet Coherence and Cross Wavelet Spectrum (WC and CWS);
- Linear regression and coefficient of determination (LR).

In the following paragraphs I will describe the techniques with an example in which the four different methods were applied and tested on two synthetic signals obtained by summing Ricker wavelets with red noise (the type of noise expected in geophysical signals).

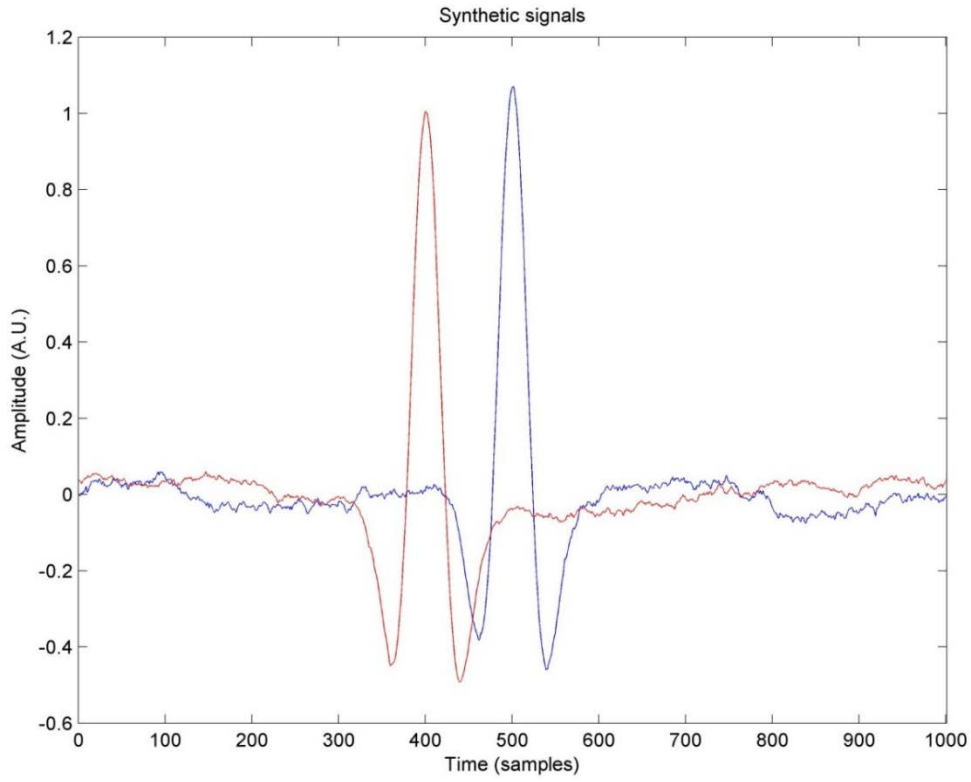

Figure 2.1. Synthetic signals obtained by summing Ricker wavelets with random red noise. The second Ricker wavelet (red) precedes the first one (blue) by 100 samples.

In **Fig 2.1** the synthetic signals mentioned above are shown. The synthetic signals are both made up of 1000 samples and the second Ricker wavelet precedes the first one by 100 samples (**Fig. 2.1**).

2.2.1 Cross Correlation (CC)

The time series, that have to be compared, were divided into windows of 400 samples, overlapped by 390 samples. Then, the cross-correlation analysis was performed. The cross-correlation function c quantifies the similarity between two signals and is defined as (Green and Neuberg, 2006):

$$c_{xy}(i, i-l) = \frac{\sum_{i=1}^{n}(x_i - \bar{x})(y_{i-l} - \bar{y})}{\sqrt{\sum_{i=1}^{n}(x_i - \bar{x})^2}\sqrt{\sum_{i=1}^{n}(y_i - y)^2}} \quad (2.1)$$

where x_i is the i-th sample of the signal x, y_{i-l} is the $(i-l)$-th sample of the signal y and the overbar represents the mean value of the signal. The index l is the lag between the two signals; changing this parameter varies the relative position of signal x with respect to signal y.

The cross-correlation analysis was performed on the windows, obtaining both the maximum cross correlation coefficient and the corresponding time lag. The maximum considered time lag was equal to 150 samples.

An example of application of this method on the two synthetic signals is shown in **Fig. 2.2**. It is evident how the described method allows to highlight the time intervals when the two signals are similar to each other, as well as the time lag between them.

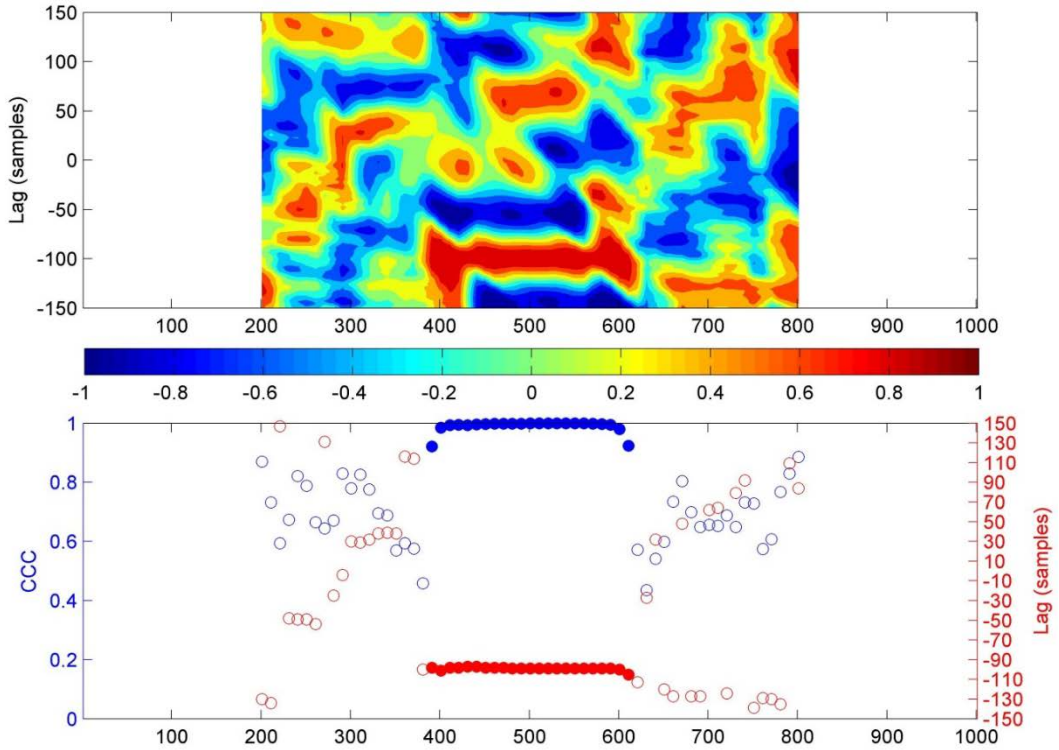

Figure 2.2. **(above)** Contour showing the time on the x-axis (in samples), the lag between the two signals in the y-axis and the cross-correlation coefficient with the color scale (see colorbar). **(below)** Cross correlation coefficient ("CCC", blue dots) and corresponding time lags (red dots) calculated for different consecutive signal windows (the empty dots represent values with cross correlation lower than 0.9).

2.2.2 Randomized Cross Correlation (RCC)

The second method was the Randomized Cross Correlation (RCC). It consisted of calculating the cross-correlation coefficient between time series considering maximum time lag of 150 samples. Moreover, in order to test the significance of the obtained cross correlation values, the analysis was repeated 1000 times, randomizing at each run the time of the second series (and then the order of its samples; Martini et al., 2009). In order to calculate mean and standard deviation of the randomized correlation, the Fisher's z transform was used to convert the correlation values into z, a new variable following a Gaussian distribution (e.g.: Saccorotti and Del Pezzo, 2000; Zuccarello et al., 2013):

$$z = \frac{1}{2} ln\left(\frac{1+c}{1-c}\right) \tag{2.2}$$

From z we can obtain unbiased estimation of both mean and standard deviation of c:

$$\acute{c} = \tanh(\bar{z}) \tag{2.3}$$

$$\sigma c = \tanh(\sigma z) \tag{2.4}$$

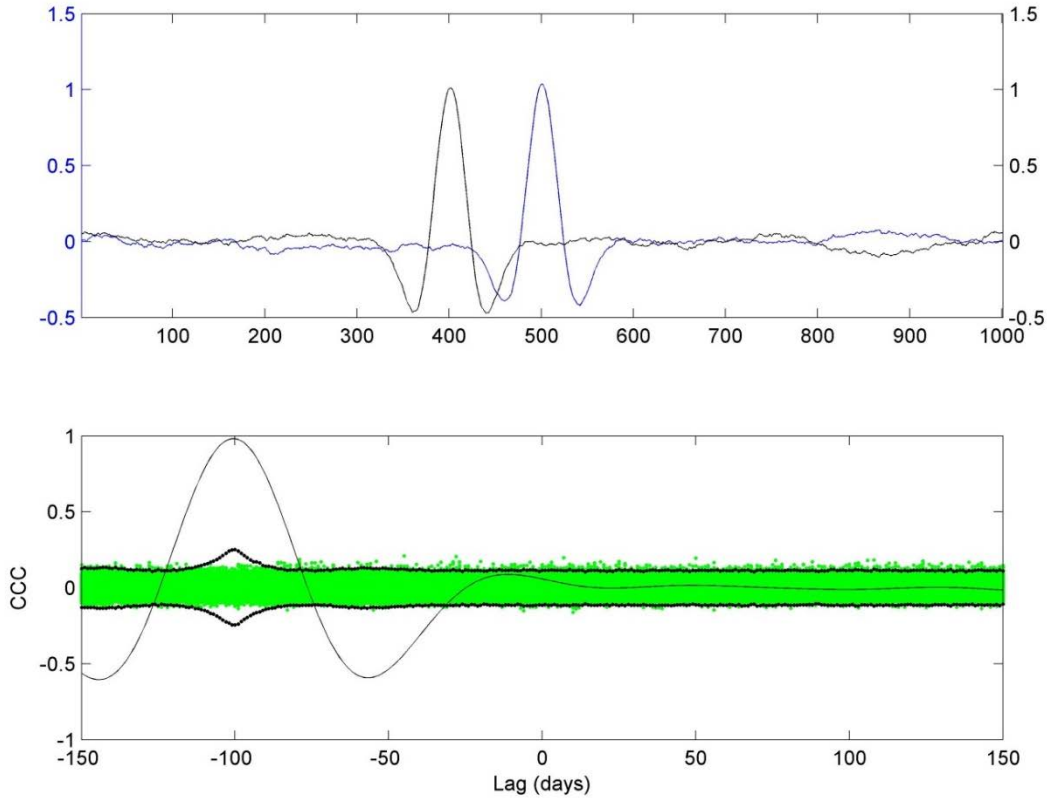

Figure 2.3. (above) Two synthetic signals. **(below)** Cross correlation function between the two signals shown above (black thin line), cross correlation values obtained by randomizing the sample order of the second signal (green dots), 99% (±3σ) confidence bounds on the distribution of the cross-correlation values (black dots).

An example of application of this method on the two synthetic signals is shown in **Fig. 2.3**. Unlike the previous method, this technique allows estimating the

significance of the obtained cross correlation values. In this case, it is noteworthy that the estimated cross correlation value is significant because it is much higher than the 99% ($\pm 3\sigma$) confidence bounds. Hence, also the time lag estimation (-100 samples) can be considered reliable.

2.2.3 Wavelet Coherence (WC) and Cross Wavelet Spectrum (CWS)

The third method is based on the wavelet transform that is used to analyze nonstationary time series (Foufoula-Georgiou and Kumar, 1995). The continuous wavelet transform (CWT) of time series is its convolution with the local basis functions, called mother wavelets, which can be stretched and translated with flexible resolution in both frequency and time (Jevrejeva et al., 2003). When using wavelets for feature extraction purposes the Morlet wavelet is a good choice, since it provides a good balance between time and frequency localization, as well as information about phase (Grinsted et al., 2004). For analysis of the covariance of two time series, two tools based on the wavelet transform can be used: cross-wavelet spectrum and wavelet coherence (hereafter referred to as CWS and WC, respectively). The former is a measure of the common power of two time series, while the latter evaluates the intensity of the covariance in time–frequency domain normalized in the range 0–1 (Jevrejeva et al., 2003). Given two time series x and y, with wavelet transform $W_n^X(s)$ and $W_n^Y(s)$ respectively, CWS is defined as (Torrence and Compo, 1998):

$$W_n^{XY}(s) = W_n^Y(s) W_n^{Y^*}(s) \tag{2.5}$$

where the $W_n^{Y^*}$ is the complex conjugate of $W_n^Y(s)$. The cross-wavelet spectrum is complex, hence a cross-wavelet power is defined as $|W_n^{XY}(s)|$. The WC is defined as (Grinsted et al., 2004):

$$R_n^2(s) = \frac{\left|S\left(s^{-1}W_n^{XY}(s)\right)\right|^2}{S\left(s^{-1}\left|\left(W_n^X(s)\right|^2\right)\right) \cdot S\left(s^{-1}\left|\left(W_n^X(s)\right|^2\right)\right)} \quad (2.6)$$

where S is a smoothing operator. Both the aforementioned techniques can also provide information on the phase relationship between time series, allowing estimating eventual lags between signals. The wavelet transform has edge artefacts because the wavelet is not completely localized in time. It is therefore useful to introduce a cone of influence (COI) in which edge effects cannot be ignored (Grinsted et al., 2004). Finally, also the noise affecting our data has to be considered. Commonly, power spectra of geophysical time series are characterized by increasing power at lower frequencies and show many distinctive red noise features. Following previous studies (e.g. Grinsted et al., 2004; Jevrejeva et al., 2003), 5% statistical significance level against red noise is considered in this study.

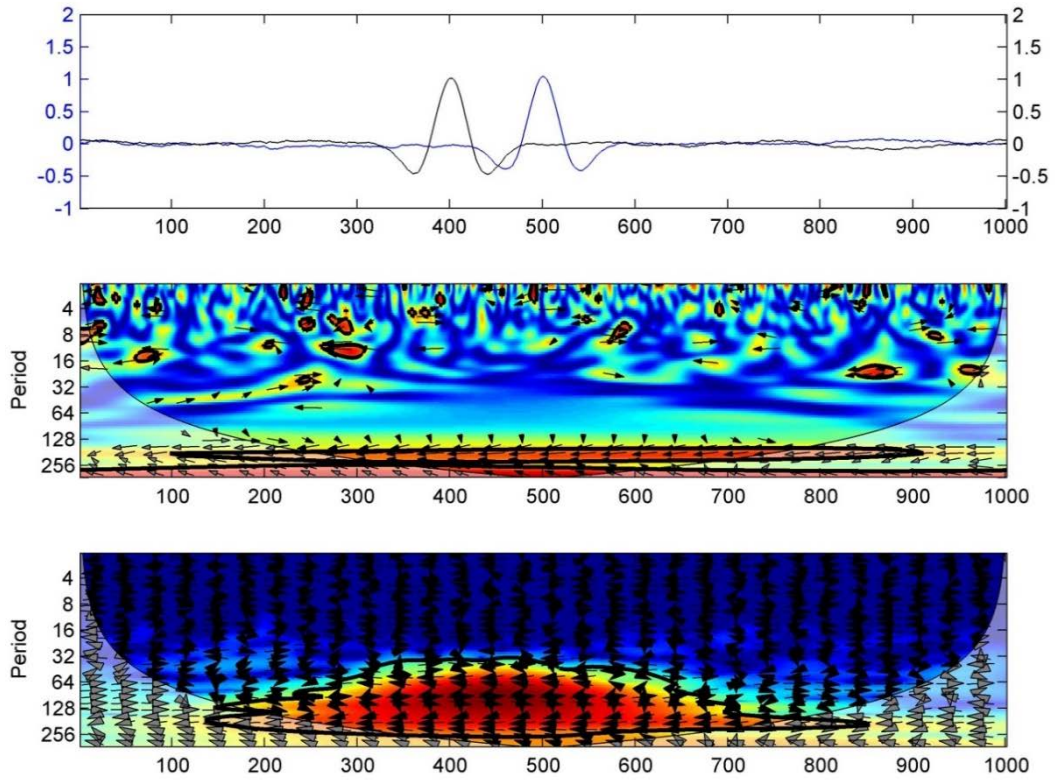

Figure 2.4. (above) Two synthetic signals, **(center)** wavelet coherence and **(bottom)** cross-wavelet spectrum. The 5% significance level against red noise is shown as a thick contour. The vectors indicate the phase difference between the synthetic signals (a horizontal arrow pointing from left

to right signifies in phase and an arrow pointing vertically upward means the first series lags the second one by 90°). The cone of influence (COI), where the edge effects might distort the picture, is shown as a lighter shade. The figures were drawn by the cross-wavelet and wavelet coherence software provided by A. Grinsted.

An application of this method on the two synthetic signals is shown in **Fig. 2.4**. WC and CWS permit pinpointing the time intervals when the compared signals are most similar, as well as to verify the significance of this similarity under the assumption of red noise. Moreover, since WC and CWS are defined in the time-frequency domain, they also allow estimating the periods (and then the frequency range) where the signals are most similar.

2.2.4 Linear regression and coefficient of determination (LR)

Similarly to the previous methods, the time series were divided into windows of 400 samples, overlapped by 390 samples. Then, the relationship between the windows was investigated by performing a linear regression and calculating the corresponding coefficient of determination (hereafter referred to as R^2). Similarly to the CC analysis, for each window we calculated both the maximum R^2 and the corresponding time lag. The maximum considered time lag was equal to 150 samples.

An application of this method on the two synthetic signals is shown in **Fig. 2.5**. Also, this method allowed to precisely estimate the time lag between the two synthetic signals. Furthermore, this technique permits to calculate a linear law (intercept and angular coefficient), that would connect the two considered parameters.

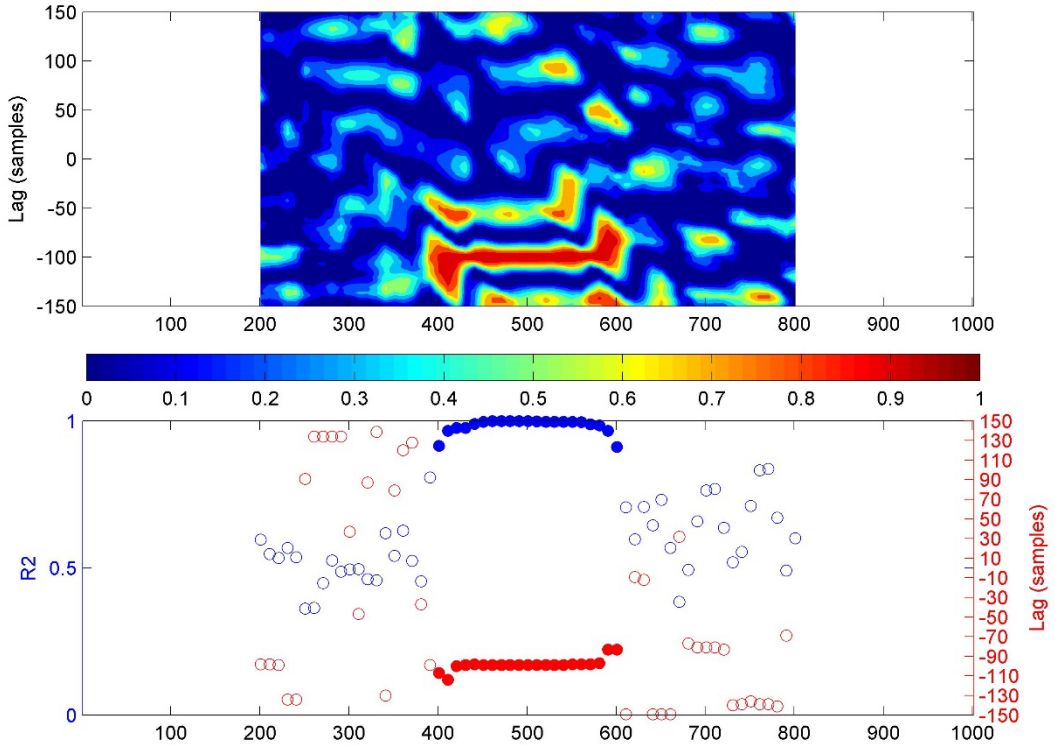

Figure 2.5. (above) Contour showing the time on the x-axis, the lag between the two signals in the y-axis and the R^2 with the color scale (see colorbar). **(below)** R^2 (blue dots) and corresponding time lags (red dots) calculated for different consecutive signal windows (the empty dots represent values with R^2 lower than 0.9).

2.3 DATA

To understand the volcano dynamics that characterized the Mt. Etna between 2011 and 2012, we referred to data from the multiparametric monitoring network managed by *Istituto Nazionale di Geofisica e Vulcanologia (INGV)*. Specifically, we made use of geophysical data such as volcanic tremor amplitude and geochemical data such as soil CO_2 flux and SO_2 flux from the summit craters. To investigate any similarity, to identify the most significant changes of trends, to detect synchronous variations of trend between different data and to estimate the possible time lag between the available time series, we took into consideration geophysical and geochemical data related to the time interval from 1 January 2010 to 31 December 2012.

2.3.1 Geophysical data

2.3.1.1 Seismic data

At Mount Etna, the seismic permanent network run by Istituto Nazionale di Geofisica e Vulcanologia (INGV) – Osservatorio Etneo comprises 33 broadband and 12 short-period stations. For this work, the analyses of seismo-volcanic signals were performed on the recordings of EBEL, the station closest to the NSEC. This station was equipped with broadband, 3-component Trillium seismometers (Nanometrics™) acquiring in real-time at a sampling rate of 100 Hz (**Fig 2.6**).

As already explained in paragraph 2.1, the seismic signal recorded in the 2010-2012 period was taken into account. Following Cannata et al. (2015), to investigate volcanic tremor temporal variations, the time evolution of the RMS amplitude of the seismic signal recorded by the vertical component of EBEL station, calculated on 10 s-long moving windows filtered in the band 0.5 - 2.5 Hz, was considered **(Fig. 2.7**).

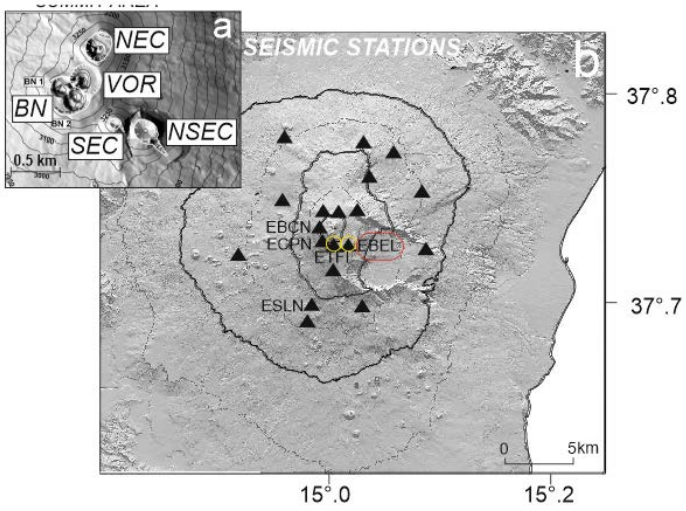

Figure 2.0.6. Digital Elevation Model (DEM) of the summit area of Mt. Etna with the main craters (Bocca Nuova: BN; Voragine: VOR; Cratere di Nord-Est: NEC; Cratere di Sud-Est: SEC; Nuovo Cratere di Sud-Est: NSEC) (**a**) and DEM of Mt. Etna with seismic stations (**b**)

Successively, the 25-th percentile on 8 hour-long moving windows of RMS was calculated to exclude the contributions of transient amplitudes and highlight the variations related to volcanic tremor changes. The most important RMS peaks, coinciding with the lava fountains, were observed during January–April 2011 (Phase I), July-November 2011 (Phase II) and January-March 2012 (Phase III) periods.

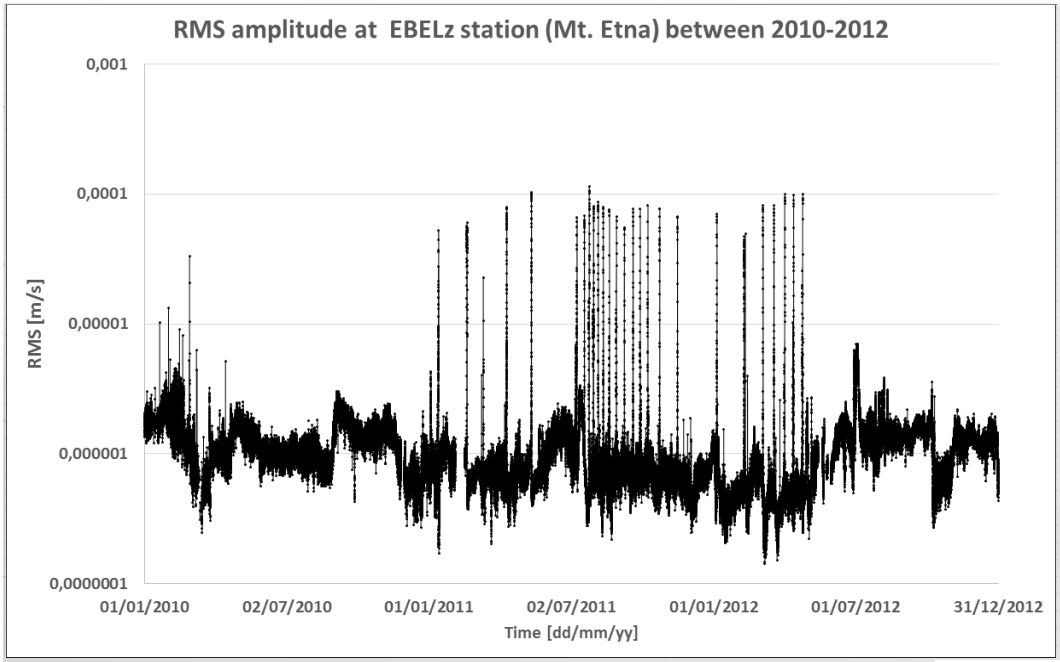

Figure 2.7. RMS amplitude of seismic signals recorded at vertical component of EBEL station during the years between 2010 - 2012 and filtered in the band 0.5-2.5 Hz.

2.3.2 Geochemical data

2.3.2.1 Soil CO_2 flux

The soil CO_2 flux data were acquired by geochemical network named EtnaGas CO_2 soil flux network, which comprises 15 automatic stations (**Fig. 2.8**).

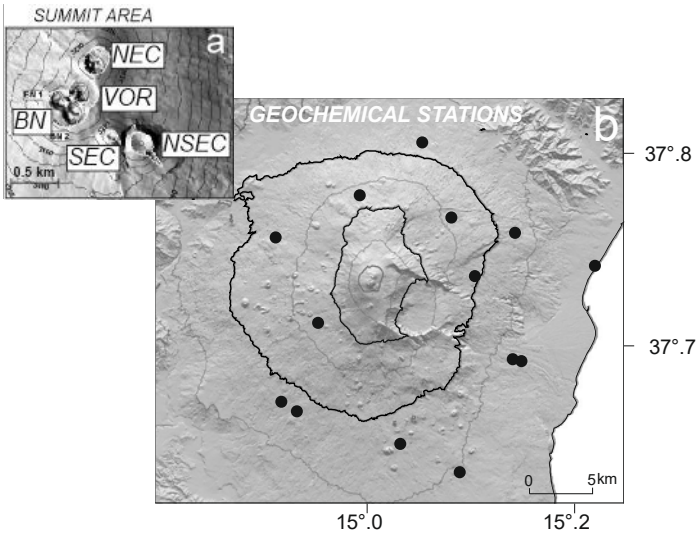

Figure 2.8. DEM of the summit area of Mt. Etna with the main craters (Bocca Nuova: BN; Voragine: VOR; Cratere di Nord-Est: NEC; Cratere di Sud-Est: SEC; Nuovo Cratere di Sud-Est: NSEC) (**a**) and DEM of Mt. Etna with geochemical stations measuring soil CO_2 flux (**b**)

The monitoring stations of the network were entirely developed by INGV Palermo and are able to monitor some parameters such as CO_2 and CH_4 soil fluxes, pressure, atmospheric temperature, humidity, rain, wind speed and wind direction. Generally, soil CO_2 flux measurements are carried out by the dynamic method (Gurrieri and Valenza, 1988; Gurrieri et al., 2008, and reference therein). Successively, a unified value of soil CO_2 flux is obtained following the method proposed in Liuzzo et al. (2013). With this method, three steps are considered: first, each time series from all the stations is filtered for the meteorological parameters and/or seasonal variations; second, in order to compare the amplitude of the soil CO_2 flux variation from different stations, each soil CO_2 flux series is normalized within the range of 0–1; and finally, all the time series from each station are added together and the final sum is normalized again within the interval 0–1.

The **Fig. 2.9** shows Φ_{Norm} representing the total soil CO_2 flux amplitude variations during 2010-2012 period. High values of Φ_{Norm} suggest a high degassing state on Mt. Etna.

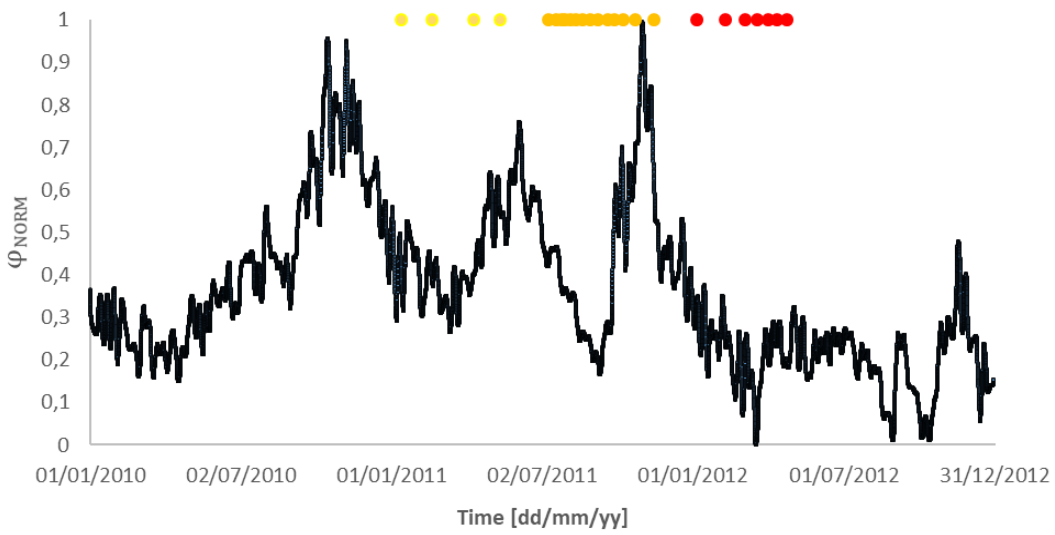

Figure 2.9. Daily soil CO_2 flux measurements by EtnaGas geochemical network of Mt. Etna from January 2010 to December 2012. Yellow, orange and red dots represent lava fountaining during Phase I, Phase II and Phase III, respectively.

2.3.2.2 SO_2 flux at summit craters

At Mt. Etna, the SO_2 flux data from summit craters were acquired with the geochemical network FLAME-Etna (Automatic Flux MEasurements, Salerno et al, 2009; Campion et al., 2010). The FLAME-Etna consists of nine autonomous ultraviolet scanning spectrometer stations (**Fig. 2.10**) installed at an altitude of ~900 m a.s.l. on the flanks of volcano edifice and spaced about 7 km apart (Salerno et al., 2009; Campion et al., 2010; Patane et al., 2013). Each station was equipped with Ocean Optics S2000 spectrometer connected via fiber optic cables to a telescope mounted in a rotating head. Each device operates independently from weather conditions scanning the sky for about 9 h (during daylight), so as to intersect the plume at a mean distance of about 14 km from the summit craters area, acquiring a complete scan in about 5 min.

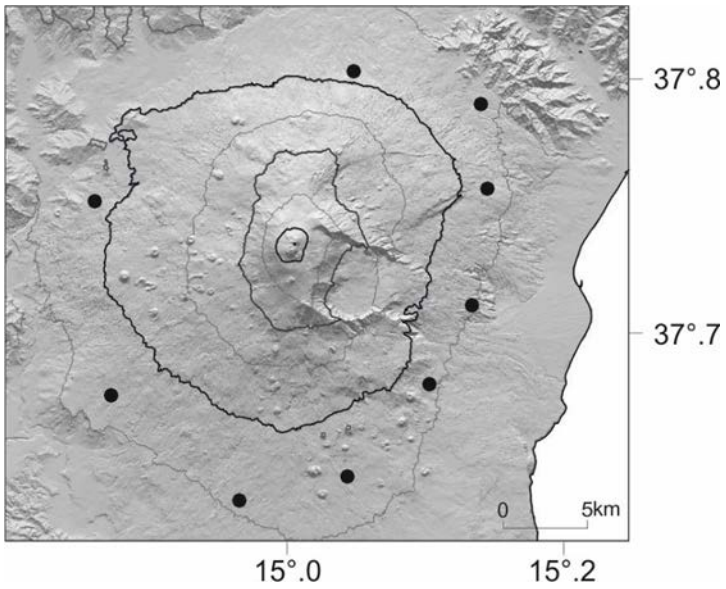

Figure 2.10. DEM of Mt. Etna with the geochemical stations belonging to the FLAME network

The light exposure of the detector is automatically adjusted throughout the day to optimize the signal. SO_2 column amounts are retrieved in real time on site from the recorded ultraviolet open path spectra applying the Differential Optical Absorption Spectroscopy (DOAS) technique but using a modeled clear-sky spectrum rather than a measured spectrum as in the classic DOAS technique.

Fig. 2.11 shows the daily SO_2 flux measurements from the bulk volcanic plume of Mt. Etna between January 2010 and December 2012.

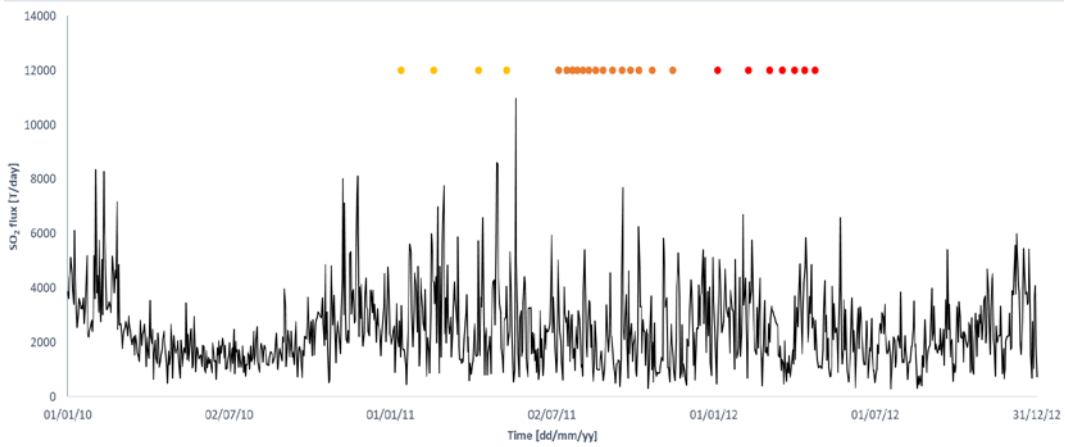

Figure 2.11. Daily SO_2 flux measurements from the bulk volcanic plume of Mt. Etna from January 2010 to December 2012. Yellow, orange and red dots represent lava fountaining during Phase I, Phase II and Phase III, respectively.

During this period, the emission rate was characterized by a mean value of 2500 $Mg \cdot d^{-1}$, ranging from a minimum value of 300 Mg d^{-1} (19 July 2012) to a maximum of 11000 $Mg \cdot d^{-1}$ (22 May 2011). The diagram shows that SO_2 emission rates rose significantly from late September 2010 to late May 2011, then underwent a slight decrease from late May 2011 until the end of 2012. However, despite the reduction, the emission values remained higher than those before the end of September 2010.

2.4 DATA ANALYSIS

Before carrying out the multiparametric quantitative comparison of time series with the methods described in paragraph 2.2, it was necessary to define a single sampling rate for the time series to be used. Therefore, having decided to use a daily sampling rate, it was necessary to resample only the time series of the RMS amplitude of volcanic tremor. Moreover, in order to avoid that peaks of volcanic tremor during lava fountaining episodes could influence the analyses, a "despiking" of the relative time series was performed.
Subsequently, quantitative comparison between time series has been carried out considering a maximum shift of 100 days (therefore corresponding to 100 samples) of the geochemical time series with the volcanic tremor RMS amplitude. The results obtained will be shown below.

2.4.1 RMS amplitude of seismic signals vs soil CO_2 flux

The quantitative comparison between the time series of the volcanic tremor RMS amplitude recorded at vertical component of EBEL seismic station and the soil CO_2 flux recorded at Mt. Etna during 2010-2012 was carried out by all the techniques discussed in Section 2.2.

- **Cross-Correlation analysis**

Fig. 2.12 shows the results obtained from the Cross-Correlation (CC) analysis; the results are considered significant for values of the cross-correlation coefficient (CCC) such that CCC ≥ 0.6. First of all, it emerges that there are no synchronous variations of trends between the compared series. However, during the considered period of 3 years, the analysis not highlighted significative similarities

by shifting the geochemical series both forward and backward: in fact, despite for Phase 1 and Phase 2 were found negative values of time lag with high values of CCC (more than 0.6) that would indicate as the seismic series lags the soil CO_2 flux series, in general many values of positive time lag were also found for the three years considered, especially for Phase 3.

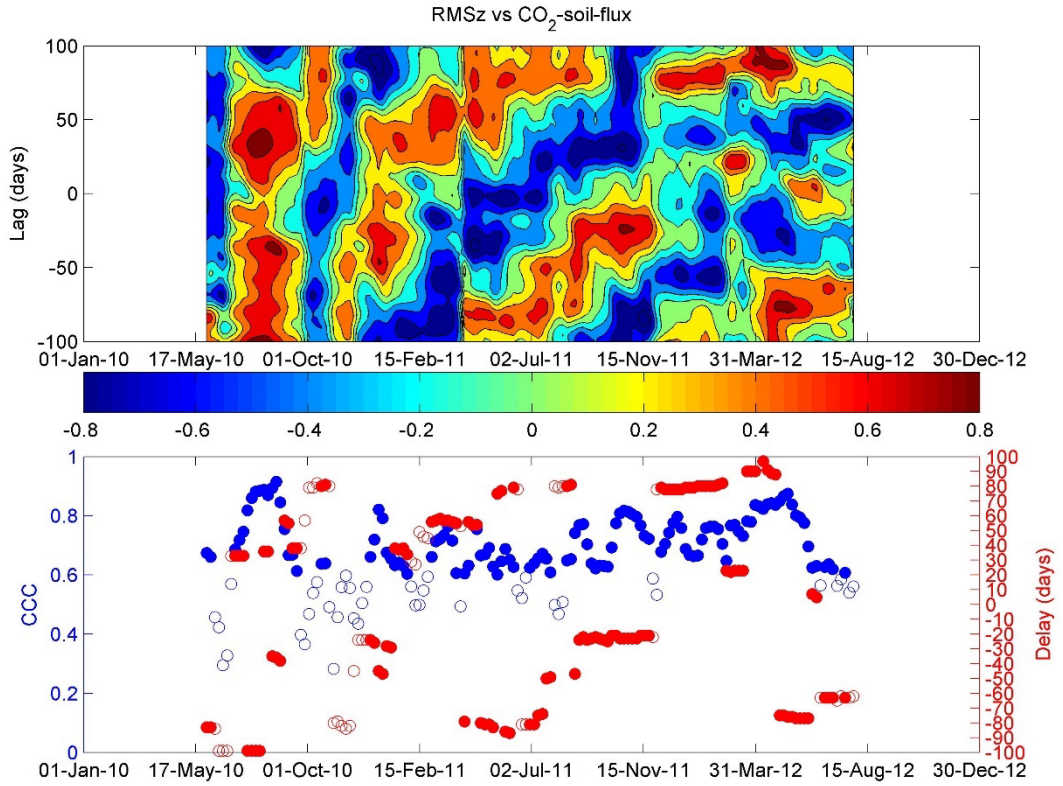

Figure 2.12. Cross correlation analysis between RMS amplitude at vertical component of EBEL station and soil CO_2 flux recorded at Mt. Etna from January 2010 to December 2012. **(above)** Contour showing the time on the x-axis (in samples), the lag between the two signals in the y-axis and the cross-correlation coefficient with the color scale (see colorbar). **(below)** Cross correlation coefficient ("CCC", blue dots) and corresponding time lags (red dots) calculated for different consecutive signal windows (the empty dots represent values with cross correlation lower than 0.6).

- **Randomized Cross Correlation**

Fig. 2.13 shows the results obtained from the Randomized Cross-Correlation (RCC) analysis. Initially it was calculated the coefficient of Cross-Correlation between the

two time series considering a maximum time lag of ± 100 samples. Subsequently, the analysis was iteratively repeated 1000 times, randomizing each time the order of the samples of the time series of the soil CO_2 flux, while the time series of the volcanic tremor remained unchanged. Shifting the geochemical series in a range between ± 100 samples, it emerges that thereare no synchronous variations of the trends between the compared series. Moreover, the analysis highlighted that, only by shifting forward the geochemical series of 35, 36 and 78 samples, it is possible to obtain the maximum values of reliable cross correlation, while for the other time lag the values tend to fall within the range of Cross-Correlation values obtained with randomization and considering a 99% confidence interval (3σ).

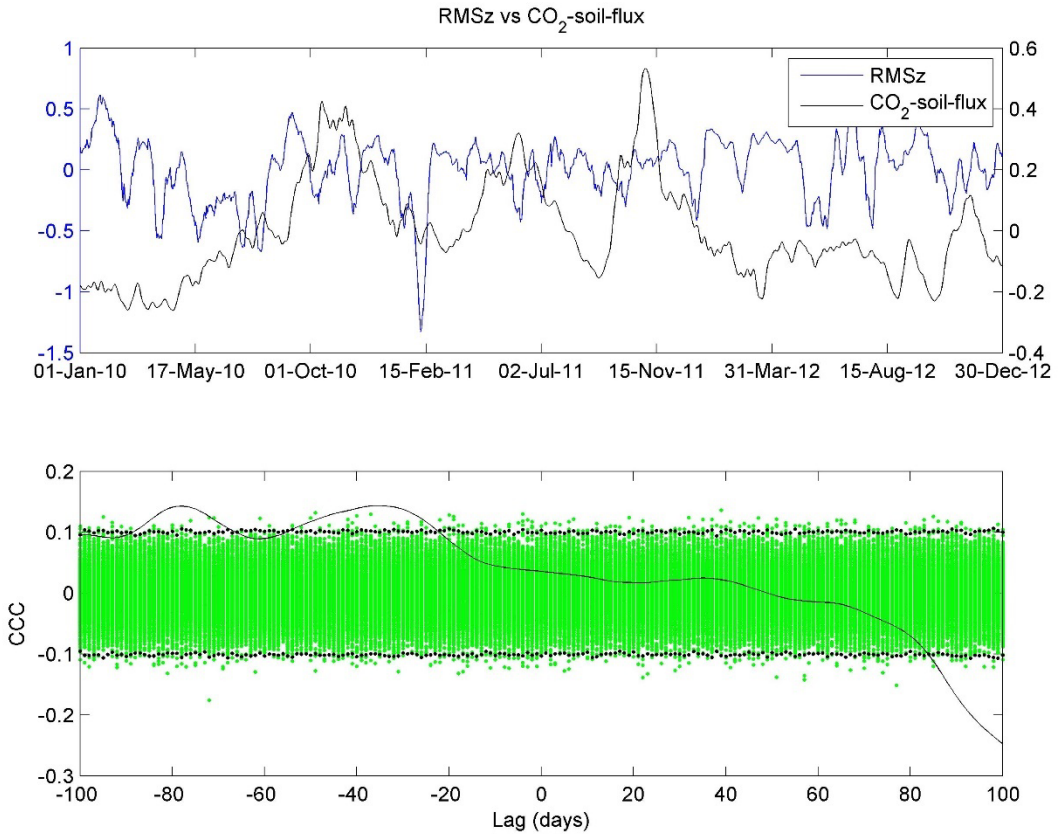

Figure 2.13. (above) Time series: RMS amplitude at vertical component of EBEL station (blue line) vs. soil CO_2 flux (black line) recorded at Mt. Etna from January 2010 to December 2012. **(below)** Cross correlation function between the two signals shown above (black thin line), cross correlation values obtained by randomizing the sample order of soil CO_2 flux time series (green dots), 99% (±3σ) confidence bounds on the distribution of the cross-correlation values (black dots).

- **Wavelet Coherence (WC) and Cross Wavelet Spectrum (CWS) analysis**

Fig. 2.14 shows the results obtained from Wavelet Coherence (WC) and Cross Wavelet Spectrum (CWS) analysis and the comparison between the geophysical and geochemical time series.

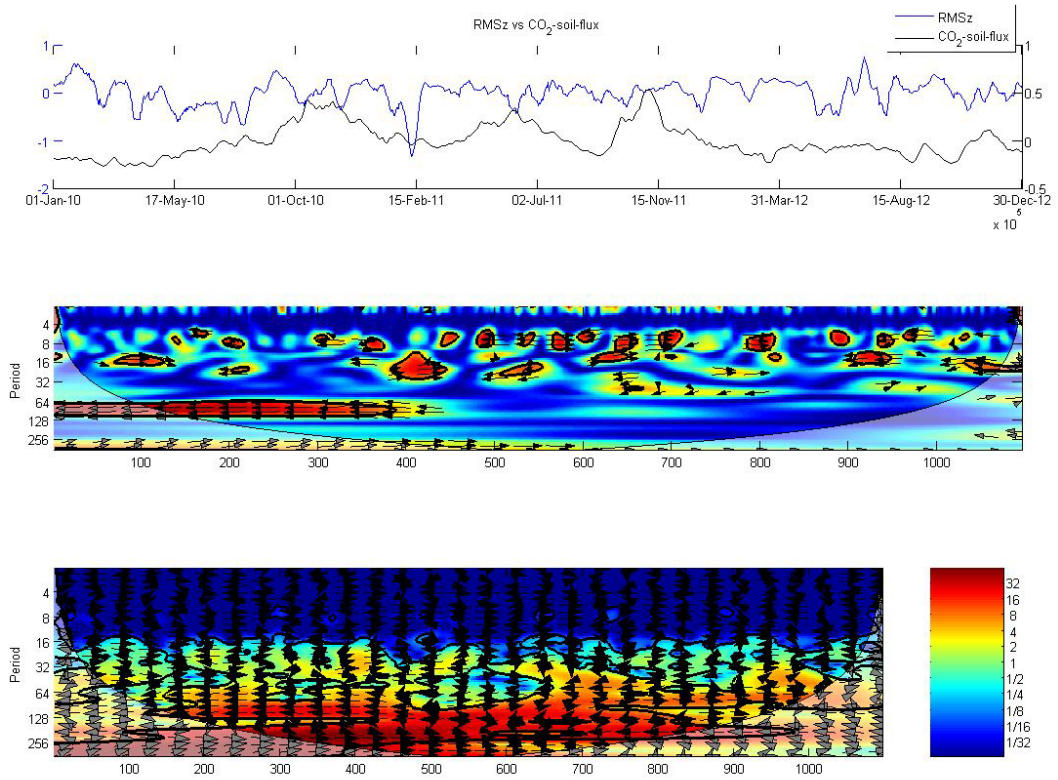

Figure 2.14. (above) Time series compared: RMS amplitude at vertical component of EBEL station (blue line) vs. soil CO_2 flux (black line) recorded at Mt. Etna from January 2010 to December 2012, **(center)** wavelet coherence and **(bottom)** cross-wavelet spectrum. The 5% significance level against red noise is shown as a thick contour. The vectors indicate the phase difference between the time series (a horizontal arrow pointing from left to right signifies in phase and an arrow pointing vertically upward means the first series lags the second one by 90°). The cone of influence (COI), where the edge effects might distort the picture, is shown as a lighter shade.

The plots in **Fig 2.15** show in detail the analysis results. Considering the 5% significance level against red noise (shown as a thick contour) and the regions outside from the cone of influence (COI) where the edge effects might distort the picture (shown as a lighter shade), the analyses have highlighted only the 2010

interval, characterized by high values of both wavelet coherence and cross wavelet spectrum at period 64-128 days and phase opposition.

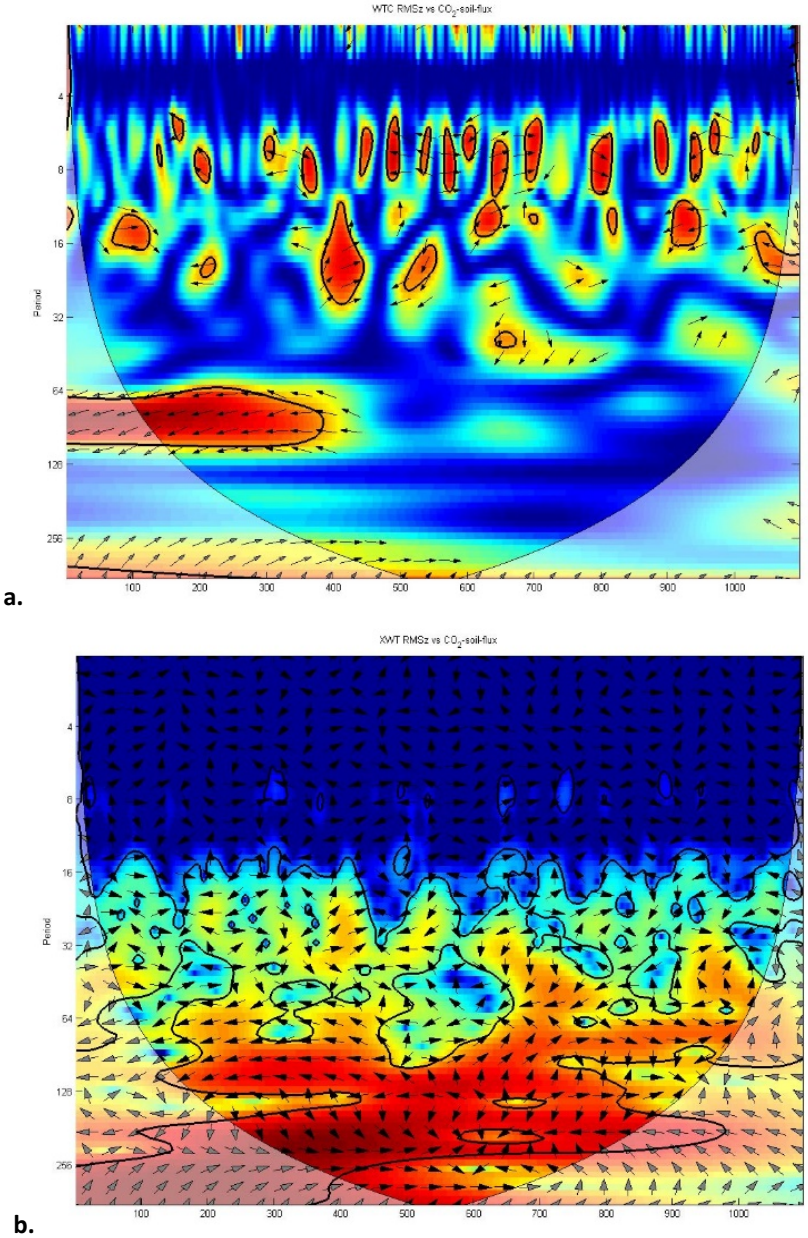

Figure 2.15. Plots in details of **(a)** wavelet coherence analysis and (**b**) cross-wavelet spectrum analysis. The 5% significance level against red noise is shown as a thick contour. The vectors indicate the phase difference between the time series (a horizontal arrow pointing from left to right signifies in phase and an arrow pointing vertically upward means the first series lags the second one by 90°). The cone of influence (COI), where the edge effects might distort the picture, is shown as a lighter shade.

- **Linear regression and coefficient of determination (LR) analysis**

Fig. 2.16 shows the results obtained from Linear Regression (LR) analysis. In this case, unlike the previous ones, the analysis did not highlight any trend or produce significant relationship between the time series: in fact, the comparison between the three-years-long time series returned low values of R^2 for the considered time lag of ± 100 samples.

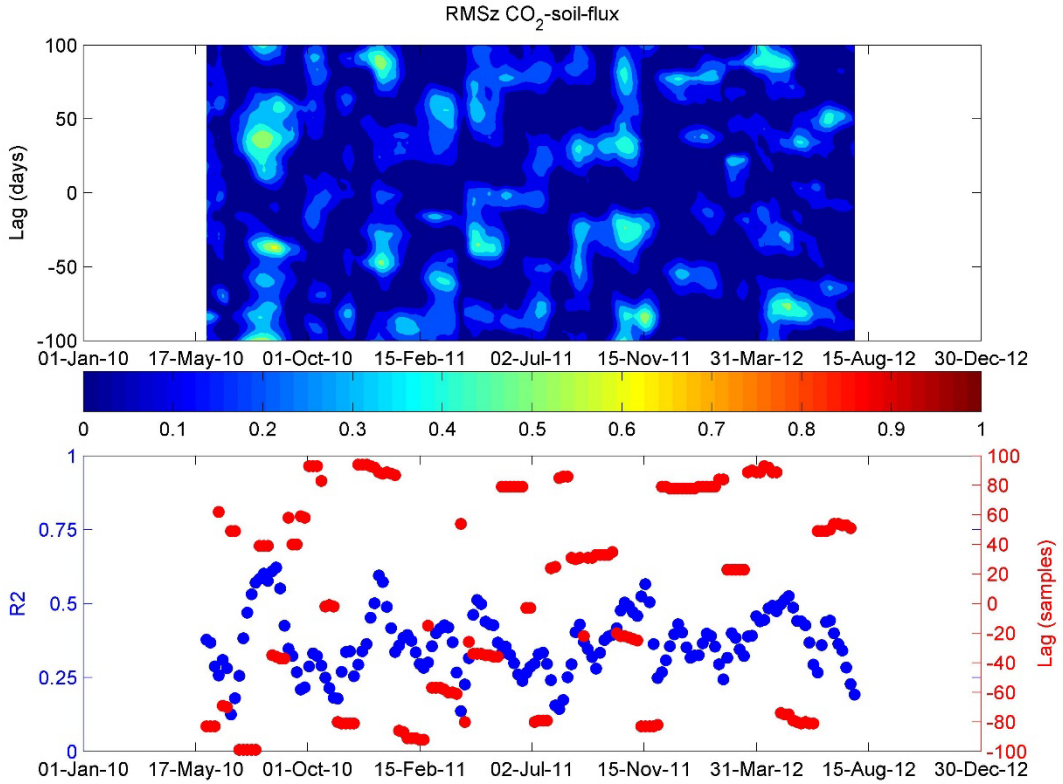

Figure 2.16. (above) Contour showing the time on the x-axis, the lag between the two temporal series in the y-axis and the R^2 with the color scale (see colorbar). **(below)** R^2 (blue dots) and corresponding time lags (red dots) calculated for different consecutive signal windows (the full dots represent values with R^2 lower than 0.9).

2.4.2 RMS amplitude of seismic signals vs SO_2 flux at summit craters

As for the comparison described in paragraph 2.4.2, the quantitative comparison between the time series of the RMS amplitude of volcanic tremor recorded at

vertical component of EBEL seismic station and the SO_2 flux at summit craters recorded at Mt. Etna during 2010-2012 was carried out by all the techniques discussed in section 2.2.

- **Cross-Correlation analysis**

Fig. 2.17 shows the results obtained from the Cross-Correlation (CC) analysis between RMS amplitude of volcanic tremor recorded at the vertical component of EBEL station and the SO_2 flux al summit craters recorded by FLAME geochemical network.

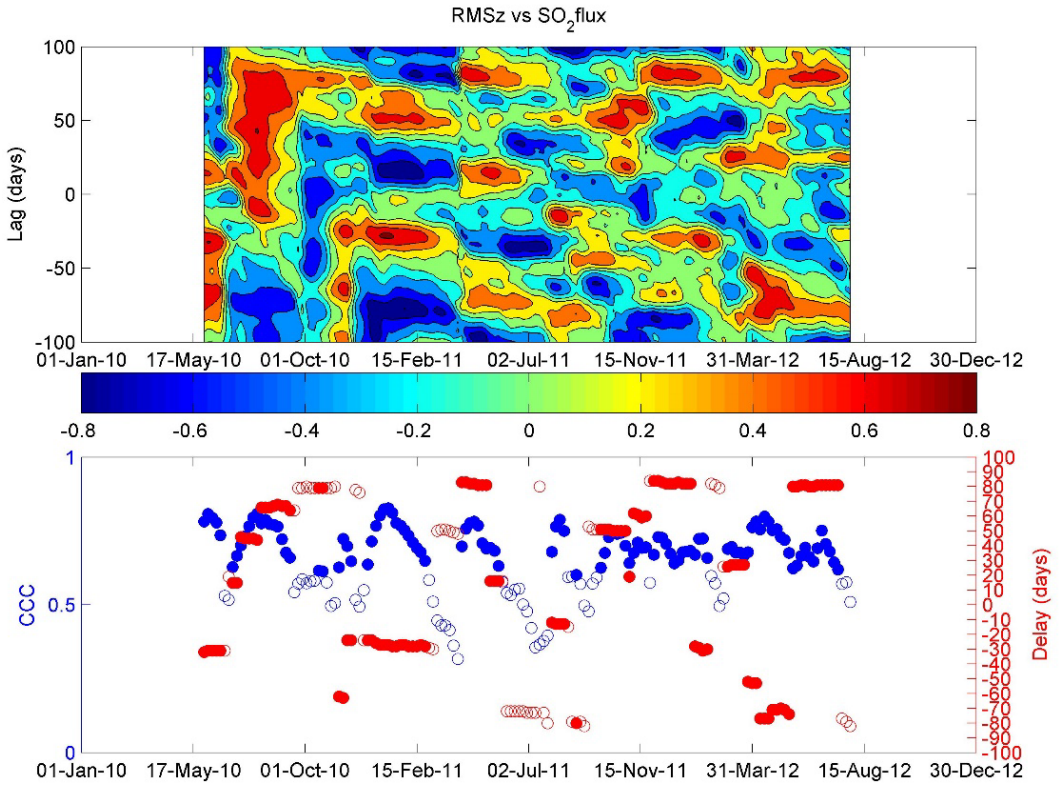

Figure 2.17. Cross correlation analysis between RMS amplitude at vertical component of EBEL station and SO_2 flux at summit craters recorded at Mt. Etna from January 2010 to December 2012. **(above)** Contour showing the time on the x-axis (in samples), the lag between the two time series in the y-axis and the cross-correlation coefficient with the color scale (see colorbar). **(below)** Cross correlation coefficient ("CCC", blue dots) and corresponding time lags (red dots) calculated for different consecutive signal windows (the empty dots represent values with cross correlation lower than 0.6).

The results are considered significant for values of the cross-correlation coefficient (CCC) such that CCC ≥ 0.6. Shifting the geochemical series in a range between ±100 samples, it emerges that there would be no synchronous variations of trends between the series compared.

As seen in Section 2.4.1 for the comparison of RMS amplitude vs soil CO_2 flux, during the considered 3 years period, also for the SO_2 flux at summit craters the analysis not highlighted significative similarities by shifting the geochemical series both forward and backward: in fact, for high values of CCC (more than 0.6), an high variability of positive and negative time lag was found without any particular trends being detected.

- **Randomized Cross Correlation**

Fig. 2.18 shows the results obtained from the Randomized Cross-Correlation (RCC) analysis. Initially it was calculated the cross-correlation coefficient between the two time series considering a maximum time lag of ± 100 samples. Subsequently, the analysis was iteratively repeated 1000 times, randomizing each time the order of the samples of the time series of the SO_2 flux at summit craters, while the time series of the volcanic tremor remained unchanged. Shifting the geochemical series in a range between ± 100 samples, it emerges that there are no synchronous variations of the trends between the series compared. Moreover, the analysis highlighted that only by shifting backward the geochemical series of a number of samples between 51 and 74 it is possible to obtain the maximum values of reliable cross correlation, while for the other time lag most of the values tend to fall within the range of cross-correlation values obtained with randomization and considering a 99% confidence interval (3σ).

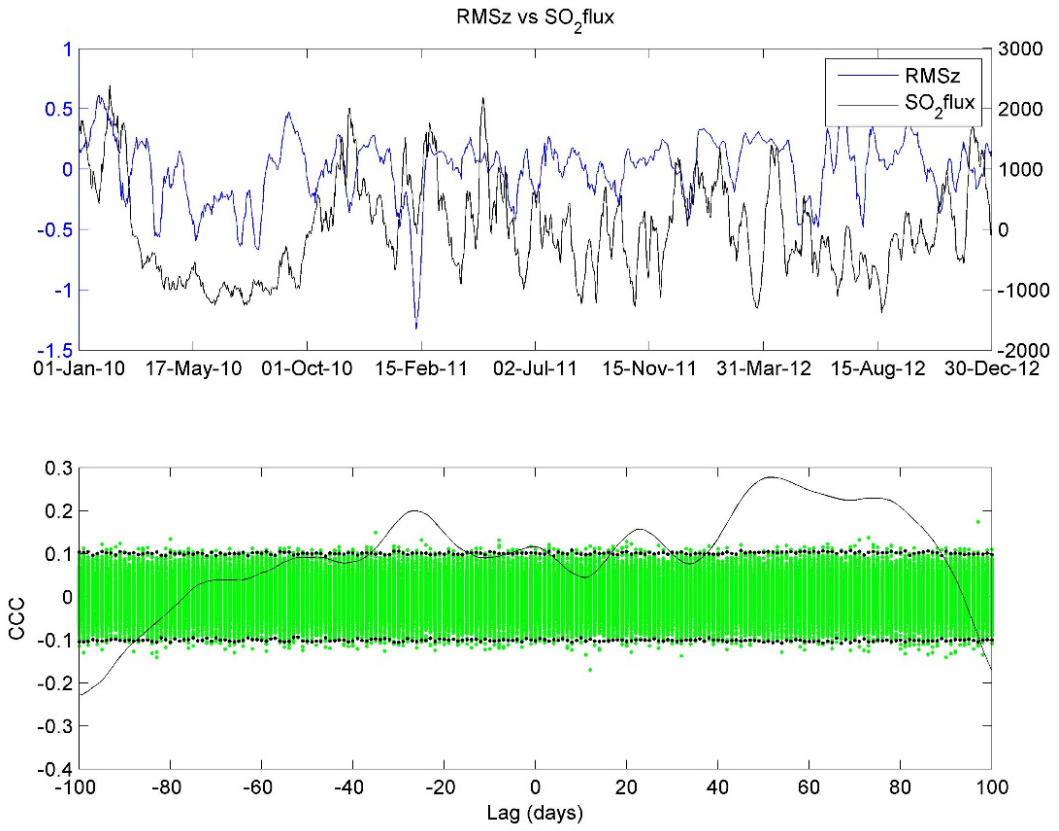

Figure 2.18. (above) Time series compared: RMS amplitude at vertical component of EBEL station (blue line) vs. SO_2 soil flux (black line) recorded at Mt. Etna from January 2010 to December 2012. **(below)** Cross correlation function between the two signals shown above (black thin line), cross correlation values obtained by randomizing the sample order of SO_2 flux time series (green dots), 99% (±3σ) confidence bounds on the distribution of the cross-correlation values (black dots).

- **Wavelet Coherence (WC) and Cross Wavelet Spectrum (CWS) analysis**

Fig. 2.19 shows the results obtained from Wavelet Coherence (WC) and Cross Wavelet Spectrum (CWS) analysis and the comparison between the geophysical and geochemical time series.

The plots in **Fig. 2.20** show in detail the results of the analyses. Considering the 5% significance level against red noise (shown as a thick contour) and the regions outside from the cone of influence (COI) where the edge effects might distort the picture (shown as a lighter shade), the analyses have not highlighted any common periods where high values of wavelet coherence and cross wavelet spectrum are

found. Therefore, as found in the comparison between the RMS amplitude of the tremor and soil CO_2 flux, it was not possible to reliably evaluate any time lag between the series considering the evaluation of the phase angle of cross wavelet spectrum.

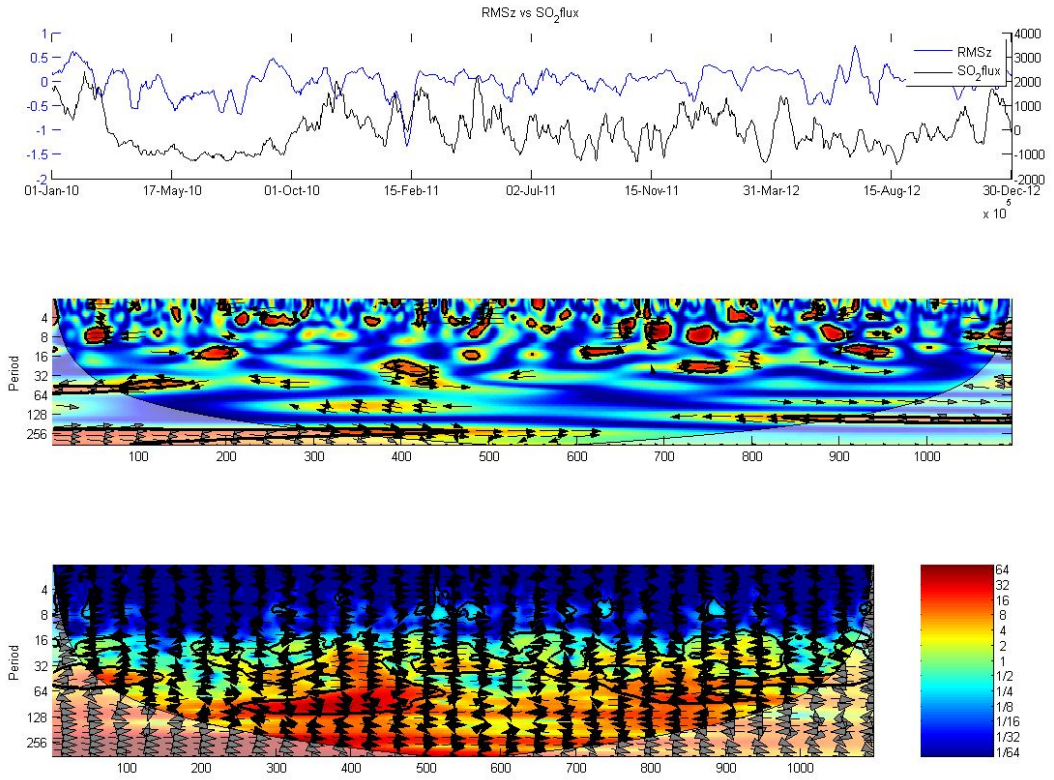

Figure 2.19. (above) Time series compared: RMS amplitude at vertical component of EBEL station (blue line) vs. SO_2 flux at summit craters (black line) recorded at Mt. Etna from January 2010 to December 2012, **(center)** wavelet coherence and **(bottom)** cross-wavelet spectrum. The 5% significance level against red noise is shown as a thick contour. The vectors indicate the phase difference between the time series (a horizontal arrow pointing from left to right signifies in phase and an arrow pointing vertically upward means the first series lags the second one by 90°). The cone of influence (COI), where the edge effects might distort the picture, is shown as a lighter shade.

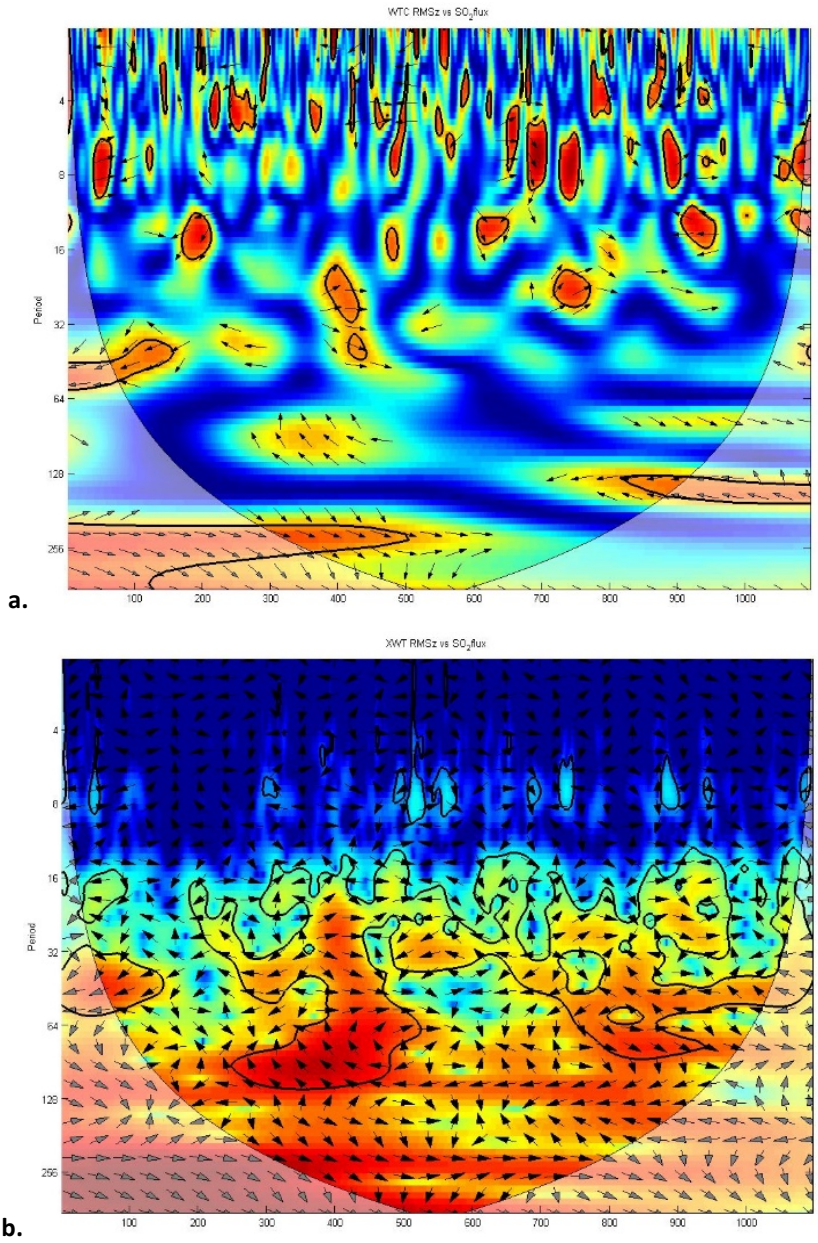

Figure 2.20. Plots in details of **(a)** wavelet coherence analysis and (**b**) cross-wavelet spectrum analysis. The 5% significance level against red noise is shown as a thick contour. The vectors indicate the phase difference between the time series (a horizontal arrow pointing from left to right signifies in phase and an arrow pointing vertically upward means the first series lags the second one by 90°). The cone of influence (COI), where the edge effects might distort the picture, is shown as a lighter shade.

- **Linear regression and coefficient of determination (LR) analysis**

Fig. 2.21 shows the results obtained from Linear Regression (LR) analysis. Similarly to the comparison of RMS amplitude vs soil CO_2 flux, the analysis did not highlight significant relationship between volcanic tremor amplitude and SO_2 flux.

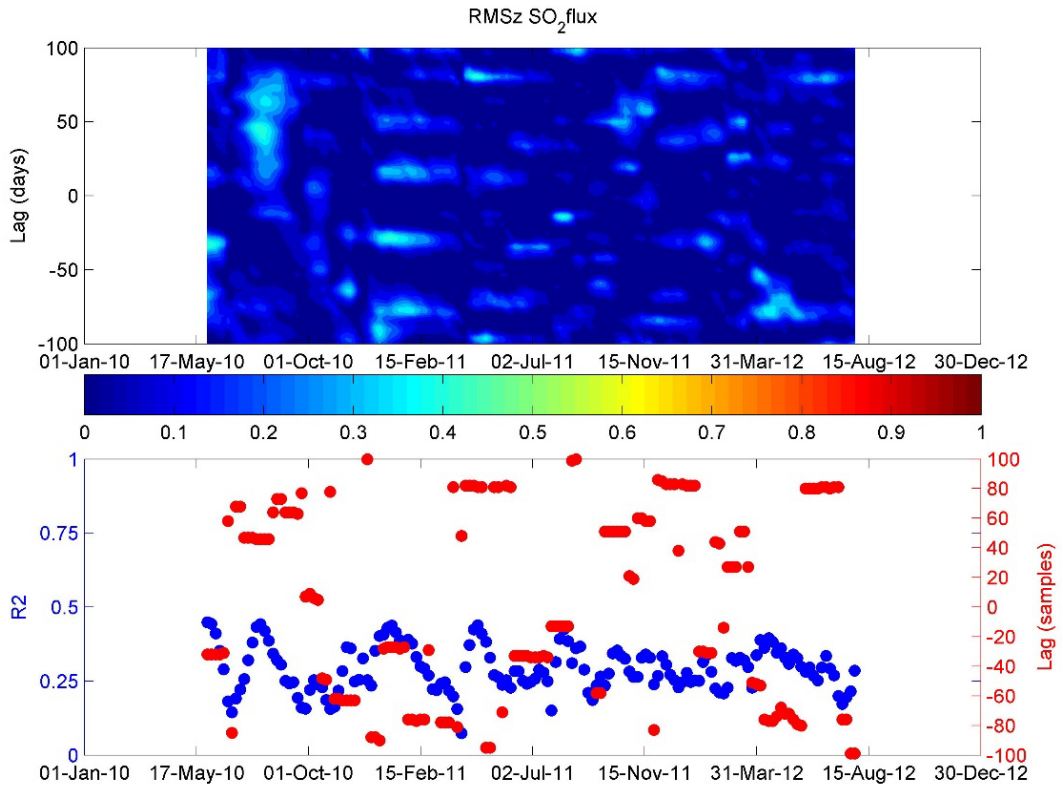

Figure 2.21. (above) Contour showing the time on the x-axis, the lag between the two temporal series in the y-axis and the R^2 with the color scale (see colorbar). **(below)** R^2 (blue dots) and corresponding time lags (red dots) calculated for different consecutive signal windows (the full dots represent values with R^2 lower than 0.9).

2.5 DISCUSSION AND CONCLUSIONS

The multiparametric approach in the analysis of the data acquired through volcanic monitoring is very important for the interpretation of the state of a volcano.

What is illustrated in this chapter consists of a multiparametric study of the volcano activity using quantitative methods of comparison. For this study, the Mount Etna volcano was taken into consideration for two fundamental reasons: (i) for the continuous and persistent activity whose dynamics often develop relatively quickly and (ii) for the continuous monitoring activity through instrumentation networks able to acquire different geophysical (such as seismic and infrasonic signals, ground deformations, gravimetric variations), geochemical (gas fluxes emissions) and volcanological data.

The attention of this study was focused on the activity at Mt. Etna that occurred between January 2011 and December 2012, when 25 episodes of lava fountain took place from the New South Eastern Crater (NSEC, pit-crater at the beginning of 2011). Initially, several time series of distinct data recorded during the period were taken into account: RMS amplitude of the seismic signal recorded at the vertical component of the EBEL station (that can be considered as RMS amplitude of the volcanic tremor), variations of the length of the baseline between EMSG-EMGL stations, degassing activities with soil CO_2 flux, SO_2 flux at summit craters and CO_2/ SO_2 ratio at summit craters. However, due to the lack of continuity in data acquisition during the considered period, for this study it was decided to exclude the time series of ground deformation and gas flux ratio at summit craters, and to proceed for quantitative comparison between the RMS amplitude of the volcanic tremor and time series of soil CO_2 flux and SO_2 flux at summit craters.

In order to perform the multiparametric quantitative comparison, four different methods of analysis were used: (i) Cross-Correlation, (ii) Randomized Cross-Correlation, (iii) Wavelet Coherence and Cross Wavelet Spectrum and (iv) Linear Regression analysis. At Mt. Etna, these analyses were used in the past to study different periods of the activity; for example, by Cross-Correlation analysis and

Wavelet Coherence - Cross Wavelet Spectrum, Cannata et al. (2010a) highlighted how it was possible to correlate the overall spectral amplitude (OSA) of the vertical component of EBEL station during the eruptive activity between September 2004 and March 2005 with the soil CO_2 flux detected about 50 days before. Using Randomized Cross-Correlation analysis, instead, Zuccarello et al. (2013) highlighted how it was possible to correlate the SO_2 flux at summit craters and cumulative volume changes due to VLP events during quiescent phase of activity at Mt. Etna between 01 October 2005 and 31 January 2006; they obtained zero-lag correlation, indicating the simultaneous coupling between the two processes.
For the quantitative analysis made with this thesis, geophysical and geochemical time series were compared with daily sampling rate during the period 01 January 2010 - 31 December 2012 and considering time lag max ±100 days. The results obtained and illustrated in Section 2.4 are:

- Cross-Correlation, Wavelet Coherence, Cross Wavelet Spectrum and Linear Regression analysis have not highlighted any clear correlation;
- Randomized Cross-Correlation analysis seems to show some significant correlations during some phases of the 2011-2012 activity.

Randomized Cross-Correlation analysis between volcanic tremor RMS amplitude and soil CO_2 flux showed that the first series lags the second one by 35 to 78 days with a highest peak equal to 0.143. Although the cross-correlation coefficient values are not high, they were considered indicative, because both they are greater than the 99% confidence interval, and because they are obtained considering a rather long period of volcanic activity characterized by high dynamism.
Focusing on Randomized Cross-Correlation analysis between volcanic tremor RMS amplitude of volcanic tremor at vertical component of EBEL station and SO_2 flux for 2010-2012 period, also in this case significant results were obtained. Specifically, Randomized Cross-Correlation highlighted four peaks of time lag, the first of -27 days with cross-correlation of 0.199 (seismic series lags geochemical

series), the second of 23 days with cross-correlation of 0.157, the third of 51 days with cross-correlation of 0.277 and the fourth of 74 days with cross-correlation of 0.229 (for 2nd, 3th and 4th peaks, geochemical series lags seismic series). Also in this case the results are considered significant, because they are greater than the 99% confidence interval, and because they are obtained considering a rather long period of volcanic activity characterized by intense volcanic activity.

Considering the volcanological framework and the results obtained by the quantitative comparison of geophysical and geochemical data, for the activity at Mt. Etna during the period between 2010 and 2012 it is possible to hypothesize pressurization and depressurization dynamics affecting the plumbing system similar to those highlighted for the same volcano during the 2013 activity. As shown by the multiparametric qualitative comparison conducted by Cannata et al. (2015) for 2013 Mt. Etna activity, evidences of considerable increase of soil CO_2 flux before lava fountaining sequences at NSEC (**Fig. 2.9**) and the relationship with increase of volcanic tremor RMS amplitude would be compatible with the hypothesis of pressurization stages of shallow plumbing system before lava fountaining sequence, likely associated with the uprise of gas-rich magma. The fact that the soil CO_2 flux precedes volcanic tremor time series by some tens of days can be associated with the different source depth. Indeed, the largest exsolution of the CO_2 initially dissolved in basaltic magmas takes place at about 12 km b.s.l. (Caracausi et al., 2003), determining increases in soil CO_2 flux both from the vents and the slopes of the edifice. On the other hand, the source of volcanic tremor, likely related to fluid dynamics within the plumbing system (e.g. Chouet and Matoza, 2013), is much shallower and generally is located about 1.5 -2.0 km a.s.l. (e.g. Di Grazia et al., 2006; Patanè et al. 2008; D'Agostino et al., 2013; Cannata et al., 2015). In the light of it, the time lag can be related to the transfer velocity of magmatic fluids from the deeper to the shallower portions of the volcano. Considering that variations in soil CO_2 flux series precede variations in volcanic tremor series of about 35 days and that the considered parameters source are localized at different depth, assuming that the magma ascent was a continuous process, for 2011-2012 activity at Mt. Etna it is possible to estimate an average

speed of magma ascent as about 0.004 m s^{-1} that means about 380 m day^{-1}. This retrieved average speed is consistent with some previous estimations carried out at Mt. Etna volcano (e.g. Allard, 1997; Caracausi et al., 2003, Cannata et al., 2009) and compatible with different model to estimate shallow- and deep-level ascent rates (e.g. Aloisi et al., 2006; Armienti et al., 2013).

As evidenced by Cannata et al. (2009), also for the considered eruptive activity it is possible to hypothesize ingression of "new" magma in the deep volcanic feeding system and its subsequent ascent toward the surface and hence increase of the CO_2 release. The ascent of new magma probably pushed ''old'' magma, already residing at shallow depth, to rise up through cracks and conduits located at very shallow depth.

The different lags observed with the quantitative comparison between volcanic tremor amplitude and SO_2, instead, are more difficult to interpret and reflect a complex situation. Probably, the different lags can be interpreted as the result of different mechanisms that influence the sulfur dioxide flux. Likewise of the soil CO_2 flux, the negative time lag can be attributed to the magma ascent toward the surface, reflecting the deeper source of SO_2 release (a few km of depth; e.g. Burton et al., 2003) with respect to volcanic tremor but at the same time its shallower source with respect to the CO_2. The positive time lags, on the other hand, could be compatible with a downward-propagating decompression of the volcanic plumbing system following the eruption. In particular, the volcanic tremor source could be related to shallow degassing and eruptive activity, that might produce a downward-propagating decompression increasing the SO_2 release in depth. Tarasewicz et al. (2012) proposed the downward-propagating decompression model to explain the eruption activity at Eyjafjallajökull during 2010; from seismic evidence, they have suggested that depressurization of the summit magma chamber began to affect the deeper magmatic plumbing system by downward propagation of decompression wave. At Mt. Etna, Cannata et al. (2015) similar dynamic was proposed by to explain the dynamics that characterized the eruptive phases of volcano activity during 2013.

2.6 SUGGESTED FUTURE WORK

In order to confirm the hypotheses of pressurization and depressurization dynamics affecting the shallow plumbing system of Mt. Etna during the 2010-2012, as well as the interpretation of the observed time lags, future works could be aimed at:

- extending the quantitative multiparametric comparison of time series to other parameters for the same examined period, for example ground data deformation such as tilt and strainmeter;
- applying the same approach and the same analyses to other longer periods of volcanic activity at Mt. Etna in which similar dynamics have been observed, i.e. the cycles of lava fountains at the NSEC that have characterized the most recent activity of the volcano.

A successful application of these analyses for the quantitative multiparametric study of volcanic activity would not only improve the knowledge about internal volcano dynamics but could allow the development of strategies able to identify automatically significant changes in trends, identify synchronous/delayed changes in trends between different data, with a significant improvement in hazard assessment.

CHAPTER 3 – MOMENT TENSOR INVERSIONS OF MT. ETNA VOLCANIC TREMOR DURING LAVA FOUNTAINING: THE CASE STUDY OF 05 AUGUST 2011 EVENT

3.1 SOURCE MODELS AND CHARACTERIZATION OF LP SEISMIC SIGNALS

Moment tensor inversion represent one of the best ways to investigate the seismic source in volcanoes. In this chapter, moment tensor inversion theory and methodology will be illustrated.

3.1.1 Source model and trigger mechanism for LP seismicity

Interpretation of seismic volcano signals and quantification of their source mechanisms are the main goals of modern volcano seismology (Chouet and Matoza, 2013). The spread of broadband seismic networks for volcano monitoring and better computing power have allowed the development of powerful analysis techniques able to uncover the role of magmatic and hydrothermal fluids in the generation of seismic waves.

Since the late 1970s, some authors have dedicated their activity to understand the source dynamics and behavior that generate long-period (LP) seismicity. LP seismicity includes LP events and tremor, typical seismic signals due to the dynamics of magmatic and hydrothermal fluids (Chouet, 1996). Tremor is the most distinctive seismic signal recorded at several volcanoes, can last minutes, hours, even months or years and it is possible to observe it during quiescent or eruptive stages (McNutt, 2005). LP events, instead, resemble small tectonics earthquakes in duration but differ in their characteristic frequency range and harmonic signature (Chouet and Matoza, 2013). Volcanic tremor and LP events show some similarities: in fact, volcanic tremor share similar frequencies (0.2 – 5.0 Hz) and spectral content with LP events; moreover, authors suggested that is possible to hypothesize the origin of tremor as an overlap of a sequence of LP events (Chouet and Matoza, 2013 and references therein).

Several source physical mechanisms at source that can describe the generation of LP seismicity have been proposed; the debate on the source models and trigger

mechanisms at the basis of LP events is still open. For an overview of current knowledge, in the next sections I will refer to the papers of Kostantinou and Schlindwein (2002) and Chouet and Matoza (2013), where the authors have exhaustively illustrated the state of the art for the topics in question.

3.1.1.1 The crack model

For the first time, Aki et al. (1977) proposed a source model to explain the mechanisms for the volcanic tremor recorded at the volcano Kilauea (Hawaii) during 1963's eruption. The authors proposed a simplified two-dimensional fluid-driven crack model for tremor which consisted in the oscillations of the cracks walls caused by the opening of channels due to excessive magmatic pressure.
A few years later, LP events were recorded during 1980-86 Mt. St. Helens eruption. Fehler and Chouet (1982) interpreted these LP events as generated from excitation of a fixed cavity under the active crater. In the following years different models based on the resonance of fluid-filled cavity have been proposed, hypothesizing different resonator geometries, mainly pipes (e.g. Chouet, 1985) and cracks (e.g. Chouet, 1986), using numerical modeling. These models had in common the presence of crack wave, very slow waves propagating through the fluid and reflecting back and forth at the crack tips. Ferrazzini and Aki (1987) studied analytically the behavior of this wave and obtained a reasonable source of radiations in case of finite cracks. Moreover, the authors established that the crack wave velocity is slower than the acoustic velocity of the fluid at all wavelengths and is inversely dispersive (velocity decreases with increasing wavelength and crack stiffness). Therefore, resonance of the fluid reservoir depends on its geometry and on physical properties of the fluid and the surrounding elastic solid. In detail, Chouet (1986, 1988) has found dependence on the following parameters (**Fig. 3.1**): (i) crack geometry, (ii) position and area over which the pressure transient occurs, (iii) boundary conditions for the stress on the crack's surface and the fluid flow at the crack perimeter and (iv) a dimensionless quantity called the crack stiffness C and the fluid-solid impedance contrast Z, defined as:

$$C = \frac{bL}{\mu d} \ , Z = \frac{p_s \alpha}{p_f a}$$

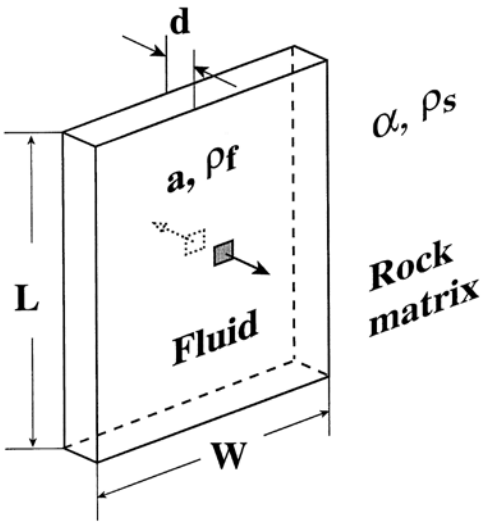

Figure 3.1. Geometry of the fluid-filled crack model described by Chouet (1986, 1988)

where b is the bulk modulus of the fluid, μ is the rigidity of the solid, L is the crack length, W is the crack width, d is the crack thickness, ρ_s is the density of the solid with P-wave velocity α, ρ_f the density of the fluid with P-wave velocity equal to a and L and W respectively length and width of a rectangular crack.

If on the one hand the model manages to explain the characteristic oscillations inside a volcano that produce the LP seismicity, on the other hand the trigger mechanism is not well known. However, it is known that many volcanic processes are involved in such as: (i) self-sustained oscillations, (ii) magmatic-hydrothermal interactions, (iii) magmatic degassing, (iv) brittle fracture of the melt and (v) solid extrusion dynamics and plug stick-slip.

3.1.1.2 Self-sustained oscillations

Several studies on the dynamics of magma fluid flow have made it possible to hypothesize how self-sustained oscillations can generate volcanic tremor.

Julian (1994) proposed a third-order system of non-linear ordinary differential equations that describe the flow inside a vertically extending crack connecting an upstream and a downstream reservoir. The non-linearity derives from the

assumption that any process of tremor generation based on a linear system cannot spontaneously oscillate. In his model, a flow induced oscillation in channels transporting magmatic fluid, channels that are constricted between deformable visco-elastic walls (**Fig. 3.2**).

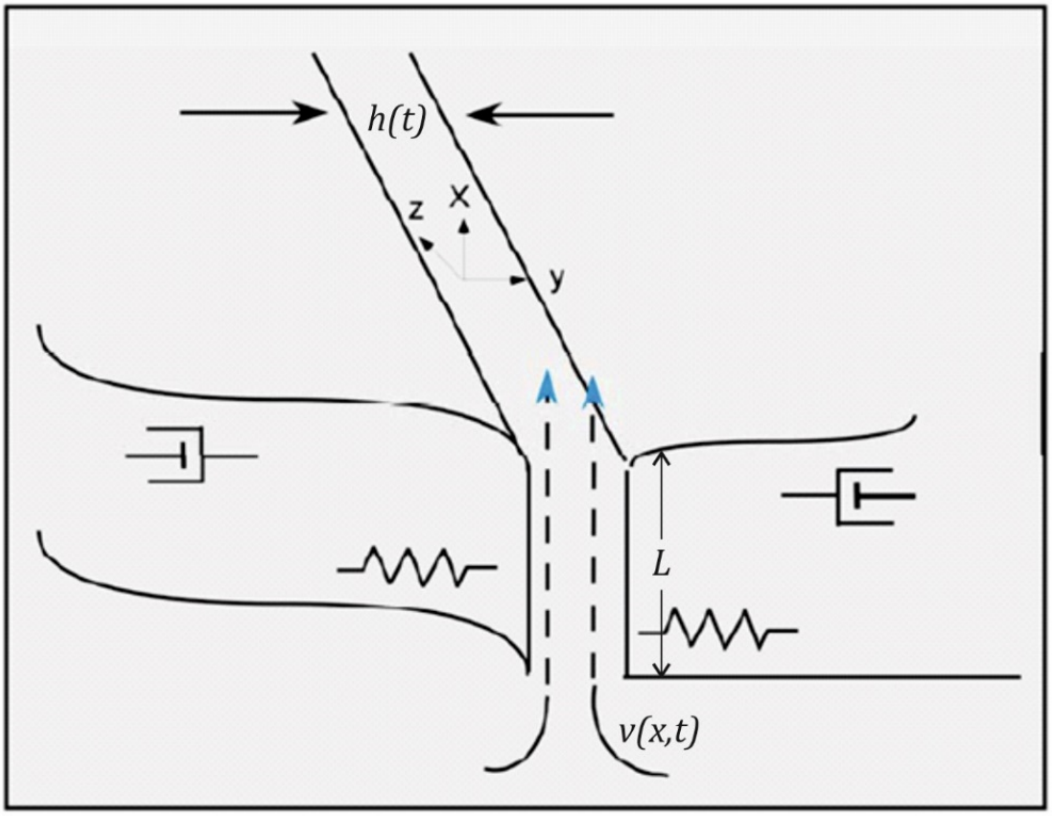

Figure 3.2. Model of the generation of volcanic tremor (Julian, 1994 – mod.). Viscous, incompressible fluid flows in x direction from upstream (bottom) to downstream (top) reservoir through a channel of length L with imperfectly elastic walls (springs and dashpots represent these properties). The model is two-dimensional; all motion occurs in the xy plane and is independent of z. The dynamical variables are the channel thickness $h(t)$ and the fluid flow speed $v(x,t)$.

The channel thickness varies in time with the variation of the fluid pressure, which causes a deformation of the walls in the y direction. Hence, since an increase in the flow speed produces a decrease in the fluid pressure (Bernoulli Effect), the walls move towards each other. As a result, the fluid is constricted causing a pressure increase that forces the channel walls to open again. The cyclic repetition of this process can trigger oscillations resembling long-period earthquake (Julian, 1994). The process in question is dependent on variables such as system

geometry, pressure and properties of the fluid. The model can explain both the generation of tremor and LP events. When the fluid-flow velocity is below a critical threshold the system is steady, but a perturbation such an earthquake, heterogeneities in the fluid or changes in the channel can determine the exceeding of the critical threshold and a disturbance of the steady state. In these conditions, the fluid creates oscillations until the steady state is reached again.

Beyond the model proposed by Julian, Balmforth et al. (2005) considered a model based on viscous flow along a uniform conduit comprised of two semi-infinite elastic slabs to study the excitation of propagating waves using long-wave expansion and linear stability theory. They concluded that fast flow through a thin channel of fluids exsolved from magma leads to the origin of flow-induced oscillations, if speed flow is greater than a critical value. This type of instability is called "roll waves"; to obtain this instability, Balmforth et al. (2005) hypothesized the exceeding of the flow-fluid speed threshold, called $v_{crit\,roll}$, defined as:

$$v_{crit\,roll} = \beta \sqrt{\frac{\rho_s}{\rho_f} \varepsilon}$$

where $\beta = \sqrt{\mu/\rho_s}$ is the shear wave velocity in the solid, ρ_s/ρ_f is the rock-to-fluid density ratio, and ε is the channel aspect ratio (thickness/length) with ε<<1. For example, for flow through a channel with aspect ratio $\varepsilon = 10^{-4}$ in a solid with shear wave speed $\beta = 2\ km\ s^{-1}$ and $\rho_s = \rho_f$, the equation suggests that flow speeds of tens of meters per second are required for instability (Chouet and Matoza, 2013).

Rust et al. (2008) investigated the conditions for roll wave instability; they concluded that roll waves are unlikely to explain volcanic tremor in many cases, but could possibly occur in the flow of hot, high-pressure H_2O- and CO_2-rich fluids at sustained flow speeds on the order of $10\ m\ s^{-1}$.

3.1.1.3 Magmatic-hydrothermal interactions

The magmatic-hydrothermal interactions represent one of the first trigger mechanisms proposed able to explain the origin of LP seismicity in volcanic area (Chouet, 1985). This broad family of processes invoked to understand the origin of LP seismicity includes: (i) boiling and depressurization of ground water (Leet, 1988; Matoza and Chouet, 2010), (ii) cyclic collapse and recharge of pressurized hydrothermal cracks (Arciniega-Ceballos et al., 2012; Matoza and Chouet, 2010; Matoza et al., 2009; Nakano, 2005; Ohminato et al., 2006; Waite et al., 2008) and (iii) unsteady chocking of a supersonic flow of magmatic steam (Chouet et al., 1994; Morrissey and Chouet, 1997).

The first evidences of links between magmatic-hydrothermal interactions and LP seismicity were inferred with studies on the activity at Kusatso-Shirane volcano, Japan.

This andesitic stratovolcano is characterized by three summit craters lake, is located in the region of Japan with the highest presence of hot-spring and shows LP events with nearly monochromatic coda (Hamada et al., 1976; Fujita et al., 1995). Analysis of LP events recorded at Kusatso-Shirane volcano have highlighted fluid-resonance with attenuation characteristics of hydrothermal fluids (Nakano et al., 1998; Kumagai et al., 2002a). Specifically, Nakano et al., (1998) determinate the complex frequencies of LP events using Sompi method (Kumazawa et al., 1990); so, they have obtained a coefficient Q which is function of the density of the fluid and of the geometry of the resonator such as

$$Q^{-1} = Q_r^{-1} + Q_i^{-1}$$

where Q_r^{-1} and Q_i^{-1} are the radiation and intrinsic losses respectively. In details, Q_r^{-1} is a function of the resonator geometry and sound speed and density of the fluid and can be evaluated using the fluid-filled crack model (Kumagai and Chouet, 1999, 2000, 2001; Morrissey and Chouet, 2001), while intrinsic attenuation Q_i^{-1} corresponds to intrinsic losses in the fluid, e.g., viscous, thermal and acoustic

damping. Kumagai et al., (2002b) studied the temporal evolution of Q by analyzing a sequence of 35 LP events recorded at volcano Kusatso-Shirane during the period between August 1992 and January 1993; they came to the conclusions that possible changes in the fluid composition of the LP resonator could have occurred. They interpret these changes in Q as due to an initially wet misty gas becoming progressively drier with time in response to drying out of the hydrothermal system caused by to magmatic heating. Assuming the existence of a sub-horizontal crack repeatedly excited at about 300 m depth, Nakano et al. (2003) performed LP events waveform inversion for the same volcano. They proposed a conceptual model for the source process of LP seismicity at Kusatsu-Shirane (**Fig. 3.3**), where magmatic heating causes a gradual buildup of steam pressure in a hydrothermal crack, which causes repeated discharges of steam from the crack.

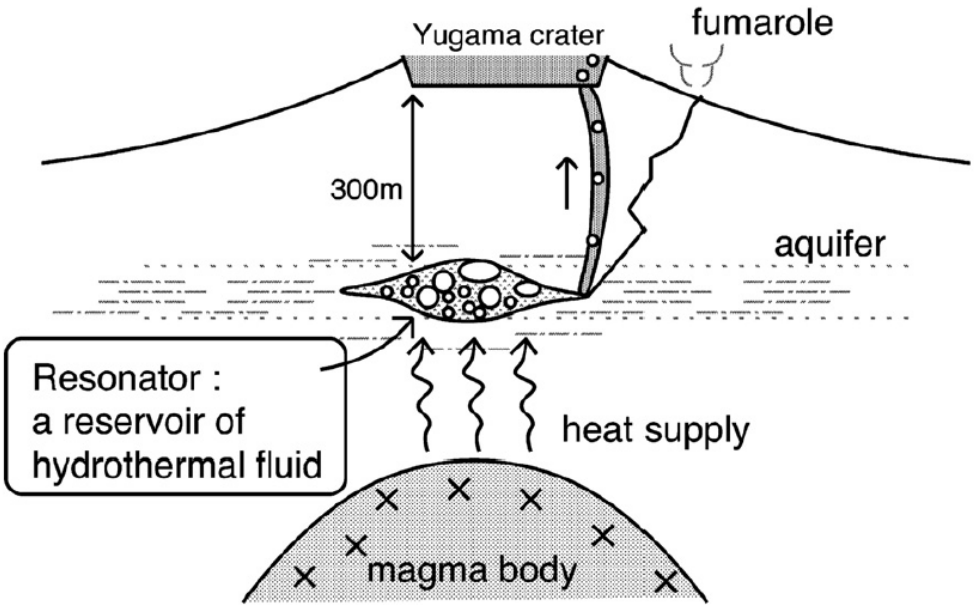

Figure 3.3. Schematic view of the source process of LP events at Kusatsu-Shirane Volcano. (Nakano et al., 2003)

Similar observations, source mechanisms, and linking LP seismicity to magmatic–hydrothermal interactions have been detected in several volcanoes such as Kilauea (Almendros et al., 2001a,b; Saccorotti et al., 2001; Kumagai et al., 2005); Redoubt (Chouet et al., 1994; Morrissey and Chouet, 1997; Stephens and Chouet,

2001); Mount St. Helens (Waite et al., 2008; Matoza et al., 2009a; Matoza and Chouet, 2010); Popocatépetl (Arciniega-Ceballos et al., 2012); Satsuma-Iwojima (Ohminato, 2006); Ontake (Nakamichi et al., 2009)**;** Aso (Kaneshima et al., 1996; Kawakatsu et al., 2000); Pinatubo (Harlow et al., 1996); Campi Flegrei (D'Auria et al., 2011); and La Fossa, Vulcano (Alparone et al., 2010).

3.1.1.4 Magmatic degassing

Magmatic degassing is one of the most widespread trigger mechanisms of Long-Period seismicity that can be found in volcanoes. Evidences of links between magmatic degassing and LP seismicity have been highlighted by several studies based on different types of analysis.

At low-viscosity basaltic volcanoes such as Pìton de la Fournaise (Reunion), Kilauea (Hawaii) and Stromboli (Italy), several authors associate LP seismicity with transport and eruption. At Pìton de la Fournaise, Aki and Ferrazzini (2000) concluded that the LP events were associated with the lateral path of magma towards the rift zones and not with magma movement along a separate vertical path to the summit. At Kilauea (Ohminato et al., 1998; Chouet and Dawson, 2011) and Stromboli (Chouet et al., 1997, 2003, 2008), instead, authors concluded that LP seismicity may be generated as part of a broadband source process associated with the unsteady transport of magma and gases through conduits.

At Mt. Etna, a basaltic stratovolcano, more studies have been shown the links between LP seismicity and typical effusive and explosive eruptions.

Tremor locations using spatial amplitude decay allowed to obtain information on the geometry of the shallow feeding system at Mt. Etna (Italy), while time variations of tremor, LP, and VLP events are explained by the transport and discharge of gas-rich magma (Patanè et al., 2008). Consistent Q values of LP events, instead, have been found with resonance in cracks filled with bubbly basalt or water–vapor mixtures (Saccorotti et al., 2007; Lokmer et al., 2008; Patanè et al., 2008). By moment tensor inversions, De Barros et al. (2011) found that 2008-2009

LP events at Mt. Etna are well-explained by highly volumetric sources, likely characterized by crack-like geometries. In particular, they conclude that the LP events are likely related to gases, rather than magma movement, in shallow part of the volcanic edifice identified by previous studies (Patanè et al., 2008, De Barros et al. 2009).

Gil Cruz and Chouet (1997) analyzed LP events and spasmodic and harmonic tremors recorded at Galeras, an andesitic stratovolcano localized in Colombia. During 1989-1993, Galeras was characterized by a series of explosive eruptions after 1988 reactivation. In particular, they focused on LP events accompanying the emplacement, extrusion, and ultimate destruction of a lava dome in the crater this volcano. Gil Cruz and Chouet (1997) hypothesized a model for generation of the LP signals, where periodic collapse of a foam layer atop a magma conduit beneath the solid lava dome induces a rapid ascent of a gas slug. Specifically, the ascent was possible thanks to a pre-existing crack able to act as the main escape pathway. Other evidence of the relationship between magmatic degassing and LP seismicity have been found in basaltic-andesitic volcano such as Arenal, Costa Rica (Benoit and McNutt, 1997**;** Garcés et al., 1998; Hagerty et al., 2000**;** Métaxian et al., 2002; Lesage et al., 2006; Davi et al., 2010, 2012) and andesitic volcanoes such as Volcán de Colima, Mexico (Zobin et al., 2008; Palo et al., 2009; Varley et al., 2010a,b), Soufriere Hills Volcano, Montserrat (Rowe et al., 2004) and Tungurahua, Ecuador (Molina et al., 2004). Although with the differences due to the volcanic frameworks, in each of these cases different models, similar to those above described, have been proposed. In general, models for the magmatic degassing are very similar to those proposed for the magmatic-hydrothermal interactions.

3.1.1.5 Brittle fracture of melt

Recent studies have highlighted the possibility that brittle fracture of melts could be one of the volcanic processes capable of generating LP seismicity. In particular, experimental and numerical evidences have shown that in condition of realistic

magma conduits (Collier and Neuberg, 2006; Gonnermann and Manga, 2007; Hale, 2007; Papale, 1999; Thomas and Neuberg, 2012) highly viscous melts can exhibit solid–like brittle behavior (Alidibirov and Dingwell, 1996; Dingwell, 1996; Ichihara and Rubin, 2010; Webb and Dingwell, 1990).

This process is based on non-Newtonian behavior of silicate melts as a result of high strain rates. When this condition is realized, a transition from viscous-fluid-like to solid-like mechanical behavior (Webb and Dingwell, 1990) can be observed. The discoveries of fossil magmatic conduits have allowed to evidence brittle failure in the conduits, a phenomenon that is not easy due to the intense hydrothermal alteration. However, after partial collapse, two well-preserved young-rhyolitic conduits at Torfajökull (Iceland) have been found (Tuffen and Dingwell, 2005; Tuffen et al., 2003); the field observation have shown veins formed in young rhyolitic conduits filled of fragments of magma and broken phenocrystals interpreted as linked to faulting and volcano seismicity.

As highlighted by Lahr (1994), the dynamics characterizing the brittle failure in certain regions of the plumbing system can also be associated with hybrid LP seismicity. Neuberg et al., (2006) proposed a link between the hybrid events signal and shear-failure in the conduit consequent to brittle behavior of magma near the glass transition.

Brittle failure of melt for generating LP/hybrid events is a newly topic of increased interest. Its better understanding could provide links between seismicity, extrusion dynamics, magma movement in conduits and also link to ground deformation and tilt (Green and Neuberg, 2006; Neuberg et al., 2006; Voight et al., 1999).

3.1.1.6 Solid extrusion dynamics and plug stick-slip

Unlike previous cases, for solid lava dome extrusion and plug flow the fluid-filled crack model doesn't explain the resonance of the conduit able to generate shallow LP seismicity and hybrid events. Thanks to studies carried out by several authors,

the 2004-2008 eruption at Mount St. Helens allowed to investigate the link between seismicity and eruptive dynamics. During this period, the volcano activity was characterized by a very regular shallow seismicity with slowly evolving waveforms (Moran et al., 2008) and for their regular nature these events were termed drumbeats (Moran et al., 2008). As for the generation process of those drumbeats at St. Helens, Iverson et al. (2006) and Iverson (2008) proposed a mechanical model based on the existence of a solid plug pulled upward by a constant flux of molten (bubbly) magma at depth in the conduit (**Fig. 3.4**) where seismic events would correspond to stick-slip motion of the lava plug. Moreover, stick-slip motion would occur on the margins of the lava plug where extrusion is resisted by friction forces.

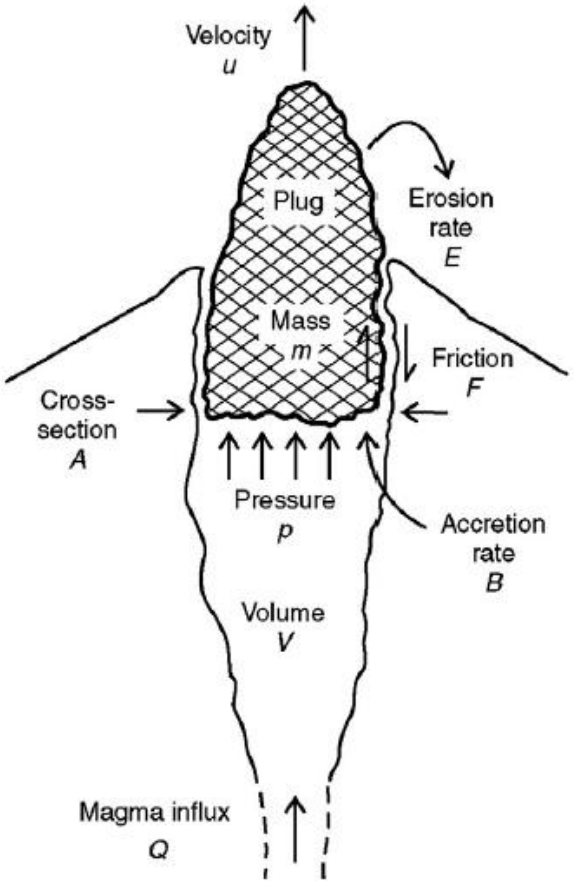

Figure 3.4. Cartoon illustrating the conceptual stick–slip model of Iverson et al. (2006) and Iverson (2008). A constant flux of magma pushes on a rigid plug of solidified magma occupying the upper ~0.5 km of conduit. Extrusion is resisted by the frictional force at the conduit wall and plug weight. Earthquakes result from incremental slip along the plug margins (see Iverson et al., 2006 for details). Figure reproduced from Iverson et al. (2006).

Seismic events with drumbeats style have been registered at Augustine (Alaska) during 1986 dome building phase and 2006 effusive phase (Power and Lalla, 2010). In this case, drumbeat seismicity at volcano is related to the shallow movement of magma and the formation of lava domes but is not likely directly caused by the emplacement of lava domes at the volcano's summit.

3.1.1.7 Slow-rupture earthquake

Installation of high-resolution broadband seismic networks in volcanoes recently allowed the development of new models to explain shallow long period seismicity. Bean et al. (2014) analyzed very-high-resolution seismic data from three active volcanoes — Mt. Etna (Italy), Turrialba (Costa Rica) and Ubinas (Peru) — measured between 2004 and 2009. Considering 2008-2009 eruption at Mt. Etna, Bean et al. 2014 found that for the same low frequency seismic events recorded, at the summit stations appeared as pulse-like low frequency signals, while at the further stations appeared as classical resonating LP signals. They explained the signals recorded at these last stations by attributing the causes at propagation effects in the medium and not at source mechanisms. Similar evidences are also found in Turrialba and Ubinas volcanoes. To support this new theory, supposing fixed crack geometry and stiffness conditions for resonance, they carried out a series of test with which they found that the corner frequency of the LPs does not scale with events size. Based on 2004 field campaign on Mount Etna, they showed how the corner frequency of events scales with moment magnitude and attributed those events as caused by dry failure (**Fig. 3.5**). For these LPs, Bain et al. (2014) hypothesized a model where seismic evidence are consequence of failure in materials in brittle-ductile transition. The brittle-ductile transition in volcanic material is related to the low friction angles of the unconsolidated shallow volcanic deposits and not to high pressure and temperature.

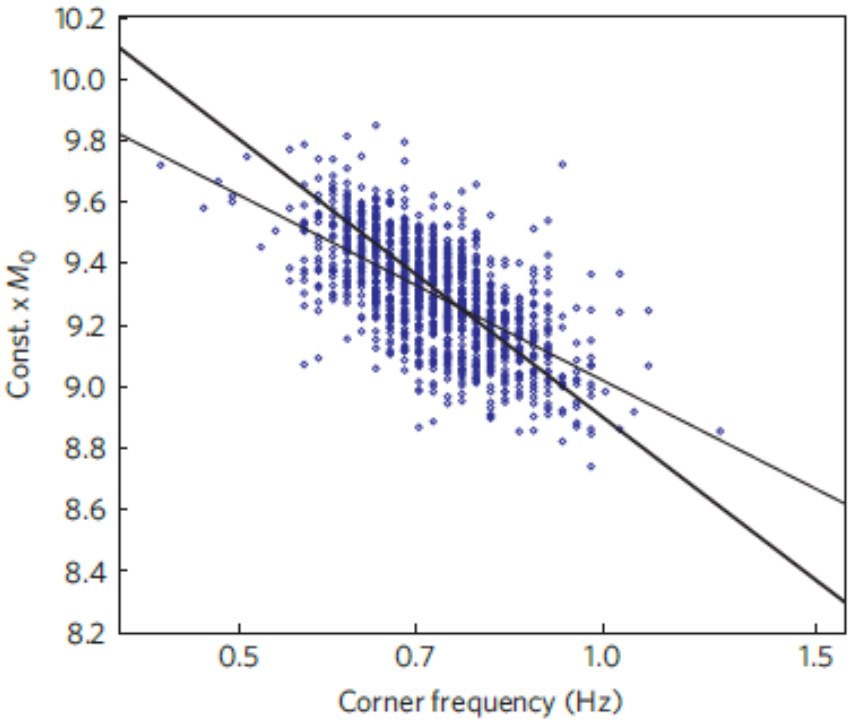

Figure 3.5. Scaling of long-period seismic moment magnitude versus corner frequency. The amplitude spectra of 1,150 long-period events, recorded in March 2004 at Mount Etna near-summit station (ECPN) are fitted with ω^2 source model, to determine the corner frequency. The y axis is proportional to the seismic moment. The thin line is best fitting with slope -2.2; the thick line has slope -3 and is broadly consistent with the data. (Reproduced from Bean et al., 2014).

3.1.2 Seismic Sources characterization of LP seismicity

3.1.2.1 The inverse problem

The inverse problem is recurrent in science, especially in geophysics. The main goal of the inverse problem is to reconstruct a model starting from a set of measurements.

For the inverse problem, measurements and model are related through one or more implicit equations. These equations can be compactly written as the vector equation $\boldsymbol{f}(\boldsymbol{d}, \boldsymbol{m}) = \boldsymbol{0}$ which synthetizes what is known about the relationship between measurements data ($\boldsymbol{d}$) and model parameters ($\boldsymbol{m}$). The main aim of

inverse theory is to solve or "invert" these equations to retrieve the model parameters (Menke, 1984).

In an ideal case, it would be possible to correctly determine the model from the data; however, measurements are affected by errors, they are often incomplete and therefore do not provide sufficient information to allow to determine the model uniquely. Generally, this is due to the use of a finite amount of data to reconstruct a model with infinite degrees of freedom. This means that the inverse problem does not have a unique solution: in fact, for the same set of measurements, several equally good models are possible. Follows that the obtained model and the real model may not be necessarily equal.

Let us consider the model parameters $\boldsymbol{m}$ of length n as

$$\boldsymbol{m} = [m_1,\ m_2, \dots, m_n]^T \tag{3.1}$$

and data $\boldsymbol{d}$ of length l as

$$\boldsymbol{d} = [d_1,\ d_2, \dots,\ d_l]^T \tag{3.2}$$

where T indicates the transposed matrix. The relationship between $\boldsymbol{d}$ and $\boldsymbol{m}$ can be expressed by explicit equation

$$\boldsymbol{d} = \boldsymbol{A}\boldsymbol{m} \tag{3.3}$$

where $\boldsymbol{d}$ is an l-dimensional data vector, $\boldsymbol{m}$ is an n-dimensional model parameters vector and A is a l x n matrix of coefficients defined as a theory operator (Snieder and Trampert, 1999) or data kernel (Menke, 1984; Gubbins, 2004). Starting from the data, an estimated model called $\boldsymbol{m}^{\boldsymbol{est}}$ is reconstructed. Generally, the estimated model differs from real model for two main reasons: (i) the errors charactering data and (ii) the non-uniqueness of the inverse problem. Therefore, considering the errors for the estimated model, the equation (3.3) becomes:

$$\boldsymbol{d} = \boldsymbol{Am} + \boldsymbol{e} \tag{3.4}$$

where $\boldsymbol{e}$ is an l-dimensional errors vector associated by l-dimensional $\boldsymbol{d}$ data vector. Many inverse problems are not linear, but often they can be linearized by making suitable approximations. In this case, the explicit equation (3.4) represent a linear inverse problem.

When the data kernel is a square matrix ($l = n$), the number of equations equals the number of unknowns and the problem is defined as equi-determined. In this case there is only one solution and it has zero prediction error (Menke, 1984). When A is an ($l < n$) matrix, there are less linearly independent equations than unknowns and the problem is known as under-determined. In this case, although the data provides information about the model parameters, they do not provide enough information to determine them uniquely. In order to obtain a solution, we must add to the problem some "extra" information. This "extra information" is called *a priori* information. When A is an ($l > n$) matrix, there are more independent equations than unknowns, the problem in this case is defined as over-determined. A common way to estimate a model is to seek the $\boldsymbol{m^{est}}$ that gives the best fit of the data, e.g. the smallest difference between the data and the product $\boldsymbol{Am}$. One of the most common approaches to best fit $\boldsymbol{m^{est}}$ is defined as "the least square solution of a linear inverse problem". The least square solution to the inverse problem defined by equation 3.3 is given by (derivation of this equation is given in Menke, 1984):

$$\boldsymbol{m^{est}} = [\boldsymbol{A^T A}]^{-1}\boldsymbol{A^T d} \tag{3.5}$$

If the predicted data $\boldsymbol{d^{pre}}$ (e.g. the product Am) are as close as possible to the observed data $\boldsymbol{d^{obs}}$, the prediction error is minimized. For each i-th observation where $i = (1, \dots, N)$, the i-th prediction error or misfit is given by

$$\boldsymbol{e_i = d_i^{obs} - d_i^{pre}} \tag{3.6}$$

When the sum "E" of the all individual misfits ($E = \sum_{i=1}^{N} e_i^2 = e^T e$) has the smallest value, the best model parameters are obtained. Therefore, the method of the least square solves the inverse problem by finding the model parameters that minimize a particular measure of the estimated data (Menke, 1984). The L_2 norm is used to quantify this length and it is expressed by

$$L_2 = \left[\sum_i |e|_i^2\right]^{\frac{1}{2}} \tag{3.7}$$

From equation 4.4 ($\boldsymbol{e = d - Am}$), E can be written as

$$E = \boldsymbol{e^T e} = \boldsymbol{(d - Am)^T (d - Am)} \tag{3.8}$$

As already mentioned, errors play a fundamental role in the inversion process. In order to improve the accuracy of the inversion process, it may be useful to introduce a weight function; therefore, it is possible to consider a new E, defined as follows:

$$E = \boldsymbol{e^T W_e e} \tag{3.9}$$

where W_e is a matrix which defines the relative contribution of each individual component to the total prediction error. In general, $\boldsymbol{W_e}$ is defined as a diagonal matrix. Considering the weight function, (4.5) and (4.8) equations can be transformed in, respectively:

$$\boldsymbol{m^{est} = [A^T W_e A]^{-1} A^T W_e d} \tag{3.10}$$

$$E = \boldsymbol{e^T e} = \boldsymbol{(d - Am)^T W_e (d - Am)} \tag{3.11}$$

An example of linearized inverse problem solved with least square solution can be considered the moment tensor inversion. In this case, minimizing the misfit between the recorded seismograms (the observed data) and calculated data (retrieved by the inversion process) is fundamental to obtain the best inversion.
Before describing the details of the moment tensor inversion, a discussion in next paragraphs about the seismic source models is illustrated.

3.1.2.2 The source function s(t)

As seen in the previous sections, the propagation of seismic waves in volcanic contexts can be set up by sources external to the edifice such as eruptions, explosions, pyroclastic flows, landslides and by internal sources such as shear failures, opening of pathways associated to fluid transport and tractions on conduit surfaces due to viscous fluid flow (Chouet, 1996). Generally, seismic sources are characterized by faults and volumetric changes. In according to elastic theorem (Aki & Richards, 2002), both types of volumetric and faulting sources can be treated in terms of body forces applied to the elements of a medium where the source is containing. Therefore, a seismic moment tensor constituted by a system of equivalent forces acting at a source point can represent a seismic source. An example of equivalent forces combination is proposed in **Fig. 3.6**. To satisfy the point source condition it is necessary to examine waveforms with a much longer wavelengths than the linear dimension of the considered source.
Identifying the combination of a seismic moment tensor is important as it allows to constrain the geometry and the mechanisms acting at the point source, hence that providing information on the history and magnitude of the seismic source.

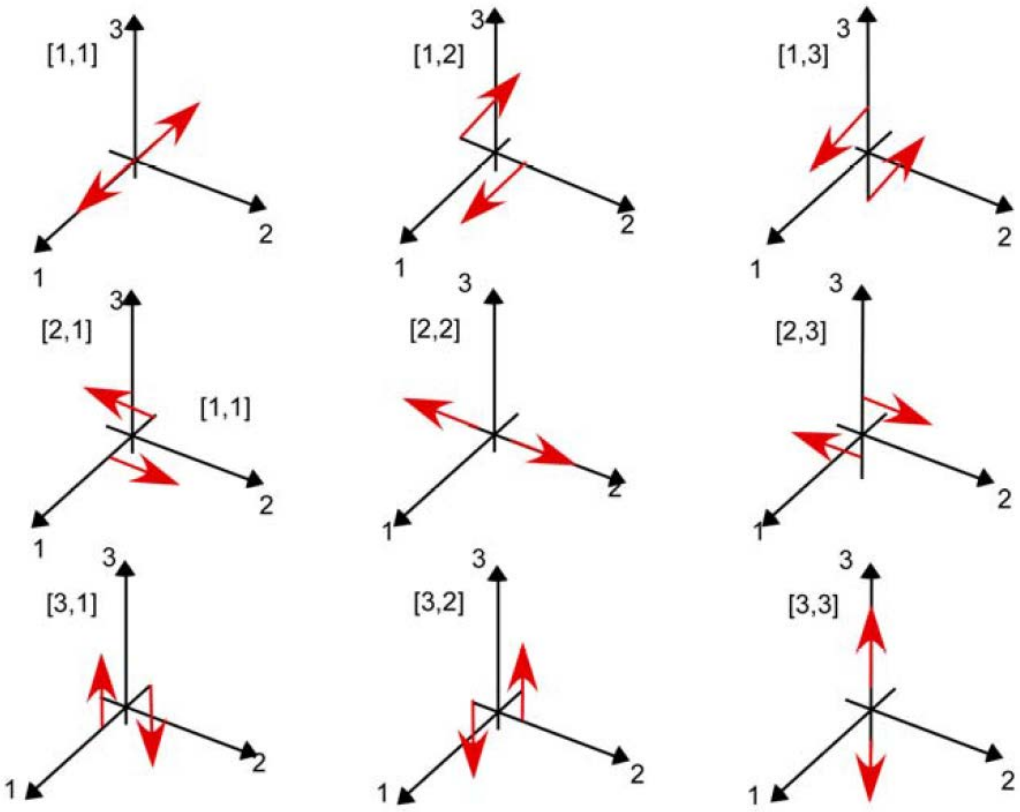

Figure 3.6. Combinations of double couple equivalent body forces and fault geometry. Double couple are used to avoid net torque or rotation of the fault, taken from Aki and Richards, (2002). In this scheme, 1 represents the x direction, 2 the y direction and 3 the z direction.

Mathematically, the moment tensor is a second-rank tensor that can be described by the equation 3.12. In seismology it is used as a mathematical representation that gives the seismic waves produced by a source involving displacements, varying in time and space. The moment tensor is composed of nine elements of force couples (off-diagonal) and dipole (diagonal elements).

$$M = \begin{bmatrix} M_{xx} & M_{xy} & M_{xz} \\ M_{yx} & M_{yy} & M_{yz} \\ M_{zx} & M_{zy} & M_{zz} \end{bmatrix} \tag{3.12}$$

A force couple or dipole is defined as two forces of magnitude f acting in opposite direction at distance d (see **Fig. 3.7**). The magnitude of force couples or dipole is given in $[dyn * cm]$ or $[N * m]$.

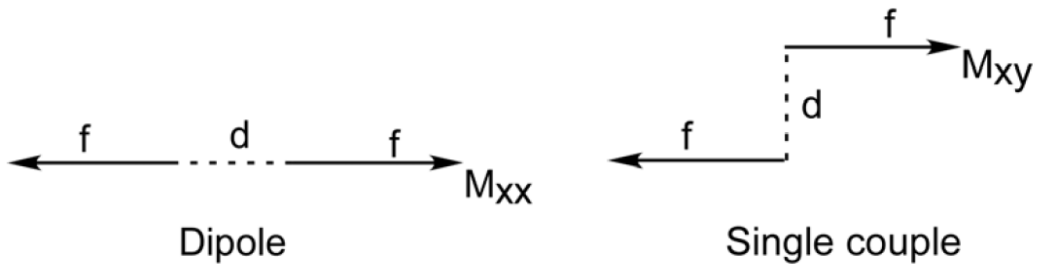

Figure 3.7. Representation of single couples and dipoles oriented in different directions (Stein and Wysession, 2003).

The seismic moment tensor can be considered symmetric based on the law of angular and linear momentum. This means that only six of the nine components are independent, and this is possible only when a force couple is balanced by its counterpart (e.g. a double couple in **Fig. 3.8**). Nevertheless, the use of single force couples would generate torque and thus observable rotations of source region.

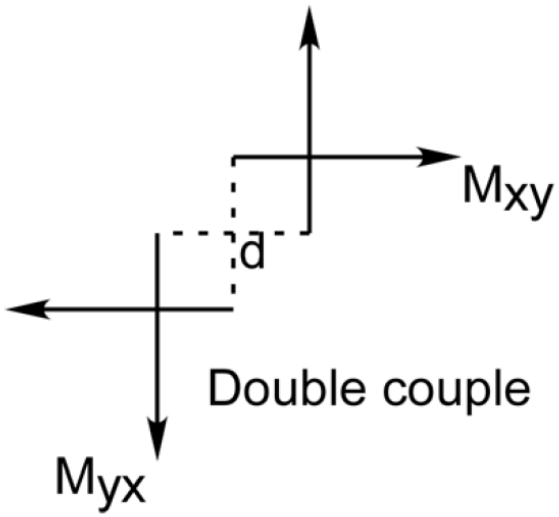

Figure 3.8. Representation of double couple along the xy direction (Stein and Wysession,2003).

Until the 1960s, seismologists debate about the suitability of single couple versus double couples. Indeed, P-wave radiations produced by either of the two models are the same and they can be distinguished only on the grounds of S waves. In the following years, the debate was overcome thanks to the availability of more high-quality data and double couple model was unambiguously determined to be more appropriate (Lay and Wallace, 1995). Nowadays, the moment tensor components

are expressed as a combination of double couples, the use of which allows the total net torque component to be neglected.

The seismic moment tensor can be retrieved through an inversion procedure that involves a time dependent seismogram. Following Stein and Wysession (2003), the seismograms at surface are the result of convolution of three different components and can be described by the general equation

$$u(t) = s(t) * g(t) * i(t) \tag{3.13}$$

where the seismogram recorded on the surface $u(t)$ can be expressed as the convolution of three different terms as a function of time that are the source $s(t)$, the medium $g(t)$ and the instrument $i(t)$.

According to Aki and Richards (2002), the equation 3.13 can be expressed in the following equation:

$$u_n(\boldsymbol{x}, t) = G_{np,q} * M_{pq} * S(t) \tag{3.14}$$

where $u_n(\boldsymbol{x}, t)$ represents the n-th components of ground displacement as a function of time t and space $\boldsymbol{x}$, M_{pq} is the force couple or dipole in the pq direction acting at the source, $G_{np,q}$ represents the n-th components of the spatial derivatives around the source position of the corresponding medium responses (Green's functions), and $S(t)$ is the source-time function.

Double couples model is ideal to explain source processes for tectonic earthquakes, but in the case of volcanic seismic signals it is not enough: in fact, in the case of volcanic context the local modifications of the stress field are induced by buried volcanic explosions, dyke injection or by thermal expansion. Therefore, seismic waves can originate from a physical process which involves a sudden volumetric change of the source area. In order to accurately describe the source process for LP seismicity, more than three single force components (**Fig. 3.9**) may be required. Takei and Kumazawa (1994) provided a theoretical justification for

the existence of single forces and torque components. In their model, the unbalanced forces and torques exchange linear and angular momenta between the source region and the rest of the Earth, with both types of momenta conserved for the entire Earth (Julian, 1998). Evidence of the role of single forces in seismic volcanic processes at source have been detected at more volcanoes such as Kilauea, Hawaii (Ohminato et al., 1998; Kumagai et al., 2005), Kusatsu-Shirane, Japan (Nakano et al., 2003), Stromboli, Italy (Chouet et al., 2003), Arenal, Costa Rica (Davi et al., 2010; 2012) and Mt. Etna, Italy (De Barros et al., 2011).

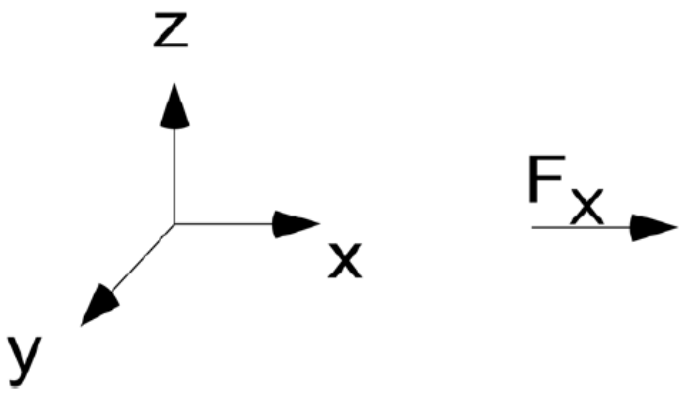

Figure 3.9. Representation of single force along the x direction (Stein and Wysession,2003).

During the ascent of a slug of gas in a column of liquid, gravitational energy can be released and this situation can be explained by single forces (Chouet, 2003). Ohminato et al. (1998) obtained solution for the analysis of very long period signals, associated with magma injection at Kilauea Volcano (Hawaii), by using also the single forces in the moment tensor inversion. Three different cases have been considered in their inversion procedure in which the source is assumed to be embedded in a homogeneous half space: (i) a volumetric source; (ii) a source with six moment tensor components, or (iii) a source with six moment tensor components and three single force components. They obtained the best solution when considering also the single forces components (case iii), reducing the difference between observed and calculated data. They assumed that these single force components are real and not due to artefacts of the inversion procedure.

They explained the single forces as drag forces applied on the walls of a narrow channel by magma as it flows.

Chouet et al. (2003) obtained solution for the analysis of very long period signals recorded in Stromboli in 1997 by using also the single forces in the moment tensor inversion. The retrieved source mechanisms are interpreted by these authors to be the results of two cracks and a vertical force of magnitude of 10^8 N initially directed downward then upwards. The vertical force is associated with mechanism of inflation and deflation that influence the direction of the force.

However, several authors have pointed out that uncertainties regarding source localization and velocity models can lead to spurious single forces (Bean et al., 2008; Chouet, 2003b; De Barros et al., 2011, 2013; Ohminato et al., 1998). By carrying out a synthetic test for different moment tensor inversion scenarios, De Barros et al. (2013) analyzed the effects of the single forces on the recovered solutions. They have shown how, for incorrect speed, models create the conditions to obtain spurious single forces. In particular, errors are higher both when plausible shallow low velocity layers are not considered.

3.1.2.3 The Moment Tensor Inversion

Considering the contribution of single forces, the previously proposed equation 4.14 becomes

$$u(\boldsymbol{x}, t) = M_{pq}(t) * G_{np,q}(\boldsymbol{x}, t) + F_p(t) * G_{np}(\boldsymbol{x}, t) \qquad (3.15)$$

where $n, p, q = 1, 2, 3$, F_p is the single force acting in the p direction, and G_{np} and $G_{np,q}$ represent the n-th components of the corresponding medium responses (Green's functions) and their derivatives, respectively. The asterisk indicates convolution and the summation convention are applied.

The equation 3.15 is a linear equation which is easily solved, provided we have a sufficient number of data (seismograms). Regarding computer memory and computational time, it is more convenient to solve this linear inverse problem in the frequency domain. Transforming the equation 3.15 to the frequency domain, it becomes:

$$u_n(\boldsymbol{x},\omega) = M_{pq}(\omega)G_{np,q}(\boldsymbol{x},\omega) + G_{np}(\boldsymbol{x},\omega)F_p(\omega) \tag{3.16}$$

where $u_n(\boldsymbol{x},\omega)$, $M_{pq}(\omega)$, $F_p(\omega)$, $G_{np,q}(\boldsymbol{x},\omega)$, $G_{np}(\boldsymbol{x},\omega)$ are the Fourier transform of the displacements, of the moment tensor components, of the single forces, and of the spatial derivatives and components of the Green's functions, respectively. In according to relative theorem, convolution in time domain is equivalent to multiplication in the frequency domain and equation 3.16 must be solved separately for each frequency. In explicit matrix form the equation 3.16 becomes

$$\begin{bmatrix} u_1 \\ u_2 \\ u_3 \\ \vdots \\ u_N \end{bmatrix} = \begin{bmatrix} g_{11,1} & g_{12,2} & g_{13,3} & g_{11,2} & g_{11,3} & g_{12,3} & g_{11} & g_{12} & g_{13} \\ g_{21,1} & g_{22,2} & g_{23,3} & g_{21,2} & g_{21,3} & g_{22,3} & g_{21} & g_{22} & g_{23} \\ g_{31,1} & g_{32,2} & g_{33,3} & g_{31,2} & g_{31,3} & g_{32,3} & g_{31} & g_{32} & g_{33} \\ \vdots & \vdots & \vdots & \vdots & \vdots & \vdots & \vdots & \vdots & \vdots \\ g_{N1,1} & g_{N2,2} & g_{N3,3} & g_{N1,2} & g_{N1,3} & g_{N2,3} & g_{N1} & g_{N2} & g_{N3} \end{bmatrix} \cdot \begin{bmatrix} M_{11} \\ M_{22} \\ M_{33} \\ M_{12} \\ M_{13} \\ M_{23} \\ F_1 \\ F_2 \\ F_3 \end{bmatrix} \tag{3.17}$$

where N is the total number of seismograms used in the inversion (including all the stations and all the components of ground motion), assuming the symmetrical moment tensor, that is, for ($M_{12} = M_{21},\ M_{13} = M_{31},\ M_{23} = M_{32}$) and

$$g_{np,q} = \begin{cases} G_{np,q} & p = q \\ G_{np,q} + G_{nq,p} & p \neq q \end{cases} \qquad n = 1, 2, 3, \dots, N \tag{3.18}$$

The equation 3.18 can be written in compact form as:

$$\boldsymbol{u} = \boldsymbol{Gm} \tag{3.19}$$

where $\boldsymbol{u}$ is the data (observed seismograms) matrix, $\boldsymbol{G}$ is the matrix containing the Green's function and $\boldsymbol{m}$ the moment tensor plus single forces components' matrix. If the number of the elements belonging to the matrix row $\boldsymbol{u}$ is greater than the number of the elements of matrix $\boldsymbol{G}$, the inverse problem expressed by equation 3.19 can be termed an overdetermined inverse problem.

Quality of inversion procedure is tested through the evaluation of the misfit (R) between calculated and observed data. R can be expressed by the following equation:

$$R = \frac{(\boldsymbol{u} - \boldsymbol{Gm})^T \boldsymbol{W} (\boldsymbol{u} - \boldsymbol{Gm})}{\boldsymbol{u}^T \boldsymbol{W} \boldsymbol{u}} \tag{3.20}$$

where $\boldsymbol{W}$ is a diagonal weighting matrix of the quality of the waveforms. It can be expressed in explicit matrix format as

$$\boldsymbol{W} = \begin{bmatrix} \boldsymbol{w_1} & \boldsymbol{0} & \cdots & \boldsymbol{0} \\ \boldsymbol{0} & \boldsymbol{w_2} & \cdots & \boldsymbol{0} \\ \vdots & \vdots & \ddots & \vdots \\ \boldsymbol{0} & \boldsymbol{0} & \cdots & \boldsymbol{w_N} \end{bmatrix} \tag{3.21}$$

The lowest value of the misfit R indicates the best solution form. As equation (3.19) is a linear equation, its least squares solution can be expressed as (Menke, 1984):

$$\boldsymbol{m^{est}} = (\boldsymbol{G^T W G})^{-1} \boldsymbol{G^T W u} \tag{3.22}$$

where the meanings of T and m^{est} were discussed in Section 3.1.2.1.

The weight matrix $\boldsymbol{W}$ plays a fundamental role in the inversion procedure: in fact, the volcanic seismic signals can be affected by disturbances of different types

(noise, site effects, instrumental problems, etc…) so as to have an amplitude able to mask the signal relative to the real source. Therefore, starting from an initial seismogram dataset registered by 3-component stations, the weight matrix can be used to eliminate the traces of one or more components to a station that is affected by this problem. This allows an inversion as much as possible linked to the signals relative to the real source. In my inversion of Mt. Etna data, based on visual observations, I have assigned zero weights to those components that showed instrumental problems (effectively excluding them), meanwhile I have given weight equal to one to the others.

Once the solution of the inverse process is evaluated, it is reasonable to assume that all the moment tensor components may have a common source-time function. For example, volcanic processes such as explosion can be represented by three equal force dipoles (diagonal elements of the moment tensor) or shear faulting can be described by the double-couple model, having the same time history. Consequently, equation 4.14 becomes:

$$u_n(\boldsymbol{x}, t) = G_{np,q} * M_{pq}^0 \cdot s(t) \tag{3.23}$$

where M_{pq}^0 represents the source mechanism (geometry) and *s(t)* is the source-time function. If we want to determine the source mechanism from the correspondent retrieved moment-tensor components, M^0 must be known.

Noisy data (i), uncertainties in velocity model (ii) or unmodelled nonlinear effects in the wave propagation (iii) can give rise to differences in time history of moment-tensor components. Vasco (1989) was able to find a temporal function that represented all the components of the moment tensor by performing the analysis of the principal components based on the decomposition of the singular value of the whole moment-tensor $M(t)$, succeeding in estimating its contribution to each component and so to each M^0 component. Defined M^0, it is possible to estimate different parameters to the source such as volumetric change, the relative

contribution of shear faulting vs. volumetric changes, the position of the fault plane (in the case of shear or tensile faulting), etc.

To define the source mechanism, the ratio of the components of diagonalized moment tensor is fundamental (Aki & Richards, 2002). To describe the moment tensor of a seismic source it may be useful to examine the cases of three sources called ISO, DC and CLVD, respectively.

If all the three diagonal terms of seismic moment tensor are non- zero and equal with same polarity as the first motion, we obtain a pure volumetric source, called ISO, which generally represents a volume change (**Fig. 3.10**), usually associated with explosions or implosions in volcanoes:

$$M = \begin{bmatrix} E & 0 & 0 \\ 0 & E & 0 \\ 0 & 0 & E \end{bmatrix} \tag{3.24}$$

The sum of the diagonal components will be equal to $3E$, where E is equal to $\lambda + \frac{2}{3}\mu$.

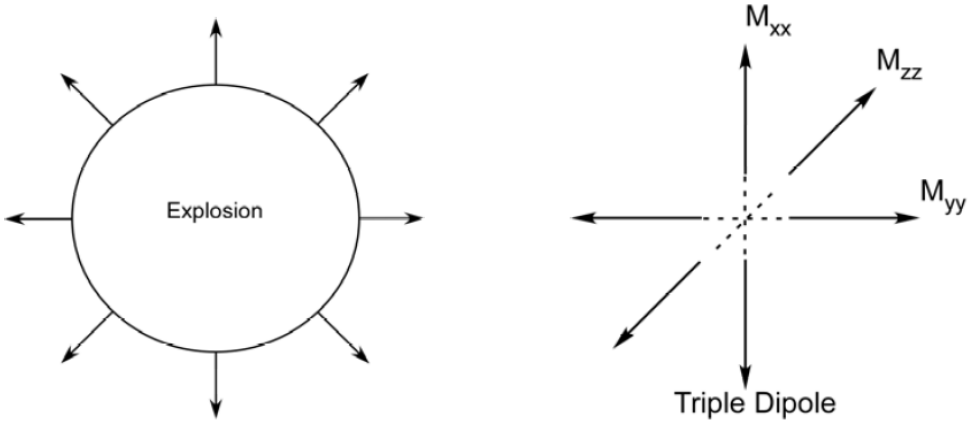

Figure 3.0.10. Representation of an explosive source using a triple dipole as equivalent body forces, (energy is equally radiated in all directions). Figure reproduced from Stein and Wysession (2003).

Faulting source mechanism, instead, are generally represented by double-couples, called DC. Considering left-lateral strike-slip motion in the ± y direction on a fault

in the $y - z$ plane (that is the same for a right-lateral movement on a fault in the $x - z$ plane) and if the magnitude is M_0 (**Fig. 3.11**), the moment tensor can be expressed as:

$$M = \begin{bmatrix} 0 & M_{xy} & 0 \\ M_{yx} & 0 & 0 \\ 0 & 0 & 0 \end{bmatrix} = M_0 \begin{bmatrix} 0 & 1 & 0 \\ 1 & 0 & 0 \\ 0 & 0 & 0 \end{bmatrix} \tag{3.25}$$

For a seismic source the Compensated Linear Vector Dipoles geometry consists in source characterized by a double-strength force couple along one axis, and unit-strength force couples in the direction of the two perpendicular directions (Lay and Wallace, 1995).

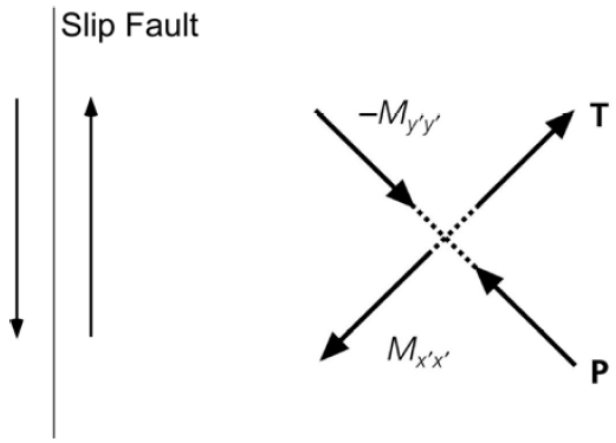

Figure 3.0.11. Representation of a slip fault using double couple as equivalent body forces. Figure reproduced from Stein and Wysession (2003).

For Compensated Linear Vector Dipoles source, called CLVD, the moment tensor can be expressed as

$$M = \begin{bmatrix} -\lambda & 0 & 0 \\ 0 & \lambda/2 & 0 \\ 0 & 0 & \lambda/2 \end{bmatrix} \tag{3.26}$$

This mechanism can be associated with an inflating magma dike which can be modelled as a crack opening under tension. For a crack, the moment tensor can be expressed as

$$M = \begin{bmatrix} \lambda & 0 & 0 \\ 0 & \lambda & 0 \\ 0 & 0 & \lambda + 2\mu \end{bmatrix} \tag{3.27}$$

while for a pipe the moment tensor can be expressed as

$$M = \begin{bmatrix} \lambda + \mu & 0 & 0 \\ 0 & \lambda + \mu & 0 \\ 0 & 0 & \lambda \end{bmatrix} \tag{3.28}$$

where λ and μ are the Lamé constant. Considering that $E = \lambda + \frac{2}{3}\mu$, the moment tensor in 4.27 can be decomposed in

$$\begin{bmatrix} \lambda & 0 & 0 \\ 0 & \lambda & 0 \\ 0 & 0 & \lambda + 2\mu \end{bmatrix} = \begin{bmatrix} E & 0 & 0 \\ 0 & E & 0 \\ 0 & 0 & E \end{bmatrix} + \begin{bmatrix} -2/3\mu & 0 & 0 \\ 0 & -2/3\mu & 0 \\ 0 & 0 & 4/3\mu \end{bmatrix} \tag{3.29}$$

Where, on the right-hand side, the first term is an isotropic tensor while the second term is a CLVD.

Also, two different double couple geometries with different moment, $\boldsymbol{M_0}$ e $\boldsymbol{2M_0}$, can generate CLVD source:

$$\begin{bmatrix} M_0 & 0 & 0 \\ 0 & 0 & 0 \\ 0 & 0 & -M_0 \end{bmatrix} = \begin{bmatrix} 0 & 0 & 0 \\ 0 & -2M_0 & 0 \\ 0 & 0 & 2M_0 \end{bmatrix} + \begin{bmatrix} M_0 & 0 & 0 \\ 0 & -2M_0 & 0 \\ 0 & 0 & M_0 \end{bmatrix} \tag{3.30}$$

Different decompositions of seismic moment tensor can reflect the same system of equivalent body forces with the same radiation pattern (**Fig. 3.12**).

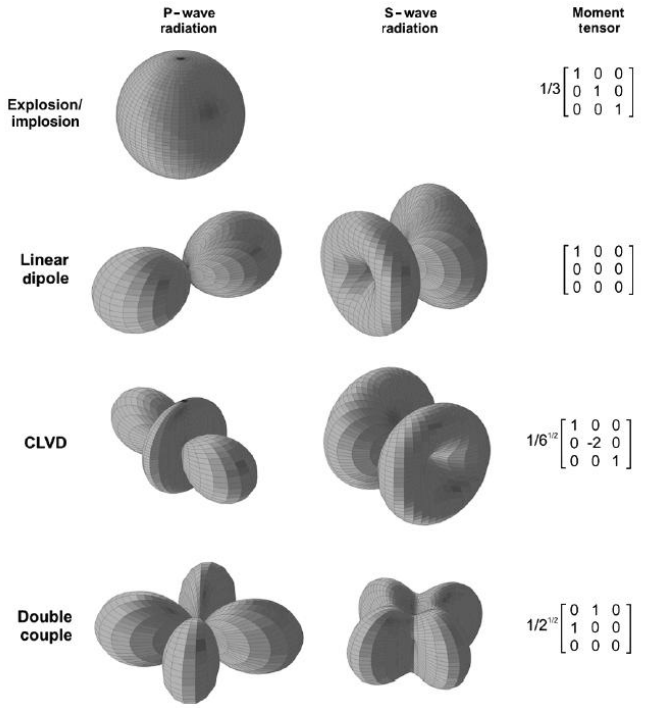

Figure 3.12. P-wave and S-wave radiation patterns and relative moment tensors for different seismic source types.

It follows that the moment tensor can be decomposed in different ways with different interpretations (Vavryčuk, 2001). Generally, the total moment tensor "$\boldsymbol{M_{TOT}}$" related to a seismic source, following Vavryčuk (2001, 2015) can be thought of as:

$$\boldsymbol{M_{TOT} = M_{ISO} + M_{DC} + M_{CLVD} = M_{ISO} + M_{DEVIATORIC}} \qquad (3.31)$$

The sum of $\boldsymbol{M_{ISO}}$ and $\boldsymbol{M_{CLVD}}$ represent the non-DC component of the moment tensor while the sum of $\boldsymbol{M_{DC}}$ and $\boldsymbol{M_{CLVD}}$ represent the deviatoric component of the moment tensor (hereafter indicated as M*).

In according with Vavryčuk (2001), the term of equation (3.31) can be expressed as

$$\boldsymbol{M_{ISO}} = \frac{1}{3} tr(\boldsymbol{M_0}) \begin{bmatrix} 1 & 0 & 0 \\ 0 & 1 & 0 \\ 0 & 0 & 1 \end{bmatrix} \qquad (3.32)$$

$$\boldsymbol{M_{CLVD}} = |\varepsilon| M^*_{|max|} \begin{bmatrix} -1 & 0 & 0 \\ 0 & -1 & 0 \\ 0 & 0 & 2 \end{bmatrix} \tag{3.33}$$

$$\boldsymbol{M_{DC}} = (1 - 2|\varepsilon|) M^*_{|max|} \begin{bmatrix} -1 & 0 & 0 \\ 0 & 0 & 0 \\ 0 & 0 & 1 \end{bmatrix} \tag{3.34}$$

where $M^*_{|min|}$ and $M^*_{|max|}$ are the minimum and maximum absolute values of the eigenvalues of the deviatoric moment **M***, respectively, and the parameter ε is the ratio value between these two eigenvalues, that defines the size of CLVD with respect to the size of DC (Julian et al., 1998):

$$\varepsilon = -\frac{M^*_{|min|}}{\left|M^*_{|max|}\right|} \tag{3.35}$$

where $\varepsilon = 0$ a pure DC, while $\varepsilon = \pm 0.5$ for a pure CLVD (positive for a tensile source and negative for compressive source). To compute the percentage (%) of each component relative to the others, Vavryčuk, (2001) proposed the follows formulas:

$$\%_{ISO} = \frac{1}{3} \frac{tr(M_0)}{\left|M^*_{|max|}\right|} 100\% \tag{3.36}$$

$$\%_{CLVD} = 2\varepsilon(100\% - |\%_{ISO}|) \tag{3.37}$$

$$\%_{DC} = 100\% - |\%_{ISO}| - |\%_{CLVD}| \tag{3.38}$$

The $\%_{DC}$ is always positive while $\%_{ISO}$ and $\%_{CLVD}$ are positive for a tensile source and negative for compressional source.

However, the exposed formulation does not consider the problems of the inversion process linked to the near-surface characteristics of the volcanic structures. In the case of LP events, while performing moment tensor inversions

of synthetic data, Bean et al (2008) observed that attention must be given to the inversions for those events located in the volcano edifices that do not have sufficient near-surface (few hundred meters) resolution, as in the case of Mt. Etna volcano. A possible solution to the problem can be considered the procedure illustrated by Nakano and Kumagai (2005) where waveforms are inverted for a set of pre-assumed possible source geometries. For the moment tensor inversion of volcanic tremor at Mt. Etna, the same principles for moment tensor inversions of LP events adopted by Lokmer et al. (2007) in the case of Stromboli (Italy) and Barros et al. (2011) in the case of Mt. Etna was followed. Therefore, in according to Nakano and Kumagai (2005), sets of equations can be used to express the Cartesian components of the moment tensor as functions of the azimuth angle φ and dip angle θ of the symmetry axis (crack normal or longitudinal axis for a pipe; see figure 3.13). For a crack, moment tensor components became:

$$\begin{aligned} M_{xx} &= M_0(\lambda/\mu + 2sin^2\theta cos^2\varphi) \\ M_{yy} &= M_0(\lambda/\mu + 2sin^2\theta sin^2\varphi) \\ M_{zz} &= M_0(\lambda/\mu + 2cos^2\theta) \\ M_{xy} &= M_0(sin^2\theta sin2\varphi) \\ M_{xz} &= M_0(sin2\theta cos\varphi) \\ M_{yz} &= M_0(sin2\theta sin\varphi) \end{aligned} \tag{3.39}$$

while for the pipe

$$\begin{aligned} M_{xx} &= M_0(\lambda/\mu + 2cos^2\theta cos^2\varphi + sin^2\varphi) \\ M_{yy} &= M_0(\lambda/\mu + 2cos^2\theta sin^2\varphi + cos^2\varphi) \\ M_{zz} &= M_0(\lambda/\mu + sin^2\theta) \\ M_{xy} &= -1/2\, M_0(sin^2\theta sin2\varphi) \\ M_{xz} &= -1/2\, M_0(sin2\theta cos\varphi) \\ M_{yz} &= -1/2\, M_0(sin2\theta sin\varphi) \end{aligned} \tag{3.40}$$

where M_0 represent the seismic moment, λ and μ are the Lamé's parameters, and x, y, and z refer to the east, north, and vertical upward directions, respectively. According to convention shown in **Fig. 3.13** and proposed by De Barros et al. (2011), φ and θ represent the azimuth and dip angles, respectively. In particular, azimuth φ is measured between 0° and 360° anticlockwise from east, while dip angles θ is defined between 0° and 90° from the upward direction.

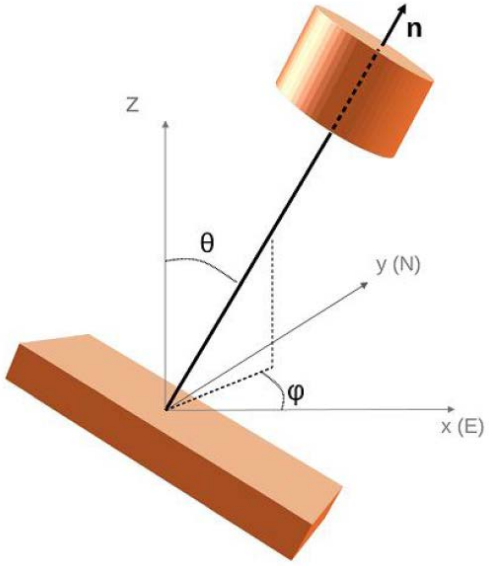

Figure 3.13. Coordinate system used to define crack and pipe orientation (De Barros et al., 2011).

Therefore, the inverse problem represented with equation 3.19 can be re-written as:

$$\boldsymbol{u} = \boldsymbol{G_M m_M}(\lambda/\mu, \theta, \varphi)M_0 + \boldsymbol{G_F m_F} \qquad (3.41)$$

where $\boldsymbol{G_M}$ are the Green's function associated with the moment tensor components and $\boldsymbol{m_M}$ is the vector containing the moment tensor component defined in the equations 3.39 and 3.40, instead $\boldsymbol{G_F}$ and $\boldsymbol{m_F}$ are the Green's functions and the source properties associated with the single forces, respectively. M_0 is the source time function in the frequency domain.

3.1.2.4 The medium function g(t)

As seen in paragraph 3.1.2.2 with the equation 3.13, the signals at seismic stations are the result of the convolution of different components. The function $g(t)$ describes the effect in the medium of seismic waves propagation and, to gain a full understanding of the source process, $g(t)$ it must be defined. Any function $g(t)$ can be defined and constructed as a linear combination of Green's Functions (Aki and Richard, 2002). The Green's functions can be described as the response of the medium to an impulse force acting at the source point, recorded at the receiver position, and, mathematically, can be expressed by a tensor source-receiver coordinate depending (Aki and Richards, 2002; Auger, 2006). Generally, the determination of the Green's function related to a medium is a problem that is investigated by a supposed high number of source points; in order to limit the calculation time, it is of fundamental the reciprocity theorem (Aki and Richards, 2002) which shows that if the position of the source and receiver are interchanged, the wavefield recorded in both positions will be the same. In this manner, it is possible to calculate Green's functions by using the seismic stations as the "source", and the points source volume defined below the summit crater area as "receivers", reducing significantly the number of computations.

The reciprocity theorem is expressed by the equation (in Aki and Richards, 2002):

$$G_{np}(\boldsymbol{r}, t_r, \boldsymbol{s}, t_s) = G_{pn}(\boldsymbol{s}, -t_s, \boldsymbol{r}, -t_r) \tag{3.42}$$

where $G_{np}(\boldsymbol{r}, t_r, \boldsymbol{s}, t_s)$ denotes the displacement in the n-th direction, recorded at position $\boldsymbol{r}$ and time t_r caused by an impulsive force acting in direction p applied at position $\boldsymbol{s}$ at time t_s. The equation 4.41 implies that this is equal to the displacement in the p-th direction when a force is acting in a direction n from a position $\boldsymbol{s}$ at time $-t_s$ to a position $\boldsymbol{r}$ at time $-t_r$; indicating $\boldsymbol{r}$ and $\boldsymbol{s}$ source and receiver positions respectively, the time-dependence of the Green's functions in equation 4.41 can be expressed by the time difference $t_r - t_s$ for $G_{np}(\boldsymbol{r}, t_r, \boldsymbol{s}, t_s)$, in other words the time needed for the wave radiated from the source at position

$\boldsymbol{s}$ to arrive at the receiver at position $\boldsymbol{r}$. If this time interval is equal to the time needed for the wave radiated from the "source" at position $\boldsymbol{r}$ to arrive at the "receiver" at position $\boldsymbol{s}$ by $-t_s + t_r$ for $G_{pn}(\boldsymbol{s}, -t_s, \boldsymbol{r}, -t_r)$, it allows us to interchange the source and receiver positions in our numerical simulations.

To calculate the Green's functions for a single point source, it is necessary to identify their spatial derivatives around the source position. Indicating Δq the vector with direction q and the length of a defined grid-step, spatial derivatives ($G_{np,q}(\boldsymbol{r}, \boldsymbol{s})$) can be extracted from the output of the simulation and are given by the central finite-difference derivatives:

$$G_{np,q}(\boldsymbol{r}, \boldsymbol{s}) = \frac{G_{np}(\boldsymbol{r}, \boldsymbol{s} + \Delta q) - G_{pn}(\boldsymbol{r}, \boldsymbol{s} - \Delta q)}{2\Delta q} \tag{3.43}$$

Using both the reciprocity theorem and three orthogonal point forces at the receiver location, it is possible to reduce the number of numerical calculations to three times the number of the receivers.

3.1.3 Distortion effects due to topography, heterogeneity and near surface velocity structure

For the moment tensor inversion of LP seismicity, the accuracy with which the Green's function are calculated is of fundamental importance to retrieve the source function correctly. For example, as highlighted by Barros et al. (2011), small amounts of noise in the Green's functions can result in large errors in the retrieved source mechanism.

For the first time, Johnson (1974) proposed a method for calculating Green's function based on the action of a point force of a homogeneous half-space.

This procedure was used in several studies to retrieve the focal and source mechanism at many volcanoes: Legrand et al. (2000) retrieved the focal mechanism of volcanic tremor at Aso volcano in Japan, while Ohminato et al.

(1998) and Kumagai et al. (2002) derived the source mechanisms of LPs recorded in Kilauea volcano (Hawaii).

In recent years, in order to reflect as closely as possible the real conditions of the studied volcanic environments, several authors have highlighted the role of effects such as those related to the topography and free surface, as well as considering increasingly complex velocity models of the medium for propagation of seismic waves.

Ohminato and Chouet (1997) highlighted the need to quantify the effect of topography in the interpretation of mechanisms at the source of LP events. The topography is one of the most pronounced discontinuities with which the waves interact and the seismometers are normally found on this surface (e.g. the free surface, Neuberg and Pointer, 2000). The interaction between the free surface and the wavefield is controlled by the seismic wavelength, stratigraphy and topography. This interaction can significantly mask the original seismo-volcanic signature, determining a response dependent on the frequency of the wavefield, on the stratigraphy and the free surface (Neuberg and Pointer, 2000).

Generally, volcanic seismic sources are very shallow, possibly embedded in low velocity layers and this condition causes the generation of surface waves that can dominate the seismic wavefield. Ripperger et al. (2003) at Merapi volcano (Indonesia) studied the distortion effects due to topography through numerical analysis. They show how the wavefield can be affected by the presence of steep topography using an isotropic point source and a finite difference scheme. Moreover, Ripperger et al. (2003) highlighted that distortion effects and surface waves generation are more pronounced where the topography is more accentuated. In addition, the scattering effects due to topography significantly increase at stations located far away from the source. The waves, propagating through volcanic edifices, sample the low velocity layers on their path to the stations. Therefore, in volcanic context it is very difficult to distinguish between the different arrival phases due to heterogeneity-topography interaction that can cause problems in differentiating the wave- types in the recorded seismogram

(Lokmer, 2008). For this reason, the classical methods of source locations are inoperative and ineffective. A clear example is provided by Chouet et al. (1997) at Stromboli volcano, where polarization analysis of explosions and tremor highlighted that direction of the seismic wave arrivals are not consistent with the crater location but correspond to structural and topographical features.

Usually alternative methods for the location of the volcanic seismic signals source are more effective than classical methodology. For example, at Arenal (Costa Rica) Metaxian et al. (2009) with numerical tests using full waveforms showed how the numerical output of the wavefield comprises a mixture of scattered waves (P, S and surface waves) due to the topography and the complex velocity model. The effects of the topography influence the source location which was reasonably well retrieved when the P-waves dominate the signal (e.g. close to the source). Therefore, this study has highlighted the need to consider topography in the calculation of Green's function in order to avoid misleading results.

Other errors in the Green's function computations can be induced by poorly detailed and/or inexactly velocity model of the medium, which can contaminate the seismic signals and mislocate the hypocenter as shown by Šileny and Hofstetter (2002) following a moment tensor inversion of the seismic signals generated by a calibration blast in the Dead Sea.

In volcanoes the heterogeneities are very complex features, due to the presence of different lithology (e.g. volcanic rocks, ash layer, etc.) with different mechanic behaviors. In addition, the complexity of dike and sill structures in the volcano edifice make difficult to obtain a detailed velocity model, the shallowest portion.

Bean et al. (2008) applied an analysis of moment tensor inversion of LPs recorded at Mt. Etna, with regard to the effect of near-surface velocity structure on LPs signals. For the seismic source located in a shallow position, the small distance between source-stations causes the creation of intertwined waves where the coda and the first arrivals are mixed. Hence it is not always possible to distinguish the path effect from the source ones in the seismograms. In particular, spurious single forces, misoriented source geometry and incorrect moment magnitude can be

caused by near-surface velocity structure (Bean et al., 2008). Analysis of LP signals recorded by stations in a vertical position away from the source represents a solution to this problem. Generally, these stations are less affected by path effects, while stations located on the flanks experience lengthening of the signals and scattering effects that strongly influence the recorded signals. Therefore, when a moment tensor inversion is performed station location is of fundamental importance. However, De Barros et al. (2011) showed that the solution of moment tensor inversion can be considered stable for the events recorded on Mt. Etna in 2008, by using several stations (a minimum of 10 stations) located near the sources.

3.1.4 The Green's function library for volcanic tremor on Mt. Etna

In order to perform the moment tensor inversion of LP seismicity is necessary to calculate the Green's functions able to explain the characteristics of the medium in which the seismic waves propagate. For this purpose, it is possible to use several numerical methods based on a wide range of techniques (such as finite difference, spectral elements, boundary elements). All these methods allow us to model the seismic wavefield, including complex topography and heterogeneities, the most dominant scatterers of wave propagation on volcanoes.

To perform the moment tensor inversion of volcanic tremor recorded on Mt. Etna during the lava fountaining episode of 5 August 2011, the same Green's functions library computed by Zuccarello (2015) for the analysis of LP seismicity at Mt. Etna volcano, were used. This library of Green's functions was obtained using the 3D discrete elastic lattice scheme (ELM O'Brien and Bean, 2004; ***Fig. 3.14***), which is suitable for simulating seismic waves propagation in complex media with topography. The ELM facilitates modelling the medium as an elastic medium, made up of particles, arranged on a cubic lattice and connected with 18 more particles by springs and a bond-bending force (O'Brien and Bean, 2004). This last

force term is proportional to the angle between adjacent particles (θ_{jik} in ***Fig. 3.14***) and allows the inclusion of a variable Poisson's ratio. In this model the authors incorporated the heterogeneity by changing the elastic spring constants on each spring.

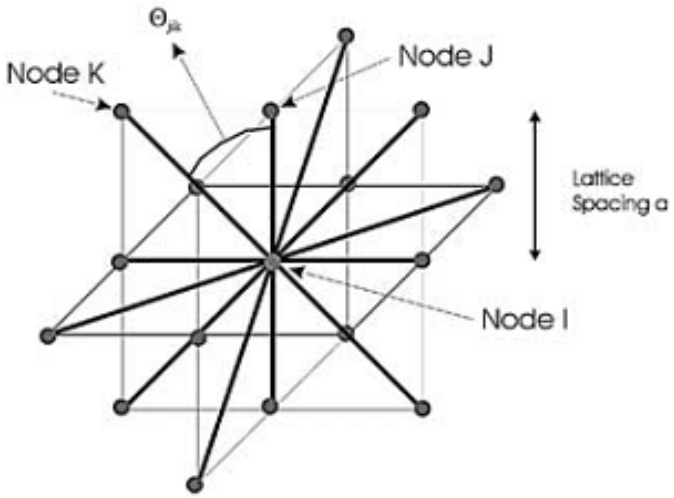

Figure 3.14. Cubic elastic scheme, taken from O'Brien and Bean (2004). Each dot represents the lattice node. Each node is connected to 18 more, by springs and a bond-bending force which is proportional to the angle between adjacent particles.

The Green's functions library was obtained with full wavefield numerical simulations, including the topography and considering a homogeneous medium. The methodology introduces the topography simply by removing all the nodes above the required free surface.

For numerical stability, the time step (dt) must be equal to:

$$dt < \frac{a}{V_{max}}$$

where a is the space between off diagonal node and V_{max} is the maximum compressional wave velocity.

Usually, for a moment-tensor inversion that includes six moment-tensor components and three single forces, nine simulations are required, if supposed that the source position is known exactly.

This gives 27 Green's functions at each seismic station for a single source position (9 simulations x 3 components of ground motion). For moment tensor inversion of volcanic tremor at Mt. Etna, the Green's functions, obtained for a number of sources contained in a defined volume containing the entire Mt. Etna edifice (about 58 x 55 x 30 km (East x North x elevation/depth), with a grid-step of 100 m), were used. For the same reason, a very large absorbing boundary of about 20 km was necessary to ensure the absorption of the longest wavelengths. The stability criterion of the numerical scheme required the time step of 0.03s.

For the moment tensor inversion of LP signals recorded at Mount Etna, several studies have shown how lower misfit of procedure are obtained for homogeneous medium velocity models that consider P-waves velocity of 1800-2000 m/s and V_P/V_S ratio of 1.73 (De Barros et al., 2009; 2011). These velocities are the same used in studies based on characterization of shallow magma pathway geometry at Mt. Etna (Patanè et al., 2008 and references therein) and tomographic survey (Monteiller et al., 2009). However, as suggested by Trovato et al. (2016), it is necessary to pay attention to this velocity model since the moment tensor inversion procedure tends to overestimate the real amplitude of the source time function.

The set of Green's functions, used in this study, were calculated by assuming P- and S-wave velocities values equal to 1800 m/s and 1000 m/s, respectively. It should be noted how this is the same velocity model used in this work in order to locate the volcanic tremor source during lava fountaining episode.

3.1.5 Location of volcanic tremor source

The location of the seismic source plays a fundamental role in the procedure of the moment tensor inversion. The location of volcanic tremor source cannot be performed with traditional methods: in fact, unlike earthquake's location where the focal coordinates are calculated from the arrival times of well identifiable seismic phases, the non-impulsive signature of tremor entails alternative location methods (Di Grazia et al., 2006).

Considering the need to reduce the source at one point for the moment tensor inversion analysis, for this study the location of the tremor source was carried out in two steps: first, (i) the volume of probable sources of the volcanic tremor was identified, while subsequently (ii) the best solution for the source contained in the detected volume was identified. For the first step, the method of amplitude decay of seismic signals was applied (e.g. Di Grazia et al., 2006), usually used for the near real-time location of the volcanic tremor at Mt. Etna. This analysis is based on a grid search method that allows to individuate the centroid of volcanic tremor, a volume inside which the source of the corresponding seismic signal can be identified; for details, see section 1.3.

Concerning the second step, a grid search procedure was again performed on the volume identified in the first step. In particular, a moment tensor grid search is performed in order to retrieve the waveform misfit values (R, see equation 3.20) for each point of the source volume and for the solutions considering only moment tensor (MT) and moment tensor plus single forces (MT + SF). The lowest misfit is considered the best estimation.

3.2 MOMENT TENSOR INVERSION OF MT. ETNA VOLCANIC TREMOR DATA OF 5 AUGUST 2011 LAVA FOUNTAINING EVENT

3.2.1 Introduction

As already described in paragraph 1.3.3, the volcanic activity at the summit craters of Mt. Etna during 2011-12 was quite intense and characterized by 25 episodes of lava fountains. In particular, the activity was more intense during July-August 2011: in fact, between July and August there were 8 lava fountain events at the New South East Crater (NSEC).

In order to understand the characteristics of the volcanic tremor source during the episodes of lava fountain, the eruptive episode, that took place on 5 August 2011, was taken into account. This episode of lava fountain lasted about 2 hours, developing from 21:00 to 23:00 GMT (Behncke et al., 2014); similar to the other events that took place in the period 2011-2012, the episode is framed within a paroxysmal event in which the fountain was preceded and followed by several hours of Strombolian activity, for a total of 8 h 15 min of activities (from 16:00 GMT on 5 August to 00:15 GMT on 6 August).

The **Fig. 3.15** shows the seismic signal recorded by vertical component of the ESLN station belonging to the seismic monitoring network managed by the INGV-OE.

Since the seismic RMS depends not only on volcanic tremor but also on amplitude transients (LP events, volcano-tectonic earthquakes, regional earthquakes, and so on), to consider only contribution of the tremor of seismic signals recorded by instruments, it was necessary to focus the attention on a specific range of frequencies. For the choice of the frequency band to be used I considered both the characteristic frequency of the tremor at Mt. Etna, but also the need to limit distortion effects two to topography, heterogeneity and near surface velocity structure discussed in section 3.1.3 in order to perform a reliable analysis of moment tensor inversion. Therefore, I decided to consider the seismic signals recorded at the different stations in the band of frequencies 0.2 - 0.5 Hz.

Specifically, I used this frequencies band both to localize volcanic tremor source and for the moment tensor inversion.

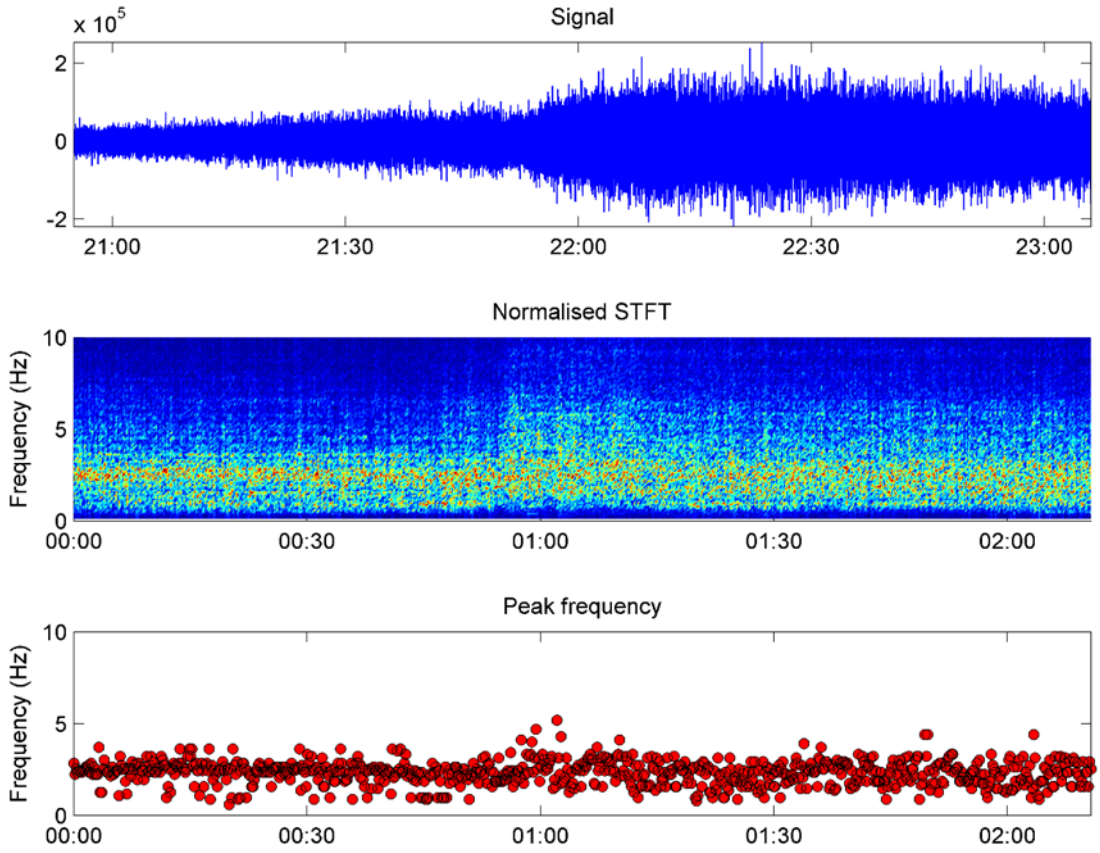

Figure 3.15. Lava fountaining at Mt. Etna of 5 August 2011. (**above**) Seismic signal recorded at vertical component of ECPN station during 2-hour long episode, and spectral analysis with results of Normalised Short Time Fourier Transform (**center**) and peak frequency (**bottom**) of seismic signal considered.

3.2.2 The paroxysmal event of 5 August 2011 event at Mt. Etna

For the description of the 9th paroxysmal event at Mt. Etna during 2011 I referred to the "Bollettino settimanale sul monitoraggio vulcanico, geochimico e sismico del vulcano Etna, 01/08/2011 - 07/08/2011 – INGV, Rep. 32/2011".

In the afternoon of Friday 5 August, the resumption of Strombolian activity at the NSEC signaled the possible occurrence of a new episode of lava fountain. Unlike previous episodes during 2011, on this occasion the paroxysmal phase of lava fountain was not preceded by a few days of Strombolian activity: in fact, the explosions near the cone increased in intensity and frequency within a few hours, accompanied by a marked increase in volcanic tremor.

The first intracraterical explosions were detected by the Montagnola thermal camera at around 17:00 GMT on 5 August. After 20:15 GMT a lava flow formed which started to spread on the eastern flank of the cone. After 20:30 GMT Strombolian activity has become almost continuous.

Shortly before 21:00 GMT, the explosive activity began to produce an almost continuous fountain, with magma jets up to about 100 m above the crater rim. A significant increase in the fountaining activity occurred after 21:30 GMT; the lava fountains have gradually grown to reach an estimated height between 400 and 500 m around 22:00 GMT, with the maximum peak amplitude of volcanic tremor recorded around 22:15 GMT. After 22:15 GMT, the explosive activity gradually decreased until 23:00 GMT and the magma jets began to drop strongly in height. The explosive activity was exhausted from 00:15 GMT on 6 August.

Observed from Monte Fontane, the lava flow was quite sustained; descending into the upper Valle del Bove, the front of the main branch had been subdivided into some secondary lava flows.

Around 24:00 GMT the lava flow was cooling, while only the main lava flows were advancing by gravitational sliding for a few tens of meters.

3.2.3 The influence of microseism

As described in the previous paragraph, in order to limit the distortion effects due to topography, heterogeneity and near surface velocity structure, it was chosen to perform MTI analysis of the volcanic tremor considering the low frequency band

0.2 – 0.5 Hz. Due to selected frequency band, before proceeding with the different steps of localization and inversion of the moment tensor of the tremor source, it was necessary to take into account the contribution of the microseism activity.

In addition to typical signals of volcanic activity such as volcanic tremor, the seismic signals continuously recorded by the broadband stations of the seismic network at Mt. Etna are affected by "noise" sources such as anthropic activity, storms and sea waves. The most continuous seismic signal on Earth is microseisms, mainly composed of surface waves and closely related to ocean wave energy coupling with the Earth's motion (e.g.: Cannata et al., 2017, and references therein). Two types of microseisms are generally distinguished: primary and secondary. The former is generated by direct ocean waves in the shallow seafloor interacting with the sloping seafloor, by breaking or shoaling. This seismic signal has the same period as the generating ocean waves (10-20 s; Hasselmann, 1963). Secondary microseisms are more energetic and are generated by standing or colliding waves within the ocean wave field near the coast or in the deep ocean and have shorter periods (3-10 s; Grob et al. 2011, and references therein). Finally, there is an even shorter period microseism, characterized by period shorter than 5 s and called Short Period Secondary Microseism, whose source is mainly associated to the local sea state and winds (e.g. Bromirski et al., 2005; Chen et al., 2011).

Recent studies, that took into account non-eruptive periods at Mt. Etna and were based on spectral analysis of seismic signals have highlighted low-frequency peaks attributable to microseismic activity (e.g.: Monna et al. 2004; Cabras et al., 2010; De Caro et al., 2014). In particular, De Caro et al. (2014) have highlighted two different peaks for secondary microseism: the first one is found at about 0.085–0.200 Hz and was generated in open seas when favorable weather conditions produce opposing swell and excited near-coastal areas. The second peak, instead, is found at 0.2 – 0.5 Hz and it is associated with waves induced by local winds. Moreover, De Caro et al. (2014) compared the local wind speed recorded by meteorological station located in Catania with the spectrogram computed on the

vertical seismic component at a deep-sea cabled observatory during the winter time. They observe a strong relationship between the increase in wind speed and the increase in energy levels of the second frequency peak. Similar peaks at the same frequencies were observed by Cabras et al. (2010); in this case, they justified these peaks as attributable to the local surface sea wind speed greater than 7.98 m/s, in agreement with the analysis proposed by Kadota and Labianca (1981).

In order to evaluate the effects of microseism activity on the signals recorded during 5 August 2011 lava fountaining episode taken into consideration for the MTI analysis, a comparison was performed among the following time series (**Fig. 3.16**): RMS amplitude at different frequency band of seismic signal recorded at the EPOZ station, belonging to the seismic monitoring network managed by *INGV-OE* and, thanks to its location close to the Ionian coast, strongly affected by the microseism sources; local wind speed recorded by the Catania station of the *Rete Mareografica Nazionale (RMN) - ISPRA* (http://www.mareografico.it); Significant Wave Height recorded by the Catania buoy of *Rete Ondametrica Nazionale (RON) – ISPRA* (http://www.telemisura.it).

By taking into account the data of the whole 2011, it is evident that both local wind speed and Significant Wave Height showed low values during 5 August 2011 (**Figs. 3.16 and 3.17**). In addition, the RMS amplitude of the seismic signals of EPOZ, filtered in low frequency bands (0.05 – 0.0769 Hz, 0.1 – 0.2 Hz and 0.2 – 0.4 Hz) reflecting the amplitude of the microseism, exhibits low values during the same day (**Fig. 3.16**).

On the basis of these observations, it is possible to consider the contribution of microseism on the signal, recorded at Mt. Etna during the considered lava fountaining episode, negligible and/or absent with respect to the volcanic tremor contribution. This is also strongly supported by the fact that the intense explosive activity of 5 August 2011 was accompanied by sharp increases in the volcanic tremor amplitudes. Therefore, it is reasonable to suppose that the MTI analysis in the considered frequency band was not significantly affected by microseism noise

and that the seismic signals recorded during the lava fountaining episode depend only on the volcanic tremor.

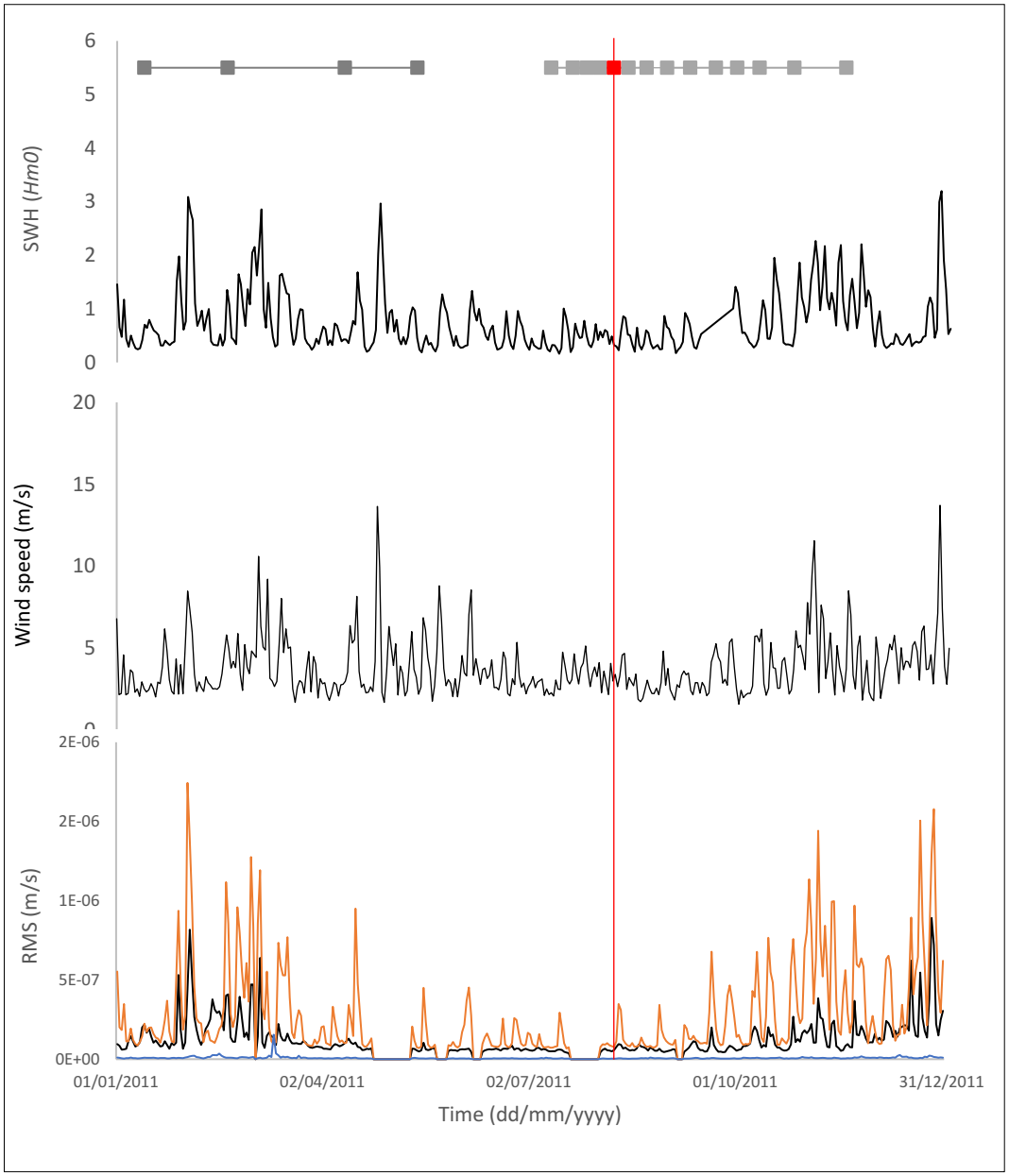

Figure 3.16. Comparison between among different time series, obtained for the whole 2011 and characterized by daily data. **a**. Significant Wave Height at Catania buoy (by RON-ISPRA). **b**. Local speed wind at Catania meteorological station (RMN-ISPRA). **c**. RMS amplitude of seismic signal recorded at vertical component of EPOZ station, filtered at low-frequencies band (0.05 – 0.0769 Hz: blue line; 0.1 – 0.2 Hz: black line; 0.2 – 0.4 Hz: red line). The top gray continuous lines and square markers represent periods of eruptive activity and lava fountains, respectively. The red vertical line with the top red square marks the occurrence of 5 August 2011 lava fountaining.

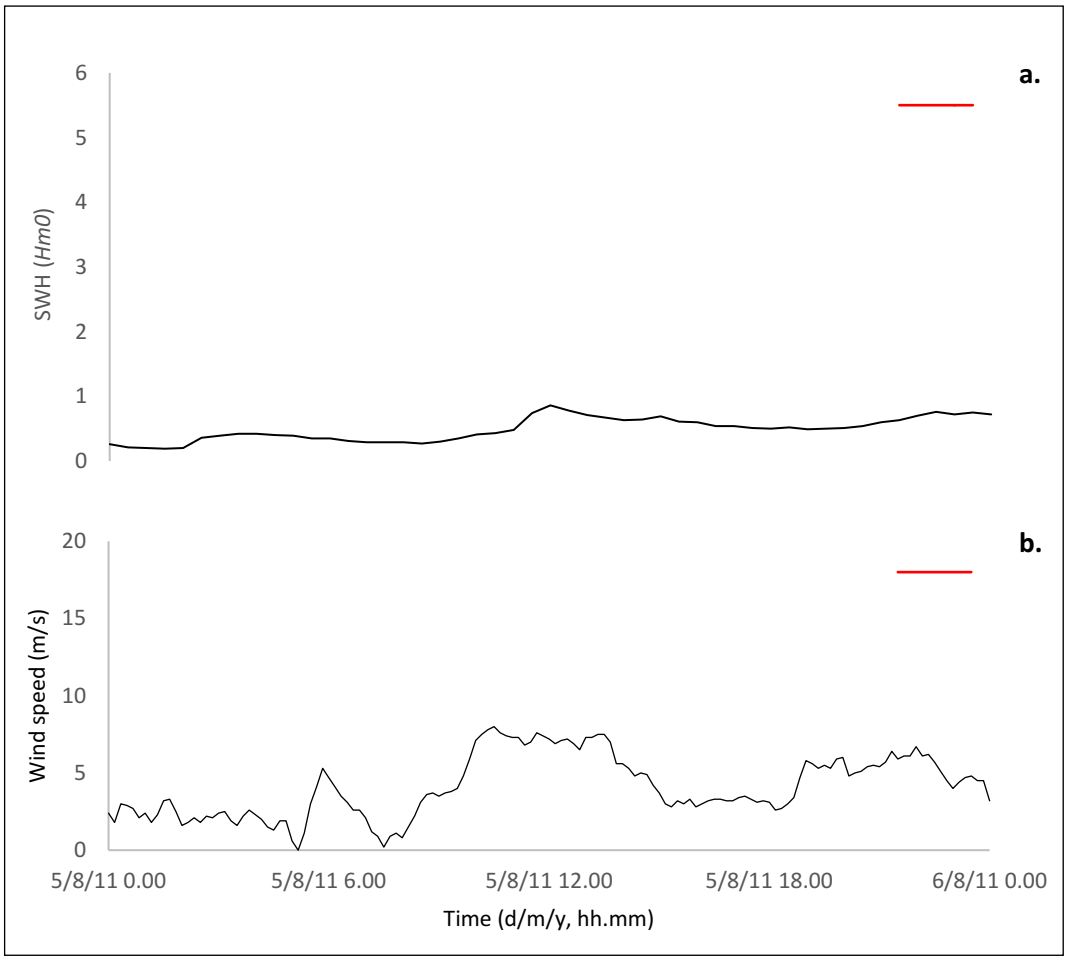

Figure 3.17. Comparison between time series, obtained for 5 August 2011 and characterized by hourly data. **a**. Significant Wave Height at Catania buoy (by RON-ISPRA). **b**. Local speed wind at Catania station (RMN-ISPRA). Red thick continuous lines represent the time interval when lava fountaining occurred.

3.2.4 Location of volcanic tremor

The source location of the seismic signal recorded in volcanic areas is the first important task for carrying out a reliable moment tensor inversion. Hence, it is necessary to define a volume within which to find the best solution for the seismic signal source. For this purpose, for the volcanic tremor recorded during the lava fountain of 5 August, the amplitude decay method, usually used at Mt. Etna to monitor the temporal variations of the tremor in terms of amplitude and source location, was applied.

For the location of volcanic tremor source, the same initial configuration of 3-component broadband seismic stations (**Fig. 3.18**), used for the calculation of the library of Green functions to which it was used with this study (for details see section 3.2.3), was utilized.

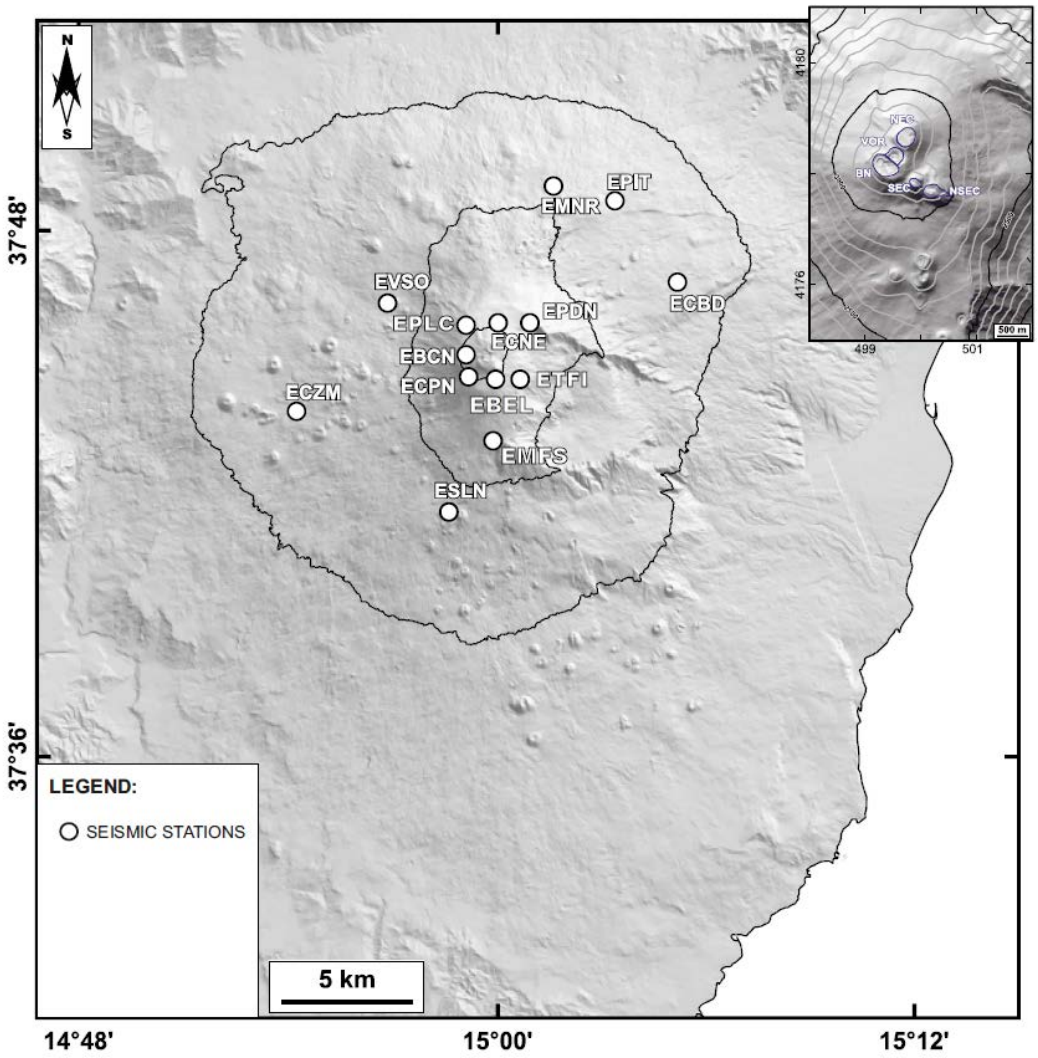

Figure 3.18. Digital elevation model of Mt. Etna with the location of 3-component seismic stations used to study volcanic tremor source.

Specifically, the temporal variations of the tremor were investigated, in terms of source localization between 21:00 GMT and 23:00 GMT, time interval when the lava fountain occurred on 5 August with peak of amplitude of the tremor at 22:15 GMT.

As for the centroids of the volcanic tremor source, the RMS amplitudes were computed. Since the seismic RMS depends not only on volcanic tremor but also on amplitude transients (LP events, volcano-tectonic earthquakes, regional earthquakes, and so on), the 25° percentile on 60 s-long moving windows of RMS was calculated to exclude the contributions of amplitude transients and highlight the variations exclusively related to volcanic tremor changes.

The volcanic tremor source was located within 10-minutes-long sliding time windows, filtered in 0.2 – 0.5 Hz low frequency band. The variations in time and space of the volcanic tremor centroid locations are given in **Fig. 3.19**.

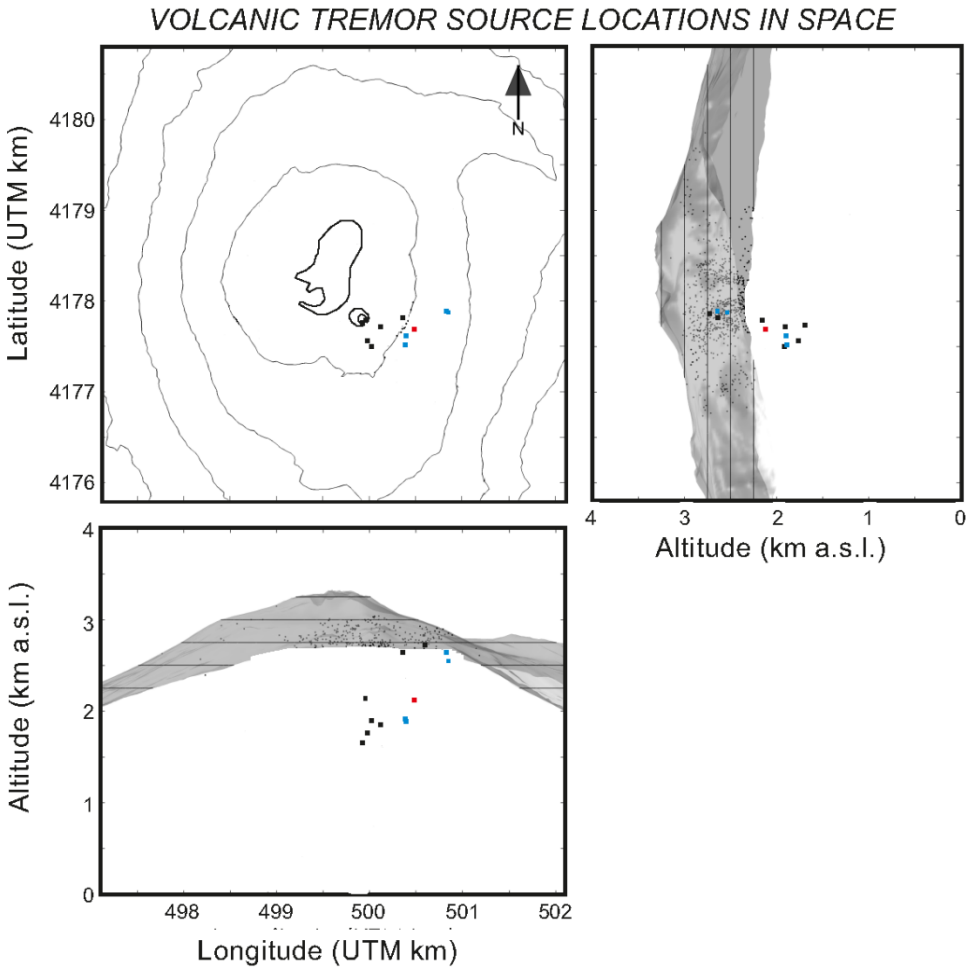

Figure 3.19. Volcanic tremor source location during 5 August lava fountaining at Mt. Etna, considering 10-minutes-long sliding time windows and 0.2 – 0.5 frequency band. Red dot represents the location during the peak amplitude, while black and blue dots represent locations pre- and post- peak amplitude phases, respectively.

The calculated volcanic tremor centroids are located below NSEC area at shallow depths (> 1.5 km a.s.l.). **Tab. 3.1** shows the errors associated with the location of the tremor during peak amplitude phase, calculated following the Jackknife's technique.

Error in volcanic tremor location		
Latitude (km)	Longitude (km)	Depth (km)
0.575	0.519	0.963

Table 3.1. Location of volcanic tremor source during the peak amplitude phase.

3.2.5 Volcanic tremor source inversion

As discussed previously, the source mechanisms associated with volcanic seismic events are generally derived by using a moment tensor inversion. For this reason, a moment tensor inversion of the volcanic tremor recorded at Mt. Etna is performed in order to (i) retrieve the seismic source mechanisms generating this type of signal during lava fountaining phases and (ii) gain a better understanding of Mt. Etna's shallower plumbing system.

Moment Tensor Inversion (MTI) analysis has been successfully applied in a wide range of volcanoes around the world (e.g., Ohminato et al., 1998; Chouet et al., 2003, 2008; Nakano et al., 2003; Kumagai et al., 2005; Davi et al., 2010; De Barros et al., 2009; 2011) in order to understand source mechanisms of seismic signals associated with LP events. MTI analysis, on the other hand, was rarely applied to volcanic tremor (e.g. Davi et al, 2012). As regards Mt. Etna, this study represents the first case in which MTI analysis is applied to volcanic tremor.

The inclusion of Single Forces (F) in the inversion procedure makes the recovery of the source mechanism an even more complicated task. However, single forces may be common in volcanic environments and have been modelled in other seismic source studies.

In order to retrieve a correct moment tensor inversion, it was necessary to start from a correct source location of volcanic tremor recorded during lava fountaining of 5 August. For this purpose, the Green's functions calculated by Zuccarello (2015) at 11 stations of the seismic broadband permanent network were used. Such Green's functions were calculated by the three-dimensional discrete elastic lattice method, using ~1.8 km/s and ~1.0 km/s for P- and S-waves velocity, respectively, and assuming that the seismic wave propagation occurred in a homogeneous medium, taking into account that by Ohminato et al. (1998) and Chouet et al. (2003) as demonstrated that the long wavelengths are usually considered insensitive to small-scale heterogeneities. The same velocity model was used by De Barros et al. (2011) obtaining the best results for the MTI analysis of LP events recorded at Mt. Etna during the 2008 activity. In particular, the inversion procedure was performed using synthetic signals generated in the same volume constrained by the location of the tremor source (see section 3.2.4).

Therefore, due to the high processing times, it was decided neither to carry out new synthetic tests nor to calculate new Green's Functions, either because no new velocity model for Mt. Etna has been proposed and for the robustness of the ELM available.

To highlight variations of source mechanisms of volcanic tremor during the lava fountaining episode, the seismic signals recorded during the paroxysmal phase were divided into 100-sec-long time windows with 40-sec overlap, thus considering a total of 120-time windows of signals. The source location was assumed to be fixed in the whole considered time period, and equal to the one found during peak phase of the episode. This assumption was made also considering both the limits that characterize the velocity model, and the high degree of overlap characterizing the centroids of the tremor during lava fountaining obtained as seen in section 3.2.4.

Hence, once the volcanic tremor centroid was fixed, the moment tensor inversions were performed in the surrounding 630 grid points. The considered volume takes into account the location error (section 3.2.4). By comparing the results obtained

by both Moments Tensor plus Single Forces (MT + F) and only Moments Tensor (MT), it is possible to highlight how lower misfit values are obtained in the first case. In **Fig. 3.20** the distribution of these inversions is reported in terms of misfit between synthetics and real signals when MT + F are considered.

For 5 August lava fountaining episode, the volcanic tremor source positions are located in the grid points where the minimum misfit values were obtained considering time window between 22:14:10 – 22:15:50 GMT (when peak in RMS amplitude of volcanic tremor during lava fountaining are detected), that is: 4177.7 (km UTM Lat) – 500.35 (km UTM Long) – 2.95 (km depth a.s.l., at an altitude 200 m lower than the surface of the volcanic edifice) (**Fig. 3.20**). It is important to highlight that the minimum misfit for the considered time window was not obtained in the same node that was obtained by the amplitude decay method, but in a nearby node, however contained within the volume identified with the error associated with the source position (see section 3.2.4).

The data of each time windows were inverted to determine the moment tensor, and hence the misfit values, using the seismic signals recorded by 27 components of 11 stations with the best azimuthal distribution. As described by Lokmer et al. (2007) and De Barros et al. (2011) in their LPs inversion analysis, the stations closest to the source help constrain the source time function, while the others can be used to determine the mechanism. In particular, De Barros et al. (2011) showed that for stations close to the source, LP waveforms are not severely distorted by propagation effects, which stabilizes the Source Time Function (STF) reconstruction. Finally, the GFs are computed for the position found as described in Section 3.1.2.

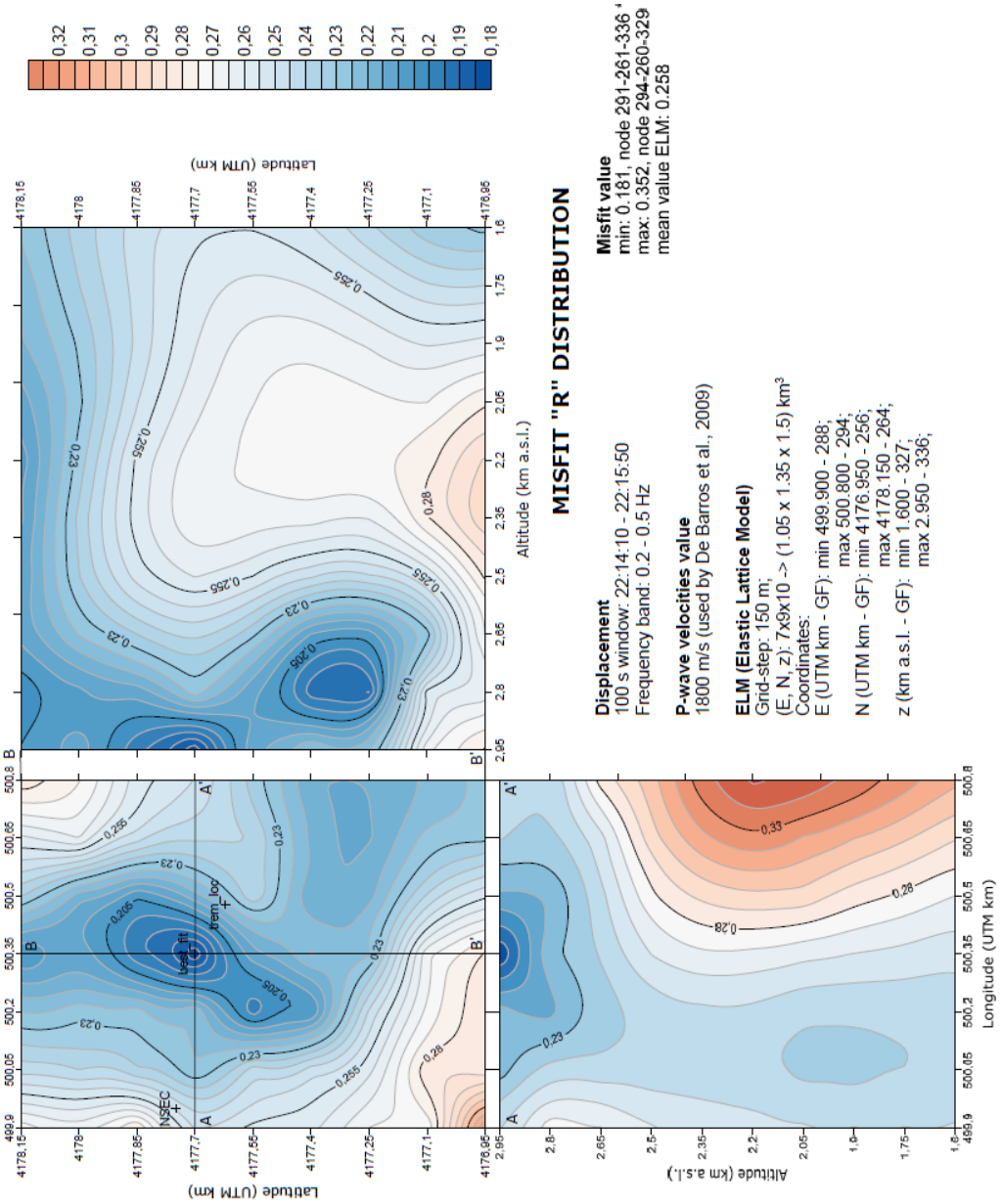

Figure 3.20. Distribution of misfit at nodes of ELM considering MT + F solutions for volcanic tremor source during max peak amplitude of seismic signals for 05 August lava fountaining episode. "*Best-fit*" represent the node with lower value of misfit that we fixed such as the source of volcanic tremor for MTI analysis. "trem_loc", instead, represent source position of volcanic tremor by amplitude decay method for the same time window. Finally, "NSEC" represent the position of New South-East Cone.

Once the source points and the velocity model are determined, the MTI for each available time windows were performed. A problem in the inversion procedure is

the use of single forces. In the case of mismodeling and mislocation, moment tensor inversions do not allow single forces to be properly reconstructed. However, De Barros et al. (2011) used the single forces to compensate for the errors coming from the velocity model and the source location. In the study presented here, the solutions obtained through MT and MT plus F were compared by calculating the Akaike Information Criterion (AIC) (Akaike, 1974). The interpretation of the solutions can be delicate, as the extraction of a single STF and the decomposition of the moment tensor components can be ambiguous and imprecise. To overcome this problem both Chouet et al. (2005) and Kumagai et al. (2005) proceeded first by determining a rough approximation of the mechanism using an unconstrained inversion, and then refining the source characteristics by constraining the inversion. A similar approach, proceeding in two steps: (i) I inverted for an unconstrained solution in order to determine the most reliable mechanism type (i.e., crack, pipe, or explosion) and (ii) I used results of step (i) to perform a constrained inversion.

For each time available window of volcanic tremor, the unconstrained inversion was carried out with and without single forces, and the Source Time Function (STF) were reconstructed. **Fig. 3.21** shows the STFs relating to the peak activity detected during 5 August lava fountaining episode.

The misfit value (misfit = 0.1889) is considerably lower when forces are considered. In this case the single forces, whether physical or an artifact, do not change the moment tensor solution.

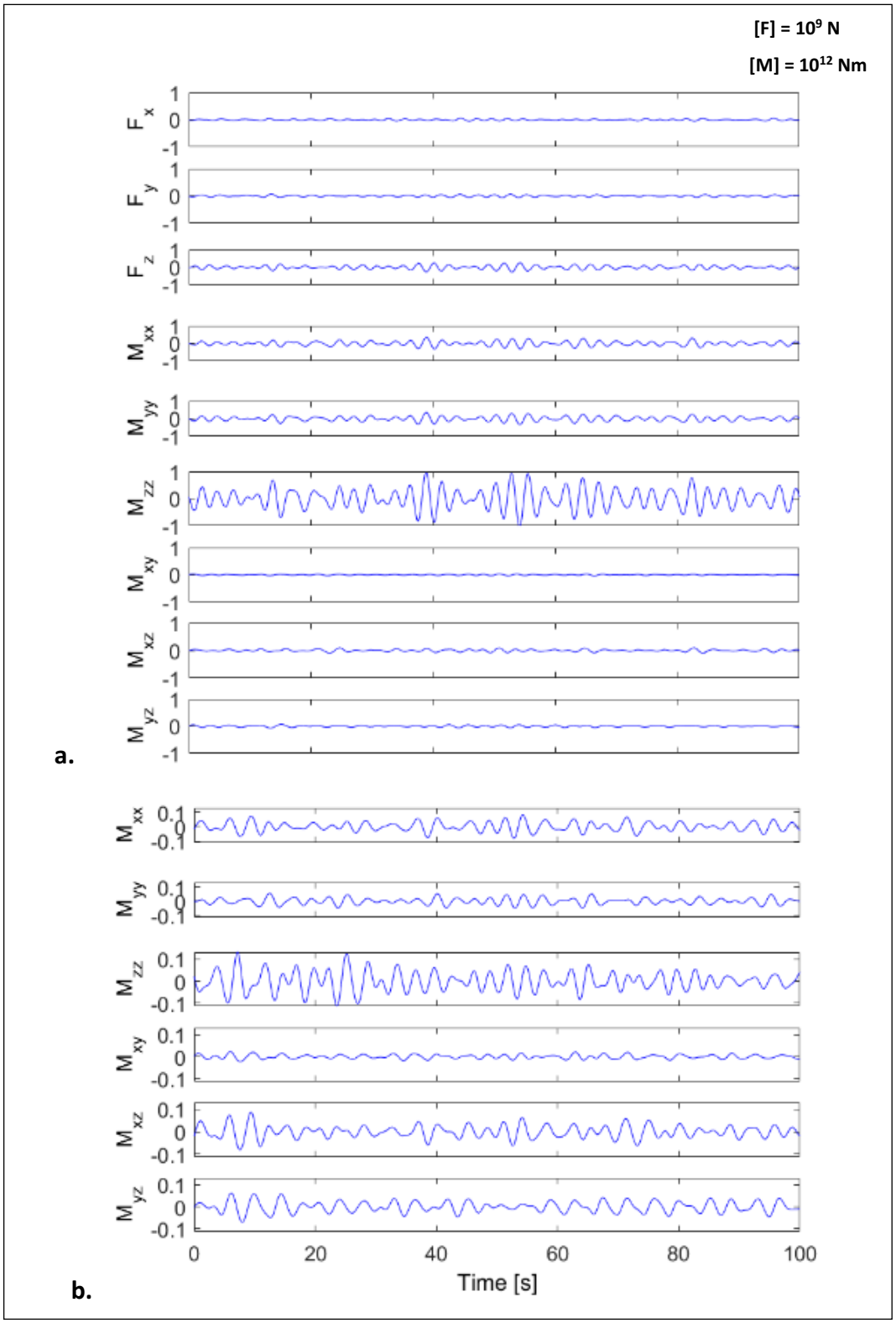

Figure 3.21. Moment Tensor Inversion results for volcanic tremor at Mt. Etna recorded during 22:14:10 – 22:15:50 GMT of 05 August 2011: source time function obtained by the unconstrained inversion considering (**a**) Moment Tensor + Single Forces (MT+F) and (**b**) Moment Tensor only (MT).

The waveform fit between original signals and synthetic seismograms are very good for most of the stations that are very close to the source position (**Fig. 3.22**).

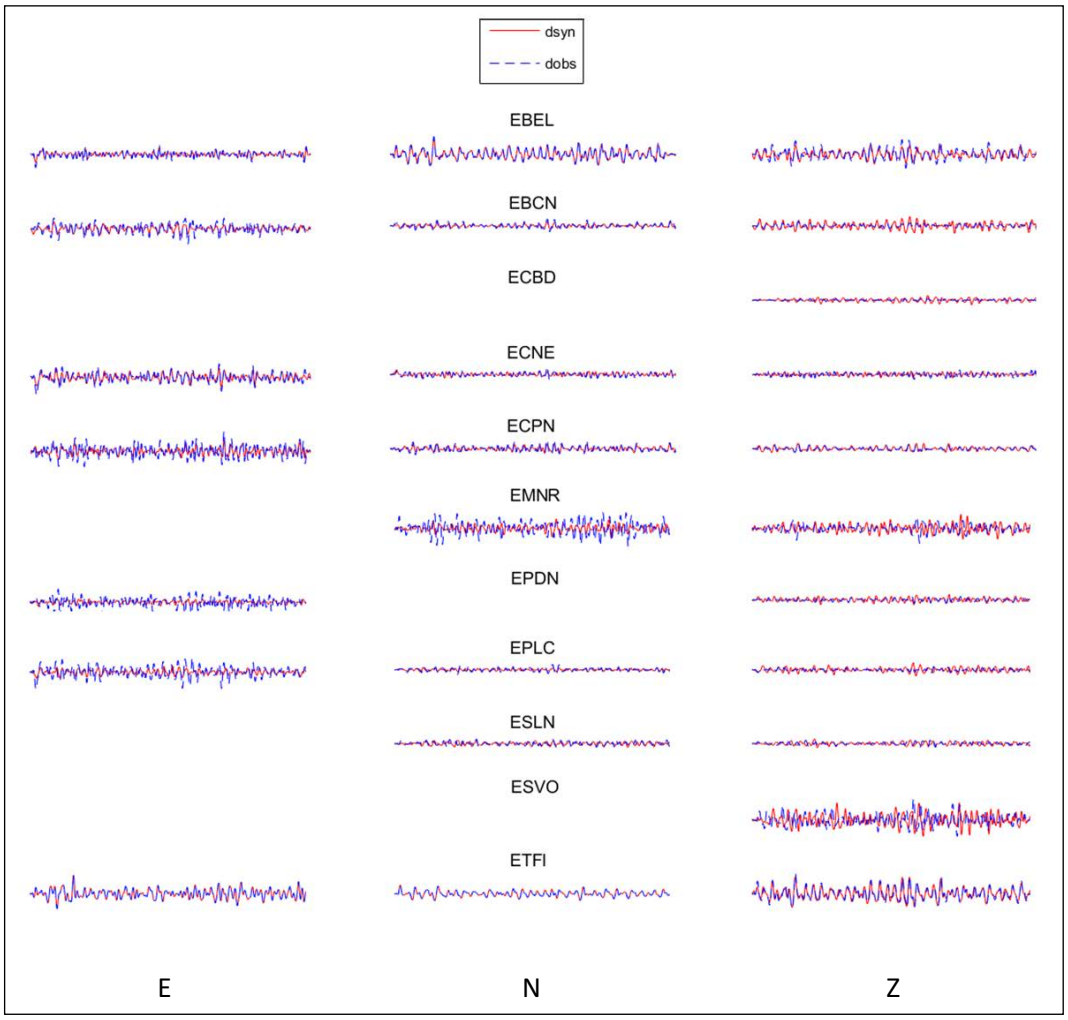

Figure 3.22. Waveform (displacement) fit between the data (continuous lines) and the synthetic seismograms (dashed lines) for the volcanic tremor at Mt. Etna recorded during time interval of 22:14:10 – 22:15:50 GMT of 05 August 2011.

The fits worsen for stations farther from the crater area, with lower amplitude signals due to the lower signal-to-noise ratio, but not for all the components. Successively, in according to Vasco (1989), the eigenvectors of the moment tensor solutions were calculated by using the principal components analysis.

This method is based on the evaluation of the singular values of the whole set of STFs, allowing the estimation of a common STF and its contribution to each component, namely the scalar moment tensor.

The moment tensor components can be written as a linear combination of a set of basic functions that can be expressed by the following equation:

$$M^T = U\lambda V^T \tag{3.44}$$

where "T" indicates the transpose matrix of the moment tensor components M, and of eigenvectors of the model parameters (V), respectively; U, instead, is the eigenvectors matrix of the data and λ the singular values matrix.

One of the main advantages of the singular values is that they act as weighting factors of the source basic functions. This means that by decomposing the solutions and finding one large singular value compared to the others, the associated source function can be considered the right one (Vasco, 1989).

Generally, the singular values are also arranged in a matrix format with a decreasing order, with the first representing the largest one. Micro-seismic noise or source complexity can increase the non-uniqueness of the solutions. In the end, the eigenvalues of the 3 × 3 scalar moment tensor give the mechanism and its eigenvectors yield the orientation of the principal axes. The solution can then be decomposed into the percentage of ISO, CLVD and DC (Vavrycuk, 2001). This last step, the decomposition, is, however, non-unique and unstable.

After having carried out these last two analyses, I found that the volcanic tremor source, during the maximum seismic amplitude phase of 5 August lava fountaining episode, shows a similar mechanism to that of a crack, with eigenvalues with nearly 56 % isotropic component, while deviatoric component shows the normal axis oriented with azimuth φ ≈ 320° and dip θ ≈ 5° (φ and θ angles defined in accordance with De Barros et al., 2011, as seen in Section 3.1.2.3 with **Fig. 3.13**). This behavior is also shown by the pattern of the eigenvalues, with a longer axis and two smaller ones (**Fig. 3.23**).

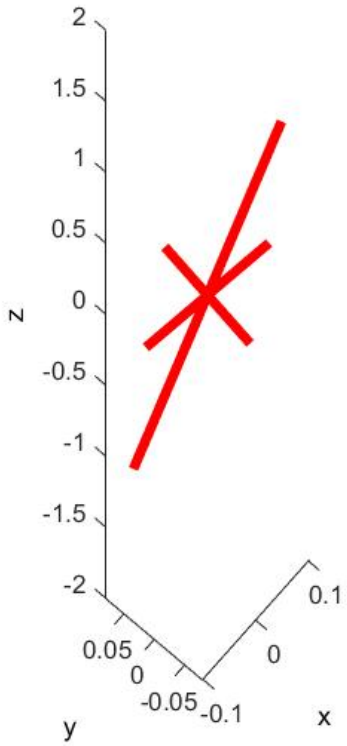

Figure 3.23. Eigenvectors obtained from the MT+F unconstrained inversion solutions for the volcanic tremor at Mt. Etna recorded during the time interval of 22:14:10 – 22:15:50 GMT on 05 August 2011. Eigenvectors are sampled every 0.03 s (x = E-W, positive towards the East; y = N-S, positive towards the Nord; z = U-D, positive towards the Up).

For the other 100-second-longs windows of the volcanic tremor recorded during the lava fountain episode of 5 August 2011, similar results were obtained. Results of the decomposition for the inversion of all tremor windows are shown in **Fig. 3.24** only for MT+F solutions. For each window of signal, a stable isotropic percentage (ISO%) was found: the ISO% varies from 54% to 59% with a small standard deviation in the order of the 1.04% from the mean value (56.94 %). Similarly to ISO component, the CLVD and DC components show a stable solution during the considered lava fountain. The CLVD% varies from 37% to 45% and shows a small standard deviation of 1.61% from the mean value (40.37 %). The DC%, instead, varies from 0% to 5% and shows a small standard deviation of 0.91% from the mean value (2.70 %).

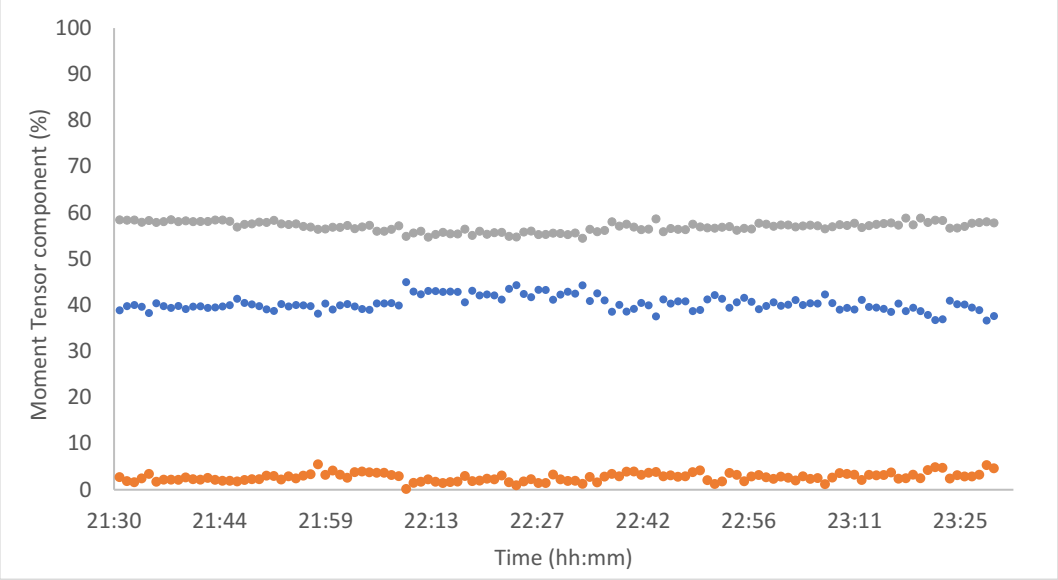

Figure 3.24. Results of the decomposition for the inversion of all tremor windows (MT+F solution) are shown. The gray, blue and orange dots indicate the percentage of ISO, CLVD and DC components, respectively.

As concerns the normal axis orientation of deviatoric component, considering only the MT + F case, the results in **Fig 3.25** show stable values during the entire duration of the lava fountain paroxysmal phase.

In particular, normal axis orientation of deviatoric component shows mean value of azimuth $\varphi \approx 344°$ with standard deviation of 16° and mean value of dip $\theta \approx 7°$ with standard deviation of 2°. The azimuth φ of normal axis orientation of deviatoric component show more scattered values during the activity peak of the lava fountain, while both before and after azimuth values tend to be rather stable and similar. The dip θ values, on the other hand, show a high stability during the whole analyzed interval.

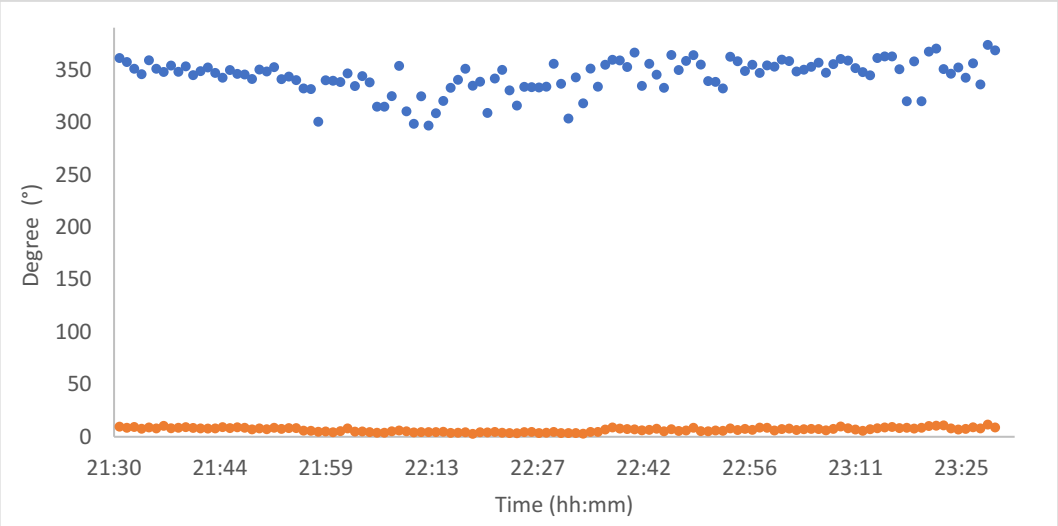

Figure 3.25. Normal axis orientation of deviatoric component for the inversion of all the tremor windows (MT+F solution). The blue and orange dots represent the values of azimuth φ and dip θ, respectively.

To confirm the mechanism, constrained inversions for a crack were carried out. As in the case of the unconstrained inversion, even in this case smaller misfit values were obtained when considering Moment Tensor plus Single Forces. These analyses confirm how the crack mechanism is the most plausible behavior for these events (**Tab. 3.2**).

EVENT	INVERSION	MISFIT	AIC
Date of lava fountain (mm/dd/yyyy): 08/05/2011 Time interval, GMT (hh:mm:ss): 22:14:10-22:15:50	MT+F	0.189	-77926
	MT	0.421	-29853
	Cr+F	0.360	-19939
	Cr	0.700	15902

Table 3.2. Misfit and AIC values for different unconstrained inversions (MT and MT+F), and for Constrained inversions. Cr, denote crack constrained inversion.

3.2.6 Discussion and conclusions

In order to improve the knowledge on the dynamical and geometrical features of the shallow plumbing system of the Mount Etna volcano, a moment tensor

inversion was performed on the signals recorded by the monitoring seismic network managed by INGV-OE. Specifically, the work done is an absolute novelty for the Mt. Etna volcano, as for the first time a study based on the moment tensor inversion was carried out on the volcanic tremor. For this purpose, seismic signals recorded during the lava fountain episode at the NSEC on 5 August 2011, the ninth of 25 episodes that occurred with the paroxysmal cycle of the 2011-2012 period (Behncke et al., 2014), were taken into consideration.

By using a frequency-domain, full-waveform inversion of the broadband ground displacement recordings, the moment tensor inversions of volcanic tremor were performed essentially into four steps. First, in order to limit distortion effects due to topography, heterogeneity and near surface velocity structure, it was decided to perform the inversion analysis considering only the low frequency-components of the volcanic tremor, the 0.2 - 0.5 Hz frequency band. Second, considering the need to reduce the source at one point for the moment tensor inversion analysis, the location of the tremor source was carried out in two phases: first, (i) the volume of probable sources of the volcanic tremor was identified by amplitude decay method following Di Grazia et al. (2006), while subsequently (ii) the best point solution for the source contained in the detected volume, was identified by the spatial distribution of moment tensor inversion misfit, at depth of about 200 meters from the surface of the volcanic edifice. Third, using an unconstrained inversion, the type of involved mechanism was determined for 2-hour-long episode of lava fountaining; for each window in which the seismic signal was divided, the source location was assumed to be fixed and equal to the source found during phase of maximum tremor amplitude. Finally, the constrained inversion was performed to confirm the source mechanism.

MTI analysis of the volcanic tremor recorded during the whole lava fountain paroxysmal phase provided mechanisms with a mean value and standard deviation of isotropic component equal to 56.94 % and 1.04 %, respectively. Moreover, deviatoric part shows the normal axis oriented with a mean value of azimuth $\varphi \approx 344°$ (with standard deviation of about 16°) and a mean value of dip

$\theta \approx 5°$ (with standard deviation of about 2°), likely generated by a sub-horizontal crack.

For the source mechanisms of volcano-seismic signals, several works in literature show how solutions such as sub-horizontal cracks can be obtained by the moment tensor inversion. For example, by moment tensor inversion considering both six moment and three single forces, Ohminato et al. (1998) explained the seismic source mechanism of VLP events, recorded at Kilauea volcano (Hawaii) during the crisis of 1 February 1996, as a pulsating transport mechanism operating on a sub-horizontal crack linking the summit reservoir to the east rift of Kilauea. The crack acts like a buffer in which a batch of fluid (magma and/or gas) accumulates over a period of 1-3 minutes before being rapidly injected into a larger reservoir (possibly the east rift) over a timescale of 5-10 s. Kumagai et al. (2002) performed a moment tensor inversion of LP events recorded at Kusatsu-Shirane (Japan) between August 1992 and January 1993. They constrained a sub-horizontal crack located a few hundred meters beneath the summit crater lakes. Arciniega-Ceballos et al. (2012) performed a moment tensor inversion of LP events recorded at Popocatépetl volcano (Mexico). They obtained a sub-horizontal crack located a few hundred meters from the surface, probably a steam-filled crack.

Davi et al. (2012), instead, performed the moment tensor inversion of volcanic tremor recorded at Arenal volcano (Costa Rica) during a seismic experiment in February 2005. Again, the authors constrained a sub-horizontal crack, interpreted as a fracture in the plug that opens and closes periodically. This crack acts as a valve through which pulses of gas escape and it is controlled by pressure oscillations in the underlying resonating conduit (Lesage et al., 2006). However, it is important to notice that the obtained solutions reveal that the source mechanisms are predominately isotropic.

According to the above mentioned studies, the sub-horizontal crack, constrained at Mt. Etna, could be interpreted as a valve through which gas-rich magma is ejected in the atmosphere during lava fountain activities.

As explained by De Barros et al. (2011), moment tensor inversion is particularly sensitive to the station spatial distribution and stations close to the source positions are especially needed to correctly invert seismic source mechanism. A good coverage of stations in the source area should give a better position of the focal volume in which the source is located, limiting the attenuation effect.

Therefore, considering the available data or this study, were good configuration possible of seismic stations, composed by eleven 3-component seismic stations (of which seven within max 2.6 km from the source of volcanic tremor), was used. However, 6 out of 33 components available were excluded due to technical failure and/or low signal to noise ratio.

For this study, a poorly constrained velocity model was used because for Mt. Etna volcano there is not a well resolved velocity model focused on the shallowest structures of the volcano. This represented an important limit for moment tensor inversion: in fact, Bean et al. (2008) have demonstrated that the marked sensitivity to the shallow velocity model prevents the recovery of the correct unconstrained solution and can lead to an entirely wrong orientation of the source structure.

Therefore, for the choice of the velocity model the results of Zuccarello (2015) were considered. This author carried out tests by taking into consideration three different velocity models and comparing synthetic and real signals. For this work, the velocity model, for which the author found the lower misfit values in the synthetic-real seismograms fit, was used. In particular, the velocity model in question considers 1800 m/s and 1000 m/s for P- and S-waves velocity, respectively, and it is the same one that De Barros et al., 2009 used for LP events location during the 2008 Etna activity.

Furthermore, attention must be paid on the role of the single forces. In this study, the single forces exhibit similar magnitude (and ratio with the MT components) found by Chouet et al. (2008) for the Stromboli VLP source inversion. In addition, as was done by these authors, it was decided to consider reliable the results characterized by the lowest values of misfit and Akaike Information Criterion (AIC), i.e. the solutions obtained with the uncostrained inversion considering moment

tensor plus single forces. However, it has been demonstrated how, generally the forces cannot be correctly reconstructed as they heavily reflect the errors coming from the velocity mismodeling and source mislocation. A study conducted for VLP signals by De Barros et al. (2013) showed that strong single forces are required to compensate for velocity mismodeling and source mislocation. Even if their analyses were too simple to reproduce the complexity of the seismic wavefield recorded in a volcanic environment, they illustrated how spurious single forces are necessary to reconstruct the observed converted surface waves, produced by an interface or the free surface.

In particular, even if low velocity layers have been observed at some volcanoes both on the top of the edifice (e.g. Cauchie and Saccorotti, 2013) and at lower altitude (e.g., Zuccarello et al., 2016), they are not usually considered in moment tensor inversion, inducing location error. Due to these errors, the inversion process gives rise to spurious single forces producing fictitious waves with comparable amplitudes to those from the moment tensor part of the solution. In the end, the misfit difference between moment tensor inversion with and without single forces may be rather large and comes from the mismodeling and not from inversion for the sources itself (De Barros et al., 2013). The only way to solve this problem is to use synthetic tests, and, at the same time, a deeper knowledge of the velocity model, especially in the shallow parts of the edifice (as suggested by Bean et al., 2008).

In conclusion, moment tensor inversion of the volcanic tremor presented in this study is affected by limits that, substantially, depend on the poor knowledge on Mt. Etna shallowest velocity model. This is important because a lack of knowledge of the velocity model can lead to incorrect source localization and does not allow the correct reconstruction of the source mechanism. However, despite this limitation, considering i) good coverage of the seismic network near the source of volcanic tremor and ii) the low misfit values obtained with the constrained inversion, the study carried out on the 2-hour-long seismic signals recorded during the lava fountaining of 5 August 2011 has allowed to obtain a stable crack-like

geometry for the volcanic tremor source, with constant orientation and mechanism, expression of a tensile source.

3.2.7 Suggested future work

One of the main problems in the moment tensor inversion of volcanic tremor recorded at Mt. Etna is the use of poorly defined velocity model of the shallowest structures of volcano. In future, more detailed velocity models could reduce the uncertainty about the solutions obtained with the inversion.

In order to confirm the features of the volcanic tremor source constrained during lava fountains activity, the same study could be extended to other periods of eruptive activity at Mt. Etna, in which similar dynamics has been observed, i.e. the cycles of lava fountains at the NSEC that have characterized the recent activity of the volcano. This would allow to evaluate the stability and / or possible temporal variations of the volcanic tremor source in the last years.

Finally, to frame the results obtained by moment tensor inversion analysis of volcanic tremor within the multiparametric studies, it could allow to improve the knowledge concerning the geometrical and dynamical characteristics of the shallow plumbing systems of Mt. Etna volcano.

CHAPTER 4 – CONCLUSIONS

4.1 GENERAL SUMMARY

During 2011-2012, an intense activity at the summit craters of Mount Etna characterized by 25 episodes of lava fountaining at the NSEC, was observed. Specifically, three eruptive phases alternated with periods of quiescence (Phase I: from January to May 2011; Phase II: from July to November 2011; Phase III: from January to April 2012).

Understanding the dynamics of volcanic activity at Mt. Etna by volcanic tremor analysis during the considered period was the main goal of the conducted research. To this end, a two-pronged study was carried out. In particular, i) a first investigation was based on the quantitative comparison between volcanic tremor and other volcanological time series for the time interval between 1 January 2010 and 31 December 2012, while ii) the second study was focused on the moment tensor inversion (MTI) of the volcanic tremor, recorded during the lava fountaining episode of 5 August 2011. The first study was applied to highlight any relationships between volcanic tremor and other parameters, that allow us to describe the volcano internal dynamics; the second study, instead, was applied to obtain information about location, mechanism and geometry of the volcanic tremor source during lava fountaining activity.

For the first study, a quantitative comparison between the time series of the volcanic tremor, soil CO_2 flux and SO_2 flux at the summit craters, was performed. After having applied four different methodologies of analysis, Randomized Cross Correlation technique showed a significant correlation between volcanic tremor and geochemical time series. In particular, volcanic tremor RMS amplitude turned out to be delayed by 35 - 78 days with respect to soil CO_2 flux, while tremor was likely to precede the SO_2 flux by 51 - 74 days. The detected time lags between the considered time series were compatible with the depth of the associated sources: indeed, Caracausi et al. (2003) showed that the largest exsolution of the CO_2 initially dissolved in basaltic magmas takes place at about 12 km b.s.l. (Caracausi et al., 2003), determining increases in soil CO_2 flux both from the vents and the

slopes of the edifice. On the other hand, the source of volcanic tremor, likely related to fluid dynamics within the plumbing system (e.g. Chouet and Matoza, 2013), is much shallower (generally above sea level; e.g. Di Grazia et al., 2006; Patanè et al. 2008; Cannata et al., 2015). In the light of it, the time lag can be related to the transfer velocity of fluids from the deeper to the shallower portions of the volcano. The different lags observed between volcanic tremor amplitude and SO_2 are likely to reflect the shallower source of SO_2 release with respect to the CO_2 (a few km of depth; e.g. Burton et al., 2003). In light of this, for the activity observed at Mt. Etna during 2011-2012, it was possible to hypothesize pressurization stages of shallow plumbing system before lava fountaining sequence, likely associated with the uprise of gas-rich magma.

As for the second study, instead, the MTI of the volcanic tremor recorded at Mt. Etna represents an absolute novelty for this volcano. For this purpose, the volcanic tremor recorded during the lava fountain of 5 August 2011 was considered. The MTI procedure is sensitive to some factors such as: i) topography and free surface (e.g. Ohminato and Chouet, 1997; Neuberg and Pointer, 2000); ii) spatial distribution of stations (e.g. De Barros et al., 2011); iii) accuracy of the shallow velocity model for the of P- and S-waves propagation in the medium (Bean et al., 2008). In order to limit the attenuation and distortion effect, volcanic tremor filtered at low-frequency band (0.2 - 0.5 Hz) and an Elastic Lattice Model ELM limited above by the real topographic surface of Mt. Etna volcano, were considered. In order to optimize the spatial distribution of seismic stations, best configuration of 11 stations were taken into consideration, of which 7 were located close to the summit area and then to the identified volcanic tremor source by amplitude decay method (Di Grazia et al., 2006). Moreover, the centroid representative of volcanic tremor source, retrieved by amplitude decay method, was used to constrain the possible source locations in the ELM. Finally, the velocity mode,l by which Zuccarello (2015) obtained the lowest misfit values between synthetic and real signals, was taken into consideration. Specifically, it is a

homogeneous velocity model similar to that used by De Barros et al. (2011) for MTI of LP events recorded at Mt. Etna during 2008 eruption.

For the volcanic tremor recorded during 5 August 2011 lava fountaining, source location at about 200 meters of depth from surface and near NSEC was obtained by MTI procedure. Moreover, the same analysis provided a mechanism with nearly 57% isotropic component, while deviatoric part shows the normal axis oriented with azimuth $\varphi \approx 345°$ and dip $\theta \approx 5°$, likely generated by a sub-horizontal crack.

For the source mechanisms of volcano-seismic signals, several works in literature show how sub-horizontal cracks are often obtained by the MTI (e.g. Ohminato et al., 1998; Kumagai et al., 2002; Arciniega-Ceballos et al., 2012; Davi et al., 2012). According to the above-mentioned studies, the sub-horizontal crack, constrained at Mt. Etna, could be interpreted as a valve through which gas-rich magma is ejected in the atmosphere during lava fountain activities.

In conclusion, the comparison between geophysical and geochemical time series and the MTI of volcanic tremor allowed to obtain information about the dynamics of the plumbing system of Mt. Etna during the 2011-2012 activity.

4.2 SUGGESTED FUTURE WORK AND PERSPECTIVES

Considering the studies performed in the framework of this PhD thesis, future works could be aimed at reducing the uncertainties and the limits, that characterized the used methods and procedures, as well as at extending the dataset.

Focusing on the quantitative multiparametric comparison, future work could be done to extend the analysis to other parameters, for example ground deformation data such as tilt and strainmeter, and to longer time intervals.

A successful application of these analyses would not only improve the knowledge about internal volcano dynamics, but could allow the development of strategies able to identify automatically significant changes in trends, identify synchronous/delayed changes in trends between different data, with a significant improvement in hazard assessment and volcano surveillance.

Focusing on the MTI analysis, further work should be done to better define the seismic velocity model of the volcano shallowest structures, which strongly influence the final MTI results. Furthermore, another possible development could be to frame the MTI analysis in a multiparametric study; comparing volcano seismicity with other monitoring data such as fluid/gas geochemistry, acoustic and ground deformation will strongly improve the understanding of the source mechanism of volcanic tremor.

All these considerations could lead to a better understanding of the volcanic tremor source.

REFERENCES

- Aki, K., Fehler, M., Das, S., 1977. *Source mechanism of volcanic tremor: fluid driven crack models and their application to the 1963 Kilauea eruption*. Journal of Volcanology and Geothermal Research 2, 259–287.
- Aki, K., & Koyanagi, R., 1981. *Deep volcanic tremor and magma ascent mechanism under Kilauea, Hawaii*. Journal of Geophysical Research: Solid Earth, 86(B8), 7095-7109.
- Aki, K., Ferrazzini, V., 2000. *Seismic monitoring and modeling of an active volcano for prediction*. Journal of Geophysical Research 105 (B7), 16,617–16,640.
- Aki, K. & Richards, P. G, 2002. *Quantitative Seismology, 2nd ed.*, University Science Books, Sausalito, California, 700 pp.
- Alidibirov, M., Dingwell, D.B., 1996. *Magma fragmentation by rapid decompression*. Nature 380, 146–148.
- Allard, P., 1997. *Endogenous magma degassing and storage at Mt. Etna*. Geophys. Res. Lett. 24:2219–2222
- Almendros, J., Chouet, B., Dawson, P., 2001a. *Spatial extent of a hydrothermal system at Kilauea Volcano, Hawaii, determined from array analyses of shallow long-period seismicity 1. Method*. Journal of Geophysical Research 106, 13,565–13,580.
- Almendros, J., Chouet, B., Dawson, P., 2001b. *Spatial extent of a hydrothermal system at Kilauea Volcano, Hawaii, determined from array analyses of shallow long-period seismicity 2.* Results. Journal of Geophysical Research 106, 13,581–13,597.
- Aloisi, M., Bonaccorso, A., Gambino, S., 2006. *Imaging composite dike propagation (Etna, 2002 case)*. Journal of Geophysical Research, 111, doi:10.1029/2005JB00390.
- Alparone, S., Andronico, D., Lodato, L., & Sgroi, T., 2003. *Relationship between tremor and volcanic activity during the Southeast Crater eruption on Mount Etna in early 2000*. Journal of Geophysical Research: Solid Earth, 108(B5).

- Alparone, S., Cannata, A., Gambino, S., Gresta, S., Milluzzo, V., Montalto, P., 2010. *Time-space variation of volcano-seismic events at La Fossa (Vulcano, Aeolian Islands, Italy): new insights into seismic sources in a hydrothermal system*. Bulletin of Volcanology 72, 803–816.
- Andronico, D., Cristaldi, A., Scollo, S., 2013. *The 12–13 January 2011 lava fountain of Mt. Etna volcano: total mass and grain-size evaluation of the fallout deposit*. Geophys. Res. Abstr. 15, EGU2013–EGU11687.
- Andronico, D., Lo Castro, M. D., Sciotto, M., and Spina, L., 2013. *The 2010 ash emissions at the summit craters of Mt Etna: Relationship with seismo-acoustic signals*, J. Geophys. Res. Solid Earth, 118, 51–70, doi:10.1029/2012JB009895.
- Arciniega-Ceballos, A., Dawson, P., Chouet, B.A., 2012. *Long-period seismic source characterization at Popocatépetl Volcano, Mexico*. Geophysical Research Letters 39, L20307. http://dx.doi.org/10.1029/2012GL053494
- Armienti, P., Perinelli, C., & Putirka, K. D., 2012. *A new model to estimate deep-level magma ascent rates, with applications to Mt. Etna (Sicily, Italy)*. Journal of Petrology, 54(4), 795-813.
- Azzaro, R., Bonforte, A., Branca, S., & Guglielmino, F., 2013. *Geometry and kinematics of the fault systems controlling the unstable flank of Etna volcano (Sicily)*. Journal of volcanology and geothermal research, 251, 5-15.
- Balmforth, N.J., Craster, R.V., Rust, A.C., 2005. *Instability in flow through elastic conduits and volcanic tremor*. Journal of Fluid Mechanics 527, 353–377.
- Bani, P., & Lardy, M., 2007. *Sulphur dioxide emission rates from Yasur volcano, Vanuatu archipelago*. Geophysical Research Letters, 34(20).
- Bartosch, T., Seidl, D. (1999). *Spectrogram analysis of selected tremor signals using Short-Time Fourier Transform and Continuous Wavelet Transform*. Ann. Geofis., 42, 3, 497-506.

- Battaglia, J., and Aki, K., 2003. *Location of seismic events and eruptive fissures on the Piton de la Fournaise volcano using seismic amplitudes,* J. Geophys. Res., 108(B8), 2364, doi:10.1029/2002JB002193.
- Battaglia, J., Ferrazzini, V., Staudacher, T., Aki, K., & Cheminée, J. L., 2005. *Pre-eruptive migration of earthquakes at the Piton de la Fournaise volcano (Réunion Island)*. Geophysical Journal International, 161(2), 549-558.
- Bean, C., Lokmer, I., O'Brien, G., 2008. *The influence of near-surface on long-period (LP) seismic signals and on moment tensor inversions: Simulated examples from Mt. Etna*. Journal of Geophysical Research, 113, B08308, doi:10.1029/2007JB005468.
- Behncke, B., Branca, S., Corsaro, R. A., De Beni, E., Miraglia, L., & Proietti, C., 2014. *The 2011–2012 summit activity of Mount Etna: Birth, growth and products of the new SE crater.* Journal of Volcanology and Geothermal Research, 270, 10-21.
- Benoit, J.P., Mc Nutt, S.R., 1997. *New constraints on source processes of volcanic tremor at Arenal Volcano, Costa Rica, using broadband seismic data*. Geophysical Research Letters 24 (4), 449–452.
- Bonaccorso, A., Bonforte, A., Guglielmino, F., Palano, M., & Puglisi, G., 2006. *Composite ground deformation pattern forerunning the 2004–2005 Mount Etna eruption*. Journal of Geophysical Research: Solid Earth, 111(B12).
- Bonforte, A., Guglielmino, F., Coltelli, M., Ferretti, A., & Puglisi, G.,2011. *Structural assessment of Mount Etna volcano from Permanent Scatterers analysis*. Geochemistry, Geophysics, Geosystems, 12(2).
- Borgia, A., Ferrari, L., & Pasquarè, G., 1992. *Importance of gravitational spreading in the tectonic and volcanic evolution of Mount Etna*. Nature, 357(6375), 231.
- Bousquet, J. C., & Lanzafame, G., 2004. *The tectonics and geodynamics of Mt. Etna: synthesis and interpretation of geological and geophysical data. Mt. Etna: volcano laboratory*, 29-47.

- Branca, S., and Carlo, P., 2005. T*ypes of eruptions of Etna volcano AD 1670–2003: implications for short-term eruptive behaviour*. Bull. Volcanol. 67, 732–742.
- Branca, F., S., Coltelli, M., Groppelli, G., and Pasquarè, G., 2009. *Note illustrative alla carta geologica d'Italia alla scala 1:50.000*. Foglio 625 Acireale.
- Branca, S., Coltelli, M., and Groppelli, G. (2004). *Geological Evolution of Etna volcano. In Etna Volcano Laboratory*, (American Geophysical Union), pp. 49–63.
- Branca, S., Coltelli, M., De Beni, E., and Wijbrans, J., 2008. *Geological evolution of Mount Etna volcano (Italy) from earliest products until the first central volcanism (between 500 and 100 ka ago) inferred from geochronological and stratigraphic data*. Int. J. Earth Sci. 97, 135–152.
- Branca, F., S., Coltelli, M., Groppelli, G., and Lentini, F., 2011a. *Geological map of Etna volcano, 1:50,000 scale*. 130.
- Branca, S., Coltelli, M., Groppelli, G., and Lentini, F., 2011b. *Geological map of Etna volcano, 1:50,000 scale*. Ital. J. Geosci. 130, 265–291.
- Bromirski, P. D., Duennebier, F. K., Stephen, R. A., 2005. *Mid-ocean microseisms*. Geochemistry, Geophysics, Geosystems, 6(4).
- Burton, M., Allard, P., Muré, F., Oppheneimer, C., 2003. *FTIR remote sensing of fractional magma degassing at Mount Etna, Sicily.* In: Oppenheimer, C., Pyle, D.M., Barclay, J. (Eds.), Volcanic Degassing, Spec. Publ.-Geol. Soc. London, vol. 213, pp. 281– 293.
- Cabras, G., Carniel, R., & Wasserman, J., 2010. *Signal enhancement with generalized ICA applied to Mt. Etna volcano, Italy*. Bollettino di Geofisica Teorica ed Applicata, 51(1).
- Calvari, S., Groppelli, G., and Pasquarè, G., 1994. *Preliminary geological data on the south-western wall of the Valle del Bove, Mt Etna, Sicily*. Acta Volcanol. 5, 15–30.

- Campion, R., Salerno, G. G., Coheur, P. F., Hurtmans, D., Clarisse, L., Kazahaya, K., Burton, M., Caltabiano, T., Clerbaux, C., & Bernard, A., 2010. *Measuring volcanic degassing of SO2 in the lower troposphere with ASTER band ratios*. Journal of volcanology and geothermal research, 194(1-3), 42-54.
- Cannata, A., Hellweg, M., Di Grazia, G., Ford, S., Alparone, S., Gresta, S., ... & Patanè, D. (2009). *Long period and very long period events at Mt. Etna volcano: Characteristics, variability and causality, and implications for their sources*. Journal of Volcanology and Geothermal Research, 187(3-4), 227-249.
- Cannata, A., Giudice, G., Gurrieri, S., Montalto, P., Alparone, S., Di Grazia, G., Favara, R., Gresta, S., & Liuzzo, M. 2010a. *Relationship between soil CO_2 flux and volcanic tremor at Mt. Etna: Implications for magma dynamics*. Environmental Earth Sciences, 61(3), 477-489.
- Cannata, A., Di Grazia, G., Montalto, P., Ferrari, F., Nunnari, G., Patanè, D., & Privitera, E., 2010b. *New insights into banded tremor from the 2008–2009 Mount Etna eruption*. Journal of Geophysical Research: Solid Earth, 115(B12).
- Cannata, A., Spedalieri, G., Behncke, B., Cannavò, F., Di Grazia, G., Gambino, S., Gresta, S., Gurrieri, S., Liuzzo, M. & Palano, M. 2015. *Pressurization and depressurization phases inside the plumbing system of Mount Etna volcano: Evidence from a multiparametric approach*. Journal of Geophysical Research: Solid Earth, 120(9), 5965-5982.
- Cannata, A., Larocca, G., Del Carlo, P., Giudice, G., Giuffrida, G. B., Liuzzo, M., Zuccarello, L., Di Grazia, G., Gambino, S., Privitera, E., Delladio, A., Grigioni, P. (2017). *Characterization of seismic signals recorded in Tethys Bay, Victoria Land (Antarctica): data from atmosphere-cryosphere-hydrosphere interaction*. Annals of Geophysics.
- Caracausi, A., Italiano, F., Paonita, A., Rizzo, A., 2003. *Evidence of deep magma degassing and ascent by geochemistry of peripheral gas emissions*

at Mount Etna (Italy): assessment of the magmatic reservoir pressure. J. Geophys. Res. 108:2463. doi:10.1029/2002JB002095

- Carbone, D., Zuccarello, L., & Saccorotti, G., 2008. *Geophysical indications of magma uprising at Mt Etna during the December 2005 to January 2006 non-eruptive period*. Geophysical Research Letters, 35(6).
- Catalano, R., Doglioni, C., Merlini, S., 2001. *On the Mesozoic Ionian basin.* Geophys. J. Int., 144, 49-64.
- Cauchie, L., & Saccorotti, G., 2013. *Probabilistic inversion of Rayleigh-wave dispersion data: an application to Mt. Etna, Italy*. Journal of seismology, 17(2), 335-346.
- Chen, Y. N., Gung, Y., You, S. H., Hung, S. H., Chiao, L. Y., Huang, T. Y., Chen Y. L., Liang W. T., Jan S., 2011. *Characteristics of short period secondary microseisms (SPSM) in Taiwan: The influence of shallow ocean strait on SPSM.* Geophysical Research Letters, 38(4).
- Chouet, B., 1981. *Ground motion in the near field of a fluid-driven crack and its interpretation in the study of shallow volcanic tremor*. Journal of Geophysical Research: Solid Earth, 86(B7), 5985-6016.
- Chouet, B., 1985. *Excitation of a buried magmatic pipe: a seismic source model for volcanic tremor.* Journal of Geophysical Research 90, 1881–1893.
- Chouet, B., 1986. *Dynamics of a fluid-driven crack in three dimensions by the finite difference method.* Journal of Geophysical Research 91, 13,967–13,992.
- Chouet, B.A., 1988. *Resonance of a fluid-driven crack: radiation properties and implications for the source of long-period events and harmonic tremor*. J. Geophys. Res. 93, 4375-4400.
- Chouet, B., 1992. *A seismic model for the source of long-period events and harmonic tremor*. In Volcanic seismology (pp. 133-156). Springer, Berlin, Heidelberg.
- Chouet, B. (2003). *Volcano seismology*. Pure and Applied Geophysics, 160(3-4), 739-788.

- Chouet, B.A., Page, R.A., Stephens, C.D., Lahr, J.C., Power, J.A., 1994. *Precursory swarms of long-period events at Redoubt Volcano (1989–1990), Alaska: their origin and use as a forecasting tool*. Journal of Volcanology and Geothermal Research 62, 95–135.
- Chouet, B., 1996. *Long-period volcano seismicity: its source and use in eruption forecasting*. Nature 380, 309–316.
- Chouet, B., Saccorotti, G., Martini, M., Dawson, P., De Luca, G., Milana, G., Scarpa, R., 1997. *Source and path effects in the wave fields of tremor and explosions at Stromboli Volcano, Italy*. Journal of Geophysical Research 102 (B7), 15,129–15,150.
- Chouet, B., Dawson, P., Ohminato, T., Martini, M., Saccorotti, G., Giudicepietro, F., De Luca, G., Milana, G., Scarpa, R., 2003. *Source mechanisms of explosions at Stromboli Volcano, Italy, determined from moment-tensor inversions of very-long-period data*. Journal of Geophysical Research 108 (B1), 2019.
- Chouet, B., Dawson, P., Martini, M., 2008. *Shallow-conduit dynamics at Stromboli Volcano, Italy, imaged from waveform inversions*. In: Lane, S.J., Gilbert, J.S. (Eds.), Fluid Motions in Volcanic Conduits: A Source of Seismic and Acoustic Signals: Geol. Soc., London, Special Publications, 307, pp. 57–84.
- Chouet, B., Dawson, P., 2011. *Shallow conduit system at Kilauea Volcano, Hawaii, revealed by seismic signals associated with degassing bursts*. Journal of Geophysical Research 116, B12317.
- Chouet, B.A., Matoza, R.S., 2013. *A multi-decadal view of seismic methods for detecting precursors of magma movement and eruption.* J. Volcanol. Geotherm. Res. 252, 108–175.
- Collier, L., Neuberg, J., 2006. *Incorporating seismic observations into 2D conduit flow modeling*. Journal of Volcanology and Geothermal Research 152, 331–346.

- Corsaro, R.A., and Cristofolini, R., 2000. *Subaqueous volcanism in the Etnean area: evidence for hydro-magmatic activity and regional uplift inferred from the Castle Rock of Acicastello*. Elsevier Oxf. Roy. UNI 1976 Rev. 95, 209–225.
- Corsaro, R.A., and Pompilio, M., 2004. *Buoyancy-controlled eruption of magmas at Mt Etna: Buoyancy-controlled eruption of magmas at Mt Etna*. Terra Nova 16, 16–22.
- Cristofolini, R., Lentini, F., Patanè, G., & Rasà, R., 1979. *Intergrazione di dati geologici, geofisici e petrologici per la stesura di un profilo crostale in corrispondenza dell'Etna*. Bollettino della Società Geologica Italiana, 98(2), 239-247.
- D'Agostino, M., Di Grazia, G., Ferrari, F., Langer, H., Messina, A., Reitano, D., & Spampinato, S., 2013. *Volcano monitoring and early warning on Mt. Etna, Sicily based on volcanic tremor: methods and technical aspects*. Complex Monitoring of Volcanic Activity, 53-92.
- D'Auria, L., Giudicepietro, F., Aquino, I., Borriello, G., Del Gaudio, C., Lo Bascio, D., Martini, M., Ricciardi, G.P., Ricciolino, P., Ricco, C., 2011. *Repeated fluid-transfer episodes as a mechanism for the recent dynamics of Campi Flegrei caldera (1989–2010)*. Journal of Geophysical Research 116, B04313. http://dx.doi.org/10.1029/2010JB007837.
- Davi, R., O'Brien, G.S., Lokmer, I., Bean, C.J., Lesage, P., Mora, M.M., 2010. *Moment tensor inversion of explosive long period events recorded on Arenal volcano, Costa Rica, constrained by synthetic tests*. Journal of Volcanology and Geothermal Research 194, 189–200.
- Davi, R., O'Brien, G.S., De Barros, L., Lokmer, I., Bean, C.J., Lesage, P., Mora, M.M., Soto, G.J., 2012. *Seismic source mechanisms of tremor recorded on Arenal volcano, Costa Rica, retrieved by waveform inversion*. Journal of Volcanology and Geothermal Research 213–214, 1–13.

- Dawson, P. B., Chouet, B. A., Okubo, P. G., Villaseñor, A., & Benz, H. M. (1999). *Three-dimensional velocity structure of the Kilauea Caldera, Hawaii*. Geophysical Research Letters, 26(18), 2805-2808.
- De Barros, L., Bean, C.J., Lokmer, I., Saccorotti, G., Zuccarello, L., O'Brien, G.S., Métaxian, J.-P., Patanè, D., 2009. *Source geometry from exceptionally high-resolution long period event observations at Mt Etna during the 2008 eruption*. Geophysical Research Letters 36, L24305.
- De Barros, L., Lokmer, I., Bean, C.J., O'Brien, G.S., Saccorotti, G., Métaxian, J.-P., Zuccarello, L., Patanè, D., 2011. *Source mechanism of long-period events recorded by a high-density seismic network during the 2008 eruption on Mount Etna*. Journal of Geophysical Research 116, B01304.
- De Barros, L., Lokmer, I., and Bean, C.J., 2013. *Origin of spurious single forces in the source mechanism of volcanic seismicity*. J. Volcanol. Geotherm. Res. 262, 1–6.
- De Beni, E., Branca, S., Coltelli, M., Groppelli, G., and Wijbrans, J.R., 2011. *40Ar/39Ar isotopic dating of Etna volcanic succession*. Ital. J. Geosci. 130, 292–305.
- De Beni, E., Behncke, B., Branca, S., Nicolosi, I., Carluccio, R., Caracciolo, F. A., & Chiappini, M., 2015. *The continuing story of Etna's New Southeast Crater (2012–2014): Evolution and volume calculations based on field surveys and aerophotogrammetry*. Journal of Volcanology and Geothermal Research, 303, 175-186.
- De Caro, M., Monna, S., Frugoni, F., Beranzoli, L., Favali, P., 2014. *Seafloor seismic noise at Central Eastern Mediterranean sites*. Seismological Research Letters, 85(5), 1019-1033.
- Del Pezzo, E., De Martino, S., Gresta, S., Martini, M., Milana, G., Patanè, D., & Sabbarese, C., 1993. *Velocity and spectral characteristics of the volcanic tremor at Etna deduced by a small seismometer array*. Journal of volcanology and geothermal research, 56(4), 369-378.

- Di Grazia, G., Falsaperla, S. and Langer, H., 2006. *Volcanic tremor location during the 2004 Mount Etna lava effusion*, Geophys. Res. Lett., 33, L04304, doi:10.1029/2005GL025177
- Di Grazia, G., Cannata, A., Montalto, P., Patanè, D., Privitera, E., Zuccarello, L., & Boschi, E., 2009. *A multiparameter approach to volcano monitoring based on 4D analyses of seismo-volcanic and acoustic signals: The 2008 Mt. Etna eruption*. Geophysical Research Letters, 36(18).
- Dingwell, D.B., 1996. *Volcanic dilemma: flow or blow?* Science 273, 1054–1055
- Eaton, D., and Forouhideh, F., 2011. *Solid angles and the impact of receiver-array geometry on microseismic moment-tensor inversion*. GEOPHYSICS 76, WC77–WC85.
- Falsaperla, S., Privitera, E., Chouet, B., & Dawson, P., 2002. *Analysis of long-period events recorded at Mount Etna (Italy) in 1992, and their relationship to eruptive activity*. Journal of volcanology and geothermal research, 114(3-4), 419-440.
- Fehler, M., Chouet, B., 1982. *Operation of a digital seismic network on Mount St. Helens volcano and observations of long period seismic events that originate under the volcano*. Geophysical Research Letters 9, 1017–1020.
- Ferrazzini, V., Aki, K., 1987. *Slow waves trapped in a fluid-filled infinite crack: Implication for volcanic tremor.* Journal of Geophysical Research, 92, B9, 9215-9223.
- Foufoula-Georgiou, E., Kumar, P., Mukerji, T., & Mavko, G., 1995. *Wavelets in geophysics. Pure and Applied Geophysics*, 145(2), 374-375.
- Fujita, E., Ida, Y., Oikawa, J., 1995. *Eigen oscillation of a fluid sphere and source mechanism of harmonic volcanic tremor*. Journal of Volcanology and Geothermal Research 69, 365–378.

- Di Grazia, G., Falsaperla, S., & Langer, H., 2006. *Volcanic tremor location during the 2004 Mount Etna lava effusion*. Geophysical research letters, 33(4).
- Garcés, M.A., Hagerty, M.T., Schwartz, S.Y., 1998. *Magma acoustics and time-varying melt properties at Arenal Volcano, Costa Rica*. Geophysical Research Letters 25, 2293–2296.
- Gemmellaro, C., 1858. *La vulcanologia dell'Etna.* Tipografia dell'Accademia Gioenia, Catania, 266 pp., 1858.

  Gil Cruz, F., Chouet, B.A., 1997. *Long-period events, the most characteristic seismicity accompanying the emplacement and extrusion of a lava dome in Galeras Volcano, Colombia, in 1991*. Journal of Volcanology and Geothermal Research 77, 121–158.
- Gonnermann, H.M., Manga, M., 2007. *The fluid mechanics inside a volcano.* Annual Review of Fluid Mechanics 39, 321–356.
- Gordeev, E., 1993. *Modeling of volcanic tremor as explosive point sources in a single-layered, elastic half-space*. Journal of Geophysical Research: Solid Earth, 98(B11), 19687-19703.
- Gottschämmer, E., & Surono, I., 2000. *Locating tremor and shock sources recorded at Bromo Volcano*. Journal of volcanology and geothermal research, 101(1-2), 199-209.
- Green, D.N., Neuberg, J., 2006. *Waveform classification of volcanic low-frequency earthquake swarms and its implication at Soufrière Hills Volcano, Montserrat.* Journal of Volcanology and Geothermal Research 153, 51–63.
- Gresta, S., Privitera, E., Leotta, A., and Gasperini, P., 1996. *Analysis of the intermittent volcanic tremor observed at Mt. Etna, Sicily during March–May 1987*, Ann. Geophys., 39, 421–428.
- Grinsted, A., Moore, J.C., Jevrejeva, S., 2004. *Application of the cross wavelet transform and wavelet coherence to geophysical time series*. Nonlinear Process Geophys., 11, 561–566.

- Grob, M., Maggi, A., and Stutzmann, E., 2011. *Observations of the seasonality of the Antarctic microseismic signal, and its association to sea ice variability*, Geophys. Res. Lett., 38, L11302, doi:10.1029/2011GL047525.
- Gubbins, D., 2004. *Time Series Analysis and Inverse Theory for geophysicist.* Cambridge University press, England, 255 pp.
- Gurrieri, S., & Valenza, M., 1988. *Gas transport in natural porous mediums: A method for measuring CO_2 flows from the ground in volcanic and geothermal areas*, Rend. Soc. Ital. Mineral. Petrol., 43, 1151–1158.
- Gurrieri, S., Liuzzo, M., & Giudice, G., 2008. *Continuous monitoring of soil CO_2 flux on Mt. Etna: The 2004–2005 eruption and the role of regional tectonics and volcano tectonics*, J. Geophys. Res., 113, B09206, doi:10.1029/2007JB005003.
- Gvirtzman, Z., & Nur, A., 1999. *The formation of Mount Etna as the consequence of slab rollback*. Nature, 401(6755), 782.
- Hagerty, M.T., Schwartz, S.Y., Garces, M.A., Protti, M., 2000. *Analysis of seismic and acoustic observations at Arenal Volcano, Costa Rica, 1995-1997*. Journal of Volcanology and Geothermal Research 101, 27–65.
- Hamada, N., Jingu, H., Ikumoto, K., 1976. *On the volcanic earthquake with slowly decaying coda wave (in Japanese with English abstract)*. Bulletin of the Volcanological Society of Japan 21, 167–183.
- Hale, A.J., 2007. *Magma flow instabilities in a volcanic conduit: implications for long-period seismicity*. Physics of the Earth and Planetary Interiors 163, 163–178
- Harrington, R. M., & Brodsky, E. E., 2007. *Volcanic hybrid earthquakes that are brittle-failure events*. Geophysical Research Letters, 34(6).
- Harlow, D.H., Power, J.A., Laguerta, E.P., Ambubuyog, G., White, R.A., Hoblitt, R.P., 1996. *Precursory seismicity and forecasting of the June 15, 1991, eruption of Mount Pinatubo*. In: Newhall, C.G., Punongbayan, R.S.

(Eds.), Fire and Mud, Eruptions and Lahars of Mount Pinatubo, Philippines. Univ. of Washington Press, Seattle, Washington, pp. 285–305.

- Hasselmann, K., 1963. *A statistical analysis of the generation of microseisms*. Reviews of Geophysics, 1(2), 177-210.
- Hidayat, D., Chouet, B., Voight, B., Dawson, P., & Ratdomopurbo, A., 2002. *Source mechanism of very-long-period signals accompanying dome growth activity at Merapi volcano, Indonesia.* Geophysical research letters, 29(23).
- Jevrejeva, S., Moore, J.C., Grinsted, A., 2003. *Influence of the Arctic Oscillation and El Nino-Southern Oscillation (ENSO) on ice conditions in the Baltic Sea: the wavelet approach*. J. Geophys. Res. 108(D21), 4677, doi:10.1029/2003JD003417.
- Johnson, L. R., 1974. *Green's Function for Lamb's Problem*. Geophysical Journal of the Royal Astronomical Society, 37(1), 99-131.
- Johnson, J. B., & Aster, R. C., 2005. *Relative partitioning of acoustic and seismic energy during Strombolian eruptions*. Journal of Volcanology and Geothermal Research, 148(3-4), 334-354.
- Julian, B., 1994. *Volcanic tremor: nonlinear excitation by fluid flow.* Journal of Geophysical Research, 99, 11859-11877.
- Julian, B. R., Miller, A. D., Foulger, G. R., 1998. *Non-double-couple earthquakes. 1, Theory*. Review of Geophysics, 36, 525-549
- Kadota, T. and Labianca, F., 1981: G*ravity-wave induced pressure fluctuations in the deep ocean*. IEEE J. Oceanic, OE-6 (2), 50-58.
- Kaneshima, S., Kawakatsu, H., Matsubayashi, H., Sudo, Y., Tsutsui, T., Ohminato, T., Ito, H., Uhira, K., Yamasato, H., Oikawa, J., Takeo, M., Iidaka, T., 1996. *Mechanism of phreatic eruptions at Aso Volcano inferred from near-field broadband seismic observations*. Science 273, 642–645.
- Kawakatsu, H., Kaneshima, S., Matsubayashi, H., Ohminato, T., Sudo, Y., Tsutsui, T., Uhira, K., Yamasato, H., Ito, H., Legrand, D., 2000. *Aso94: Aso seismic observation with broadband instruments.* Journal of Volcanology and Geothermal Research 101, 129–154.

- Kostantinou, K.I., Schlindwein, V., 2002. *Nature, wavefield properties and source mechanism of volcanic tremor: a review.* Journal of Volcanology and Geothermal Research, 119, 161-187.
- Kubotera, A., 1974. *Volcanic tremors at Aso volcano. In Developments in Solid Earth Geophysics* (Vol. 6, pp. 29-47). Elsevier.
- Kumagai, H., Chouet, B.A., 1999. *The complex frequencies of long-period seismic events as probes of fluid composition beneath volcanoes.* Geophysical Journal International 138, F7–F12.
- Kumagai, H., Chouet, B.A., 2000. *Acoustic properties of a crack containing magmatic or hydrothermal fluids.* Journal of Geophysical Research 105 (B11), 25,493–25,512.
- Kumagai, H., Chouet, B.A., 2001. *The dependence of acoustic properties of a crack on the resonance mode and geometry.* Geophysical Research Letters 28, 3325–3328.
- Kumagai, H., Chouet, B.A., Nakano, M., 2002a. *Waveform inversion of oscillatory signatures in long-period events beneath volcanoes*. Journal of Geophysical Research 107 (B11), 2301.
- Kumagai, H., Chouet, B.A., Nakano, M., 2002b. *Temporal evolution of a hydrothermal system in Kusatsu-Shirane Volcano, Japan, inferred from the complex frequencies of long-period events.* Journal of Geophysical Research 107 (B10), 2236. http://dx.doi.org/10.1029/2001JB000653.
- Kumagai, H., Chouet, B.A., Dawson, P.B., 2005. *Source process of a long-period event at Kilauea Volcano, Hawaii.* Geophysical Journal International 161, 243–254.
- Kumazawa, M., Imanishi, Y., Fukao, Y., Furumoto, M., Yamamoto, A., 1990. *A theory of spectral analysis based on the characteristic property of a linear dynamic system*. Geophysical Journal International 101, 613–630.
- Ichihara, M., Rubin, M.B., 2010. *Brittleness of fracture in flowing magma*. Journal of Geophysical Research 115, B12202.

- Ichihara, M., Takeo, M., Yokoo, A., Oikawa, J., & Ohminato, T., 2012. *Monitoring volcanic activity using correlation patterns between infrasound and ground motion*. Geophysical Research Letters, 39(4).
- Iverson, R.M., 2008. *Dynamics of seismogenic volcanic extrusion resisted by a solid surface plug, Mount St. Helens, 2004–2005*. In: Sherrod, D.R., Scott, W.E., Stauffer, P.H. (Eds.), A Volcano Rekindled: The Renewed Eruption of Mount St. Helens, 2004–2006: U.S. Geological Survey Professional Paper 1750, pp. 425–460 (Chap. 21).
- Iverson, R.M., Dzurisin, D., Gardner, C.A., Gerlach, T.M., LaHusen, R.G., Lisowski, M., Major, J.J., Malone, S.D., Messerich, J.A., Moran, S.C., Pallister, J.S., Qamar, A.I., Schilling, S.P., Vallance, J.W., 2006. *Dynamics of seismogenic volcanic extrusion at Mount St. Helens in 2004–05*. Nature 444, 439–443.
- Lahr, J. C., Chouet, B. A., Stephens, C. D., Power, J. A., & Page, R. A., 1994. *Earthquake classification, location, and error analysis in a volcanic environment: Implications for the magmatic system of the 1989–1990 eruptions at Redoubt Volcano, Alaska*. Journal of Volcanology and Geothermal Research, 62(1-4), 137-151.
- Lay, T., Wallace, T. C., 1995. *Modern Global Seismology*. Academic Press, San Diego, USA, 521 pp.
- Langer, H., & Falsaperla, S., 1996. *Long-term observation of volcanic tremor on Stromboli volcano (Italy): a synopsis*. pure and applied geophysics, 147(1), 57-82.
- Leet, R.C., 1988. *Saturated and subcooled hydrothermal boiling in groundwater-flow channels as a source of harmonic tremor.* Journal of Geophysical Research 93, 4835–4849.
- Legrand, D., Kaneshima, S., Kawakatsu, H., 2000. *Moment tensor analysis of near-field broadband waveforms observed at Aso Volcano, Japan*. Journal of Volcanology and Geothermal Research 101, 155–169.

- Leonardi, S., Gresta, S., & Mulargia, F., 2000. *Searching for a significant correlation between volcanic tremor amplitude and SO_2 emissions at Mount Etna volcano, Sicily*. Geophysical Journal International, 141(3), 832-834.
- Lesage, P., Glangeaud, F., Mars, J. (2002). Applications of autoregressive and time-frequency analysis to the study of volcanic tremor and LP events. J. Volcanol. Geotherm. Res., 114, 391-417
- Lesage, P. (2008). Automatic estimation of optimal autoregressive filters for the analysis of volcanic seismic activity. Nat. Hazards Earth Syst. Sci., 8, 369-376.
- Lesage, P., Mora, M.M., Alvarado, G.E., Pacheco, J., Metaxian, J.P., 2006. *Complex behavior and source model of the tremor at Arenal volcano, Costa Rica*. Journal of Volcanology and Geothermal Research 157, 49–59.
- Liuzzo, M., Gurrieri, S., Giudice, G., & Giuffrida, G., 2013. T*en years of soil CO_2 continuous monitoring on Mt. Etna: Exploring the relationship between processes of soil degassing and volcanic activity*, Geochem. Geophys. Geosyst., 14, 2886–2899, doi:10.1002/ggge.20196.
- Lokmer, I., Bean, C.J., Saccorotti, G., Patane, D., 2007. *Moment-tensor inversion of LP events recorded on Etna in 2004 using constraints obtained from wave simulation tests.* Geophysical Research Letters 34, L22316. http://dx.doi.org/10.1029/2007GL031902.
- Lokmer, I., Saccorotti, G., Di Lieto, B., Bean, C.J., 2008. *Temporal evolution of long-period seismicity at Etna Volcano, Italy, and its relationships with the 2004–2005 eruption.* Earth and Planetary Science Letters 266, 205–220.
- Lyell, C., 1859. *On the structure of lavas which have consolidate on steep slopes; with remarks on the mode of origin of Mt. Etna, and on the theory of "Center of Elevation"*. Phill Trans. Roy Soc, 703-785,
- Martini, F., C. J. Bean, G. Saccorotti, F. Viveiros, and N. Wallenstein, 2009. *Seasonal cycles of seismic velocity variations detected using coda wave*

interferometry at Fogo volcano, São Miguel, Azores, during 2003–2004. J. Volcanol. Geotherm. Res., 181, 231–246

- Matoza, R.S., Garcés, M.A., Chouet, B.A., D'Auria, L., Hedlin, M.A.H., De Groot-Hedlin, C., Waite, G.P., 2009. *The source of infrasound associated with long-period events at Mount St. Helens.* Journal of Geophysical Research 114, B04305. http://dx.doi.org/10.1029/2008JB006128.
- Matoza, R.S., Chouet, B.A., 2010. *Subevents of long-period seismicity: implications for hydrothermal dynamics during the 2004–2008 eruption of Mount St. Helens.* Journal of Geophysical Research 115, B12206. http://dx.doi.org/10.1029/2010JB007839
- McGuire, W. J., & Pullen, A. D., 1989. *Location and orientation of eruptive fissures and feederdykes at Mount Etna; influence of gravitational and regional tectonic stress regimes*. Journal of Volcanology and Geothermal Research, 38(3-4), 325-344.
- McNutt, S. R., 1996*. Seismic monitoring and eruption forecasting of volcanoes: a review of the state-of-the-art and case histories.* In Monitoring and mitigation of volcano hazards (pp. 99-146). Springer, Berlin, Heidelberg.
- McNutt, S. R., Rymer, H., & Stix, J., 2000*. Synthesis of volcano monitoring.* Chapter 71 of Encyclopedia of Volcanoes; Academic Press, San Diego, CA, 1167.
- McNutt, S.R., 2005. *Volcanic seismology.* Annual Review of Earth and Planetary Sciences 32, 461–491.
- Menke, W. 1984. *Geophysical data analysis: Discrete inverse theory. First edition*, Academic Press Inc., Orlando, Florida, 260 pp.
- Métaxian, J.-P., Lesage, P., Valette, B., 2002. *Locating sources of volcanic tremor and emergent events by seismic triangulation: application to Arenal volcano, Costa Rica.* Journal of Geophysical Research 107 (B10), 2243. http://dx.doi.org/10.1029/2001JB000559.

- Métaxian, J. P., O'Brien, G. S., Bean, C. J., Valette, B., Mora, M., 2009. *Locating volcano-seismic signals in the presence of rough topography: wave simulations on Arenal volcano, Costa Rica*. Geophysical Journal International, 179, 3, doi: 10.1111/j.1365-246X.2009.04364
- Miller, A. D., Stewart, R. C., White, R. A., Luckett, R., Baptie, B. J., Aspinall, W. P., ... & Voight, B., 1998. *Seismicity associated with dome growth and collapse at the Soufriere Hills Volcano, Montserrat*. Geophysical Research Letters, 25(18), 3401-3404.
- Minakami, T., 1974. *Seismology of volcanoes in Japan.* In Developments in Solid Earth Geophysics (Vol. 6, pp. 1-27). Elsevier.
- Molina, I., Kumagai, H., Yepes, H., 2004. *Resonances of volcanic conduit triggered by repeated injections of ash-laden gas*. Geophysical Research Letters 31, L03603. http://dx.doi.org/10.1029/2003GL018934.
- Monna, S., Frugoni, F., Montuori, C., Beranzoli, L., Favali P., 2004: *Valutazione della qualità del segnale sismico registrato dall'osservatorio geofisico marino SN-1*. In: Slejko D. and Rebez A. (eds), GNGTS 2004 – 23° Convegno Nazionale, Riassunti Estesi delle Comunicazioni, Tipografia Mosetti, Trieste, pp. 21-23.
- Monteiller, V., Got, J. L., Patanè, D., Barberi, G., Cocina, O., 2009. *Double-difference tomography at Mt Etna volcano: Preliminary results*. In The VOLUME Project–VOLcanoes: Understanding subsurface mass moveMEnt.
- Moran, S.C., Malone, S.D., Qamar, A.I., Thelen, W., Wright, A.K., Caplan-Auerbach, J., 2008. *2004–2005 seismicity associated with the renewed dome-building eruption of Mount St. Helens.* In: Sherrod, D.R., Scott, W.E., Stauffer, P.F. (Eds.), A Volcano Rekindled: The Renewed Eruption of Mount St. Helens, 2004–2006: U.S. Geological Survey Professional Paper 1750, pp. 27–60 (Chap. 2).
- Morrissey, M.M., Chouet, B.A., 1997. *A numerical investigation of choked flow dynamics and its application to the triggering mechanism of long-*

period events at Redoubt Volcano, Alaska. Journal of Geophysical Research 102, 7965–7983.

- Nadeau, P. A., Palma, J. L., & Waite, G. P., 2011. *Linking volcanic tremor, degassing, and eruption dynamics via SO_2 imaging*. Geophysical Research Letters, 38(1).
- Nakamichi, H., Kumagai, H., Nakano, M., Okubo, M., Kimata, F., Ito, Y., Obara, K., 2009. *Source mechanism of very-long-period event at Mt. Ontake, central Japan: response of a hydrothermal system to magma intrusion beneath the summit.* Journal of Volcanology and Geothermal Research 187, 167–177.
- Nakano, M., Kumagai, H., Kumazawa, M., Yamaoka, K., Chouet, B.A., 1998. *The excitation and characteristic frequency of the long-period volcanic event: an approach based on an inhomogeneous autoregressive model of a linear dynamic system*. Journal of Geophysical Research 103, 10,031–10,046.
- Nakano, M., Kumagai, H., 2005. *Response of a hydrothermal system to magmatic heat inferred from temporal variations in the complex frequencies of long-period events at Kusatsu-Shirane Volcano, Japan*. Journal of Volcanology and Geothermal Research 147, 233–244.
- Narváez, L., Cepeda, H., & Stix, J. (1997). *'Tornillo'-type seismic signals at Galeras volcano, Colombia, 1992–1993*. Journal of volcanology and geothermal research, 77(1-4), 159-171.
- Neuberg, J., Luckett, R., Ripepe, M., & Braun, T., 1994. *Highlights from a seismic broadband array on Stromboli volcano.* Geophysical Research Letters, 21(9), 749-752.
- Neuberg, J. and Pointer, T., 2000. *Effects of volcano-topography on seismic broadband waveforms*. Geophysical Journal International, 143, 239–248.
- Neuberg, J.W., Tuffen, H., Collier, L., Green, D., Powell, T., Dingwell, D., 2006. *The trigger mechanism of low-frequency earthquakes on Montserrat*. Journal of Volcanology and Geothermal Research 153, 37–50.

- Norini, G., & Acocella, V., 2011. *Analogue modeling of flank instability at Mount Etna: understanding the driving factors*. Journal of Geophysical Research: Solid Earth, 116(B7).
- O'Brien, G. S., Bean, C. J., 2004. *A 3D discrete numerical elastic lattice method for seismic wave propagation in heterogeneous media with topography*. Geophysical Research Letters, 31, L14608.
- Ohminato, T., Chouet, B.A., Dawson, P.B., Kedar, S., 1998. *Waveform inversion of very long-period impulsive signals associated with magmatic injection beneath Kilauea Volcano, Hawaii*. Journal of Geophysical Research 103, 23,839–23,862.
- Ohminato, T., Takeo, M., Kumagai, H., Yamashina, T., Oikawa, J., Koyama, E., Tsuji, H., Urabe, T., 2006. *Vulcanian eruptions with dominant single force components observed during the Asama 2004 volcanic activity in Japan*. Earth Planets Space 58, 583–593.
- Palma, J. L., Calder, E. S., Basualto, D., Blake, S., & Rothery, D. A., 2008. *Correlations between SO_2 flux, seismicity, and outgassing activity at the open vent of Villarrica volcano, Chile*. Journal of Geophysical Research: Solid Earth, 113(B10).
- Palo, M., Ibanez, J.M., Cisneros, M., Bretón, M., Del Pezzo, E., Ocana, E., Orozco-Rojas, J., Posadas, A.M., 2009. *Analysis of the seismic wavefield properties of volcanic explosions at Volcan de Colima, Mexico: insights into the source mechanism*. Geophysical Journal International 177, 1383–1398.
- Papale, P., 1999. *Strain-induced magma fragmentation in explosive eruptions*. Nature 397, 425–428.
- Patanè, D., Barberi, G., Cocina, O., De Gori, P., & Chiarabba, C., 2006. *Time-resolved seismic tomography detects magma intrusions at Mount Etna.* Science, 313(5788), 821-823.
- Patanè, D., Di Grazia, G., Cannata, A., Montalto, P., Boschi, E., 2008. *Shallow magma pathway geometry at Mt. Etna volcano*. Geochemistry, Geophysics, Geosystems 9, Q12021.

- Patanè, D., Aiuppa, A., Aloisi, M., Behncke, B., Cannata, A., Coltelli, M., Di Grazia, G., Gambino, S., Gurrieri, S., Mattia, M., Salerno, G., 2013. *Insights into magma and fluid transfer at Mount Etna by a multi-parametric approach: a model of the events leading to the 2011 eruptive cycle*. J. Geophys. Res. 118, 1–21. http://dx.doi.org/10.1002/jgrb.50248.
- Power, J.A., Lalla, D.J., 2010. *Seismic observations of Augustine Volcano, 1970–2007*. In: Power, J.A., Coombs, M.L., Freymueller, J.T. (Eds.), The 2006 Eruption of Augustine Volcano, Alaska: U. S. Geological Survey Prof. Pap. 1769, pp. 3–40 (Ch. 1).
- Prejean, S., Ellsworth, W., Zoback, M., & Waldhauser, F., 2002. *Fault structure and kinematics of the Long Valley Caldera region, California, revealed by high-accuracy earthquake hypocenters and focal mechanism stress inversions*. Journal of Geophysical Research: Solid Earth, 107(B12).
- Privitera, E., Sgroi, T., & Gresta, S., 2003. *Statistical analysis of intermittent volcanic tremor associated with the September 1989 summit explosive eruptions at Mount Etna, Sicily*. Journal of volcanology and geothermal research, 120(3-4), 235-247.
- Privitera, E., Bonanno, A., Gresta, S., Nunnari, G., and Puglisi, G. (2012). *Triggering mechanisms of static stress on Mount Etna volcano. An application of the boundary element method*. J. Volcanol. Geotherm. Res. 245–246, 149–158.
- Rasà, R., Azzaro, R., & Leonardi, O., 1996. *Aseismic creep on faults and flank instability at Mount Etna volcano, Sicily*. Geological Society, London, Special Publications, 110(1), 179-192.
- Ripperger, J., Igel, H., Wasserman, J., 2003. *Seismic wave simulation in the presence of real volcano topography*. Journal of Volcanology and Geothermal Research, 128 (1-3), 31-44.
- Rittman, A., 1973. *Mount Etna and the 1971 eruption-Structure and evolution of Mount Etna*. Phil. Trans. R. Soc. Lond. A, 274(1238), 5-16.

- Rowe, C., Thurber, R.C.H., White, R.A., 2004. *Dome growth behavior at Soufriere Hills Volcano, Montserrat, revealed by relocation of volcanic event swarms, 1995–1996*. Journal of Volcanology and Geothermal Research 134, 199–221.
- Rust, D., Behncke, B., Neri, M., & Ciocanel, A., 2005. *Nested zones of instability in the Mount Etna volcanic edifice, Italy*. Journal of Volcanology and Geothermal Research, 144(1-4), 137-153.
- Rust, A.C., Balmforth, N.J., Mandre, S., 2008. *The feasibility of generating low-frequency volcano seismicity by flow through a deformable channel.* In: Lane, S.J., Gilbert, J.S. (Eds.), Fluid Motions in Volcanic Conduits: A Source of Seismic and Acoustic Signals: Geol. Soc., London, Special Publications, 307, pp. 45–56.
- Saccorotti, G., & Del Pezzo, E., 2000. *A probabilistic approach to the inversion of data from a seismic array and its application to volcanic signals.* Geophysical Journal International, 143(1), 249-261.
- Saccorotti, G., Chouet, B., Dawson, P., 2001. *Wavefield properties of a shallow long-period event and tremor at Kilauea Volcano, Hawaii.* Journal of Volcanology and Geothermal Research 109, 163–189.
- Saccorotti, G., Lokmer, I., Bean, C.J., Di Grazia, G., Patane, D., 2007. *Analysis of sustained long-period activity at Etna Volcano, Italy.* Journal of Volcanology and Geothermal Research 109, 163–189.
- Salerno, G. G., Burton, M. R., Oppenheimer, C., Caltabiano, T., Tsanev, V. I., and Bruno, N., 2009. *Novel retrieval of volcanic SO_2 abundance from ultraviolet spectra*, J. Volcanol. Geotherm. Res., 181, 141–153, doi:10.1016/j.jvolgeores.2009.01.009.
- Salerno, G. G., Burton, M., Di Grazia, G., Caltabiano, T., & Oppenheimer, C., 2018. *Coupling between magmatic degassing and volcanic tremor in basaltic volcanism.* Frontiers in Earth Science, 6, 157.

- Schlindwein, V., Wassermann, J., & Scherbaum, F., 1995. *Spectral analysis of harmonic tremor signals at Mt. Semeru volcano, Indonesia.* Geophysical Research Letters, 22(13), 1685-1688.
- Shimozuru, D., Osada, N., Horigome, K., Sawada, M., Okada, A., Shibano, M., ... & Hosoya, Y., 1972. *Volcanic and seismic characteristics of Izu islands—brief summary of the special project of prediction of volcanic eruptions*. Bull. Volc. Soc. of Japan, 17, 66-87.
- Snieder, R., Trampert, J., 1999*. Inverse problems in geophysics. Reprinted from "Wavefield Inversion".* Ed. A. Wirgin, Springer Verlag, New York, 119-190 pp.
- Stein, S., Wysession, M., 2003. *An introduction to Seismology, Earthquakes, and Earth Structure*. Blackwell Publishing, England, 498 pp.
- Steinberg, G. S., & Steinberg, A. S., 1975. *On possible causes of volcanic tremor*. Journal of geophysical research, 80(11), 1600-1604.
- Stephens, C.D., Chouet, B.A., 2001. *Evolution of the December 14, 1989 precursory long-period event swarm at Redoubt Volcano, Alaska*. Journal of Volcanology and Geothermal Research 109, 133–148.
- Takei, Y. & Kumazawa, M., 1994. *Why have the single force and torque been excluded from seismic source models?* Geophysical Journal International, 118 (1), 20-30.
- Tarasewicz, J., White, R. S., Woods, A. W., Brandsdóttir, B. and Gudmundsson, M. T., 2012. *Magma mobilization by downward-propagating decompression of the Eyjafjallajökull volcanic plumbing system*. Geophysical Research Letters, 39(19).
- Thomas, M.E., Neuberg, J., 2012. *What makes a volcano tick — a first explanation of deep multiple seismic sources in ascending magma*. Geology 40 (4), 351–354.
- Torrence, C., Compo, G.P., 1998. *A Practical Guide to Wavelet Analysis*. Bull. Amer. Meteor. Soc., 79, 61–78.

- Torres, C., Gómez, M., & Narvàez, M., 1996. *Unusual seismic signals associated with the activity at Galeras volcano, Colombia, from July 1992 to September 1994.*
- Trovato, C., Lokmer, I., De Martin, F., Aochi, H., 2016. *Long period (LP) events on Mt Etna volcano (Italy): the influence of velocity structures on moment tensor inversion*. Geophysical Supplements to the Monthly Notices of the Royal Astronomical Society, 207(2), 785-810.
- Tuffen, H., Dingwell, D.B., Pinkerton, H., 2003. *Repeated fracture and healing of silicic magma generates flow banding and earthquakes?* Geology 31, 1089–1092.
- Tuffen, H., Dingwell, D., 2005. *Fault textures in volcanic conduits: evidence for seismic trigger mechanisms during silicic eruptions.* Bulletin of Volcanology 67, 370–387.
- Uhira, K., & Takeo, M., 1994. *The source of explosive eruptions of Sakurajima volcano, Japan*. Journal of Geophysical Research: Solid Earth, 99(B9), 17775-17789.
- Varley, N.R., Arambula-Mendoza, R., Reyes-Davila, G., Sanderson, R., Stevenson, J., 2010a. *Generation of Vulcanian activity and long-period seismicity at Volcan de Colima, Mexico.* Journal of Volcanology and Geothermal Research 198, 45–56.
- Varley, N.R., Arambula-Mendoza, R., Reyes-Davila, G., Stevenson, J., Harwood, R., 2010b. *Long-period seismicity during magma movement at Volcan de Colima*. Bulletin of Volcanology 72, 1093–1107.
- Vasco, D.W., 1989. *Deriving source-time functions using principal component analysis*. Bulletin of the Seismological Society of America, 79(3), 711-730.
- Vavryčuk, V., 2001. *Inversion for parameters of tensile earthquakes*. Journal of Geophysical Research, 106, B8, 16339-16355.
- Vavryčuk, V., 2015. *Moment tensor decompositions revisited*. J. Seismol. 19, 231–252.

- Viccaro, M., Garozzo, I., Cannata, A., Di Grazia, G., & Gresta, S., 2014. *Gas burst vs. gas-rich magma recharge: a multidisciplinary study to reveal factors controlling triggering of the recent paroxysmal eruptions at Mt. Etna*. Journal of volcanology and geothermal research, 278, 1-13.
- Voight, B., Sparks, R.S.J., Miller, A.D., Stewart, R.C., Hoblitt, R.P., Clarke, A., Ewart, J., Aspinall, W.P., Baptie, B., Calder, E.S., Cole, P., Druitt, T.H., Hartford, C., Herd, R.A., Jackson, P., Lejeune, A.M., Lockhart, A.B., Loughlin, S.C., Luckett, R., Lynch, L., Norton, G.E., Robertson, R., Watson, I.M., Watts, R., Young, S.R., 1999. *Magma flow instability and cyclic activity at Soufriere Hills Volcano, Montserrat, British West Indies.* Science 283, 1138–1142. http://dx.doi.org/10.1126/science.283.5405.1138.
- Waite, G.P., Chouet, B.A., Dawson, P.B., 2008. *Eruption dynamics at Mount St. Helens imaged from broadband seismic waveforms: interaction of the shallow magmatic and hydrothermal systems*. Journal of Geophysical Research 113, B02305. http://dx.doi.org/10.1029/2007JB005259.
- Waltershausen, W. S., 1880. *DerEtna. Vol. 1 and 2*, Engelman, Leipzig, 317 pp.
- Wassermann, J., 1997. *Locating the sources of volcanic explosions and volcanic tremor at Stromboli volcano (Italy) using beamforming on diffraction hyperboloids*. Phys. Earth Planet. Int., 10, 271-281.
- Wassermann, J., 2012. *Volcano Seismology, IASPEI New Manual of seismological observatory practice 2*. Deutsches GeoForschungsZentrum GFZ, Potsdam.
- Webb, S.L., Dingwell, D.B., 1990. *Non-Newtonian rheology of igneous melts at high stresses and strain rates: experimental results for rhyolite, andesite, basalt, and nephelinite.* Journal of Geophysical Research 95 (B10), 15,695–15,701.
- Zobin, V.M., Reyes, G.A., Guevara, E., Breton, M., 2008. *Seismological constraints on the position of the fragmentation surfaces in the volcano conduit*. Earth and Planetary Science Letters 275, 337–341.

- Zuccarello, L., Burton, M. R., G. Saccorotti, Bean, C. J., and Patanè, D., 2013. *The coupling between very long period seismic events, volcanic tremor, and degassing rates at Mount Etna volcano*. J. Geophys. Res. Solid Earth, 118, 4910–4921, doi:10.1002/jgrb.50363.
- Zuccarello, L., 2015. *Volcanic activity on Mt. Etna during quiescent October 2005-Jannuary 2006 period, inferred through very long period events, volcanic tremor, degassing rates and gravity.* PhD Thesis
- Zuccarello, L., Paratore M., La Rocca M., Ferrari F., Messina A., Branca S., Contrafatto D., Galluzzo D., Rapisarda S., García L., 2016. *Shallow velocity model in the area of Pozzo Pitarrone, Mt. Etna, from single station, array methods and borehole data*. Annals of Geophysics, doi:10.4401/ag-7086.